Photothermal Lateral Flow Assay with Inertial Microfluidic Enrichment for Early Detection of *E. coli* in Urinary Tract Infections

Yasaman Ghazi

A THESIS SUBMITTED TO

THE FACULTY OF GRADUATE STUDIES

IN PARTIAL FULFILLMENT OF THE REQUIREMENTS

FOR THE DEGREE OF MASTER OF SCIENCE

GRADUATE PROGRAM IN MECHANICAL ENGINEERING

YORK UNIVERSITY

TORONTO, ONTARIO

December 2025

Abstract

E. coli is one of the main causes of urinary tract infections (UTIs), but diagnosing it quickly and accurately is still not straightforward. The tests most commonly used, like culturing urine samples or examining them under a microscope, take time, depend on trained staff, and do not always give a clear answer when it comes to identifying *E. coli* specifically. This makes them less effective in point of care settings, where quick and reliable results are essential. Despite the frequency and seriousness of these infections, the tools available for diagnosis are still time consuming and require skilled workers and equipment which makes it less feasible for rapid, low-cost, sensitive ,and point of care diagnosis. Although recent advancements in lateral flow assays (LFAs) address these gaps, their high visual Limit of Detection (LOD) restricts their clinical efficacy. This thesis presents a diagnostic approach that combines microfluidic bacterial enrichment with photothermal detection to improve the sensitivity of lateral flow assays for detecting *E. coli* in UTIs. The microfluidic system is designed to concentrate bacteria by using viscoelastic forces, created by flowing Polyethylene Oxide (PEO) solutions at different rates through custom-built channels with straight, symmetric zigzag, and asymmetric zigzag shapes. The best enrichment achieved had design factors of 2 µL/min in straight channel with 1000 ppm PEO in a 25 µm × 25 µm channel. By reducing the sample volume while retaining the bacteria, this method increases the concentration of target cells and lowers the detection limit by roughly an order of magnitude.

Simultaneously, a photothermal detection method employing lock-in thermography was developed to detect and compare temperature fluctuations induced by nanoparticle-target binding events on the LFA test and control lines. This technique improved sensitivity by an additional two orders of magnitude compared to visual inspection alone.

The integrated microfluidic enrichment and photothermal detection system achieved about a 1000-fold improvement in sensitivity compared to standard visual LFAs. This notable advancement highlights the great potential of this combined approach to provide rapid, sensitive, and reliable point-of-care diagnostics for UTIs.

Several limitations were identified, including reliance on manual operation without closed-loop control, processing performed on desktop systems that reduce portability, and the use of PDMS channels that limit pressure tolerance. Considering these constraints, future work should include validation using clinical urine samples spanning diverse chemical and biological properties, broader testing across clinically relevant bacterial concentrations and strain types, and development of an integrated and automated platform with onboard fluidic control and embedded image processing to improve ease of use. Evaluation of rigid microchannels to enable higher flow operation and assessment of durability under extended use should be conducted. The platform should also be adapted and verified for additional bacterial pathogens and for deployment in varied diagnostic contexts where preconcentration and sensitive detection are required, thereby guiding the next phase of research and translation.

Acknowledgments

First and foremost, I would like to express my earnest gratitude to my supervisors Prof. Nima Tabatabaei and Prof. Pouya Rezai for giving me the opportunity to study at York University and their guidance and patience throughout my M.Sc. studies.

I would like to thank Prof. Satinder K. Brar for her support and advice during my comprehensive exam and annual committee meetings. I am also grateful to Prof. Satinder Brar and Prof. Paul O'Brien for their consideration and patience during the thesis examination.

I express my sincere thanks to my colleagues at York University for their support and guidance during my M.Sc. studies. Especially, Dr. Arsalan Nikdoost, Nakisa Samadi and Derek Hayden for their valuable advice and support over the past years. I am also grateful to my dear friends for their friendship and encouragements and always being there for me through thick and thin.

Finally, I would like to acknowledge my family for their unconditional support in every step of my life.

Table of Contents

List of Tables

List of Figures

Abbreviations

3D: Three-dimensional

AR: Aspect ratio

AuNPs: gold nanoparticles

CAD: Computer aided design

CCD: Charge-coupled device

CFU: Colony forming unit

CI: Confidence interval

CLIA: Chemiluminescent immunoassays

CMOS: Complementary metal-oxide-semiconductor

CTC: Circulating tumour cell

CW: Continuous-wave

DI Water: Deionized water

E. coli: Escherchia coli

ELISA: Enzyme-linked immunosorbent assay

EV: Extracellular-vesicle

FD-PTR: frequency-domain photothermal radiometry

FFT: Fast Fourier transfer

FOV: Field of view

FWHM: Full width at half maximum

GMR: Giant magnetoresistive

HUS: hemolytic-uremic syndrome

IM: Inertial microfluidics

IPA: Isopropanol alcohol

LED: Light emitting diode

LFA: Lateral flow assay

LFIA: Lateral flow immunoassay

LIT: Lock-in thermography

LOC: Lab on chip

LOD: Limit of detection

MCT: mercury cadmium telluride

PBS: Phosphate-buffered saline

PCR: Polymerase chain reaction (PCR)

PDMS: Poly[dimethyl siloxane]

PEO: Poly[ethylene oxide]

POC: Point of care

PT: Photothrmal

PTR: Photothermal radiometry

P- PTR: Pulsed photothermal radiometry

PSA: Prostate-specific antigen

PTR: Photothermal radiometry

PWM: Pulse-width-modulated

RBC: Red blood cell

rGo: reduced graphene oxide

RoI: Region of interest

SAD: Strand displacement amplification

SERS: Surface-enhanced Raman scattering

SPR: Surface plasmon resonance

STEC: Shiga toxin–producing *Escherichia coli*

STX: Shiga toxins

THTC: Too high to count

TLTC: Too low to count

TMR: Tunnel magnetoresistive

TPLI: Thermophotonic lock-in imaging

UPEC: Uropathogenic *Escherchia coli*

UTI: Urinary tract infection

Glossary of Terms

Acoustophoresis: Migration of particles under the effect of acoustic force exerted by ultrasound waves.

Analytes: A component or chemical substance that is the subject of an analytical procedure.

Blockage ratio: The ratio of particle diameter to the channel hydraulic diameter.

Dielectrophoresis: The movement of neutral particles when subjected to a non-uniform electric field.

Lab-on-a-chip: A microdevice, which integrates different laboratory functions on a single integrated circuit with a size up to few square centimeters.

Magnetophoresis: This method utilizes the magnetic field gradients to apply a force to particles or cells with magnetic susceptibilities different from the carrying fluid.

Microfluidics: The technology to manipulate fluids in channels with tens of micrometer in size.

Non-Newtonian fluid: A fluid, which do not follow the Newton's law of viscosity.

Relaxation time: A characteristic time of a fluid in which it relaxes from a deformed state.

Viscoelastic fluid: A type of non-Newtonian fluid, which exhibit both viscous and elastic behavior towards deformation.

Chapter 1

1 Introduction and Literature Review

1.1 Introduction

1.1.1 Introduction to Urinary Tract Infections (UTIs)

Human urine is commonly used in regular medical checkups and tests to identify the cause of symptoms, because urine is a rich source for evaluating overall health, especially kidney function, as it contains hundreds of body wastes that the kidneys filter from the blood[1].

Bacterial urinary tract infections (UTIs) are among the most frequently encountered bacterial infections, which are painful and economically costly, impacting mostly women due to anatomic differences [2,3]. UTIs are one of the most frequently occurring infectious diseases worldwide, affecting 150 million people every year [4]. They account for 8 million hospital visits annually in the U.S. [5]. UTIs are responsible for 1% to 3% of all medical consultations in Great Britain[1].

The volume of antibiotic agents prescribed and urine culture testing associated with the management of acute cystitis in the community is substantial. Half of all females experience at least one episode of acute cystitis in their lifetime [6,7]. In the United States, there are approximately 4 million outpatient visits annually by females for uncomplicated UTI [8]. An antibiotic agent is prescribed in 67% of visits, and a urinalysis is ordered in 81%, [8] with wide variations in physician management [9,10]. As many as 40% of antibiotics prescribed may be unnecessary because the subsequent urine culture result is negative [11]. The cystitis decision aid is a simple clinical approach that could reduce practice variation as well as unnecessary antibiotic prescriptions and urine culture testing.

Among individuals who experience a first infection, 20% experience a second infection within six months, and 3% experience a third infection within six months [4,12] . In addition, UTIs have a high recurrence rate, and early treatment is required for reducing morbidity and the risk of recurrence[5].

1.1.2 *E. coli* as a Major Causative Agent of UTIs

Escherichia coli (*E. coli*) is responsible for up to 80% of UTIs [13,14]. Uropathogenic *E. coli* (UPEC) is responsible for approximately 80−85% of community-acquired uncomplicated UTI cases [4,15,16]. It can invade the urothelial cell lining and live within the urinary tract by evading the host's immune response[17]. Generally, healthy urine should be sterile [18], and therefore, a urine culture with *E. coli* concentration of 10^4 to 10^5 colony-forming unit (CFU) per mL or above confirms UTI [4,5,19]. Of note, in acute cystitis, a lower threshold ($\geq 10^2$ CFU/mL) can also define a positive culture [20].

The hemolytic-uremic syndrome (HUS) is a rare but serious disease that predominates in young children and is frequently associated with infection due to serotype O157 Shiga toxin–producing Escherichia coli (STEC) [21]. In some cases, STEC infection may manifest as a UTI, highlighting that urine-based testing can be crucial in detecting *E. coli* O157 in patients at risk of HUS [22].

When diagnostic questions arise about a possible STEC infection, immunoassays for Shiga toxins (STX) or molecular methods (e.g., Polymerase chain reaction (PCR)) to detect STX genes may be preferable to cytopathogenicity testing on cell lines, since these approaches provide faster and more specific identification of toxin-producing strains. Although HUS is most often linked to pediatric enteric infections with *E. coli* O157, case reports have documented HUS following UTIs with STEC in adults, even in the absence of diarrhea. This highlights the importance of direct detection of STX or their genes in urinary *E. coli* isolates.

There is also concern regarding the possible adverse effect of antibiotics on HUS outcomes. Several authors suggest that certain antimicrobial therapies may increase the release of STX, thereby worsening or precipitating HUS [21,23]. These findings underscore that STEC-associated UTIs, though rare, represent a serious diagnostic and therapeutic challenge, in contrast to the far more common UPEC infections, where persistence is driven by intracellular reservoirs rather than toxin release [23].

1.1.3 Antibiotic Resistance and Global Concerns

The rise of antibiotic resistance has been widely recognized as one of the major global societal threats of this century [23,24]. Over 50% of antibiotics are either incorrectly or unnecessarily prescribed, a trend that fuels bacterial resistance [25]. With increasing resistance, front-line agents are at risk of losing their efficacy.

Various organizations have introduced incentives to address this crisis, including the 2014 Longitude Prize (focused on better, faster, cheaper pathogen detection) and the Infectious Disease Society of America's calls to develop new antibacterial drugs [26]. Public Health England has published studies indicating that UTI is the second-highest prescription driver in primary care, especially among the elderly (>65 years) [27].

A recent report concluded that more than half of antibiotic prescriptions are either incorrect or unwarranted [25]. With current prescribing trends, it is predicted that resistance rates will continue to rise, emphasizing the urgent need for diagnostic tools that can curb antibiotic overuse [28].

1.1.4 Diagnosis: Traditional and Emerging Approaches

1.1.4.1 Standard-of-Care Diagnostic Workflows

Generally, UTI is diagnosed symptomatically, treated empirically, and confirmed via 48 h laboratory testing [29]. This approach has been used for decades to manage the high case volume of infections [30]. The gold standard for pathogen detection and quantification is based on cell culture methods, typically taking 48 to 72 h [4,26]. Delays in treatment for UTIs can have serious clinical and public health implications. They prolong symptoms like pain and urinary urgency, increase the risk of progression to kidney infections and long-term damage (especially in children), and may lead to ineffective initial antibiotic use when resistance is present. Additionally, such delays drive overuse of broad-spectrum antibiotics, contributing to the global problem of antimicrobial resistance. [31]

1.1.4.2 Emerging Rapid Molecular and Immunological Methods

Several rapid molecular-based methods (e.g., PCR, immunoassays) are available for pathogen identification [27,28]. However, these methods can be high-cost, require specialized instruments, and

need extensive sample preparation (nucleic acid extraction, cell lysis, and amplification) which restricts their use in resource-limited areas [27].

In recent years, there has been an emphasis on developing better, faster, and more affordable tests to enable evidence-based prescriptions at the point-of-care (POC) [28]. POC testing for UTIs helps reduce unnecessary antibiotic prescriptions and can be critical in elderly populations, where a short delay can increase mortality [32]. Timely and cost-effective POC diagnostics can also help mitigate antibiotic resistance by guiding appropriate antibiotic use [33].

In summary, UTIs remain a significant global health concern, affecting millions of people each year and driving considerable antibiotic usage[4]. *E. coli*, particularly UPEC strains, continues to be the main causative agent, responsible for 80−85% of community-acquired uncomplicated UTIs[4,15,16]. The combination of high prevalence, recurrence rates, and rising antibiotic resistance underscores the urgent need for rapid, accurate, and cost-effective diagnostic tools [29]. While traditional culture methods remain the gold standard, they are slow (48–72 h)[4,12,27], and newer molecular and immunologic assays, although faster, face challenges of cost and accessibility[28,29]. Global efforts such as the 2014 Longitude Prize, the Infectious Disease Society of America's "10×'20 initiative," and research into portable POC solutions highlight the push toward better diagnostics. By minimizing diagnostic delays and informing targeted therapy, these emerging technologies can not only improve patient outcomes but also help curb the overuse of antibiotics and mitigate the growing crisis of antimicrobial resistance[25,29].

1.2 Literature Review

Diagnostics consist of two interconnected stages: sample preparation and detection. Each stage is critical for achieving reliable results, yet advances in detection technologies have often dominated discussions of diagnostic progress. In contrast, the integration of effective sample preparation methods has received less emphasis, even though approaches such as enrichment play a central role in improving sensitivity by increasing the concentration of target analytes. To situate this thesis within the broader diagnostic landscape, this chapter first examines detection approaches and explains the rationale for selecting LFAs as the primary method of focus. It then turns to enrichment as a key sample preparation strategy that enhances sensitivity and concludes with a review of LFA readers. This structure emphasizes the interdependence of preparation and detection and points to their integration as a foundation for next-generation diagnostic platforms. The chapter concludes by outlining the objectives of the thesis.

1.2.1 Literature Review on *E. coli* Detection Technologies

The detection of *E. coli*, a significant public health concern, is essential for applications ranging from clinical diagnostics (e.g., UTI) to food safety and environmental monitoring. Advances in detection technologies have introduced innovative methods that enhance sensitivity, reduce detection time, and improve portability. This review examines recent developments in *E. coli* detection technologies, focusing on their applications, strengths, and limitations.

1.2.1.1 Biosensors and Nanosensors

Biosensors and nanosensors have become an important class of diagnostic tools for the detection of pathogenic bacteria, including *E.coli*. These technologies typically rely on transducing

a biological recognition event into a measurable signal, such as an electrochemical response, fluorescence emission, or optical resonance shift. Their main advantage lies in the ability to provide rapid, sensitive detection without the need for lengthy culture steps. Within this category, a wide range of strategies have been explored.

Detection limits in the range of 10–10^3 CFU/mL with turnaround times from 30 minutes to a few hours have been reported in the literature for electrochemical and optical UTI biosensors. For instance, Psotta et al.[41] reported a Prussian Blue sensor detecting 10^3 CFU/mL in urine within 4 h, while Yao[42] et al. developed a FRET-based fluorescent biosensor detecting 467 CFU/mL in 30 minutes. More biologically inspired strategies include bacteriophage-mediated lysis coupled with image analysis by Yang et al.[43], and mannose-functionalized microspheres by Vendeville et al.[44] for rapid agglutination assays. Despite their impressive sensitivity, these methods often require skilled operators, additional equipment, or centrifugation steps that limit true POC use.

Microchip-based technologies, including microfluidic lab-on-a-chip (LOC) devices and nanosensor-enabled platforms, have advanced considerably over the past decade. These devices typically combine sample handling, concentration, and detection on a single microfabricated platform, offering the potential for rapid, automated diagnostics at the point of need. The miniaturized architecture not only reduces sample and reagent consumption but also enables multiplexing and integration with modern computational tools such as artificial intelligence.

Several approaches illustrate the versatility of these platforms. For instance, Demirci et al.[45] reported a portable microfluidic chip that detects *E. coli* in phosphate-buffered saline (PBS), blood, milk, and spinach, achieving detection limits as low as 50 CFU/mL in PBS, blood, and milk and 500 CFU/mL in spinach within 30 minutes. Similarly, Li et al.[46] demonstrated a thin-film transistor image sensor integrated with deep learning, which reduced analysis time by ~12 hours compared

to culture and achieved an accuracy of 97.3% after 9 hours of incubation. Yang et al.[47] developed a LOC platform incorporating dual chambers for concentration and impedance-based detection using antibody-coated magnetic beads, reaching a detection limit of 10^5 CFU/mL but requiring further sensitivity improvement. Finally, Gur et al.[48] used surface plasmon resonance (SPR) with gold nanoparticles to achieve ultra-sensitive detection at the single-cell level (1 CFU/mL), although challenges such as complex fabrication, limited reusability, and specificity issues remain.

As in Table 1-1, overall, microchip-based technologies highlight the versatility of LOC platforms and their ability to incorporate advanced sensing modalities. These systems are attractive for their speed, sensitivity, and potential for integration with computational tools. However, they also face key barriers, including matrix variability, device complexity, and limited robustness in field conditions. Further innovation is needed to transition these promising prototypes into widely deployable diagnostic products.

Table 1-1 Literature review summary

Ref	**Detection Method**	**Matrix**	**LOD (CFU/mL)**	**Time**	**POC Suitability**	**Notes / Limitations**
Psotta et al.[34]	Prussian Blue Electrochemical Sensor	Urine	10^3	4 h	Partial	Requires electrode setup, not fully integrated
Yao et al.[35]	FRET-based fluorescent biosensor	Urine	467	30 min	Partial	Requires fluorescence reader

Yang et al.[36]	Phage lysis + image analysis	Urine	~10^2–10^3	<1 h	No	Image processing needed; needs bacterial incubation
Vendeville et al.[37]	Mannose-functionalized beads (Agglutination)	Urine	~10^4	15 min	Yes	Visual but semi-quantitative; prone to interpretation errors
Demirci et al.[38]	Microfluidic chip	PBS, urine, blood	50	30 min	Yes	Sample compatibility across matrices, microscopy required
Li et al.[39]	TFT-based sensor + Deep Learning	Urine	N/A (Accuracy 97%)	9 h	No	Requires incubation and AI processing
Yang et al.[40]	Dual-chamber LOC with impedance	Urine	10^5	~1 h	No	Needs further optimization
Gur et al.[41]	SPR with gold nanoparticles	Model urine	1	~30–60 min	No	Complex fabrication, high cost, low field robustness

1.2.1.2 Paper-Based Devices and Rapid Assays

Lateral flow immunoassays (LFAs) are among the most widely used paper-based diagnostics because they are inexpensive, portable, and simple to use. In the sandwich format, which is the most common, the target analyte binds to both a mobile detector antibody and an immobilized capture antibody. As seen in Figure 1-1, his interaction produces a colored line due to the accumulation of gold nanoparticles (GNPs), whose intensity increases with analyte concentration [42,43]. While GNPs are the most commonly used label in LFAs, alternative labels such as colored latex beads, carbon nanoparticles, fluorescent tags, or magnetic particles may also be used, depending on the required sensitivity and detection method[44]. A control line coated with anti-species antibodies confirms proper fluid migration and reagent integrity.

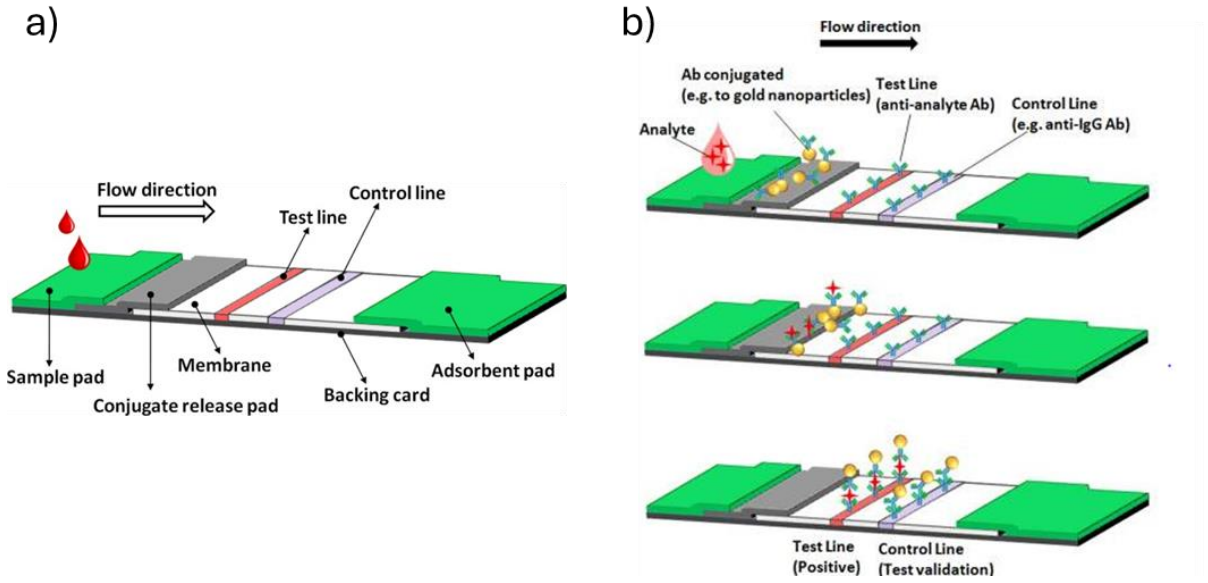

Figure 1-1 a) LFA is usually composed of the following elements: sample pad, conjugate release pad, membrane with immobilized antibodies and adsorbent pad. The components of the strip are usually fixed to an inert backing material. b) Schematic representation of the assay's mechanism. Top: the sample is deposited on the sample pad and migrates towards the conjugate. Middle: the conjugated antibodies bind

the target analyte and (bottom) migrate to the test line, where the bound target analyte is captured. Reprinted with permission from MDPI [42].

Despite their advantages, LFAs exhibit limited sensitivity and quantitative reliability compared with standard laboratory methods such as culture and PCR, and their sandwich format depends on well-matched antibody pairs and is susceptible to effects such as signal saturation (hook effect) [45–47]. Alternative LFA configurations, including competitive assays for small molecules and multiplexed formats using spatially separated test zones or spectrally distinct labels, expand analytical flexibility and enable simultaneous detection of multiple targets [43,47,48] . While LFAs enable rapid, low-cost, and instrument-free detection, exemplified by the hCG pregnancy test, their performance remains constrained by sensitivity and limited quantitative accuracy. Consequently, extensive efforts have focused on improving LFA performance through nanomaterials, signal amplification strategies, and portable readers, with recent reviews of *E. coli* biosensors highlighting progress toward enhanced reproducibility, sensitivity, and standardization for robust POC diagnostics [49].

1.2.1.3 Challenges and Future Directions

Recent studies by Cho et al. [50] and Lenhert et al. [51] report that integrated microfluidic assays can achieve detection limits below 10^2 CFU/mL with assay times of 15–100 min; however, most platforms rely on off-chip pre-treatment steps such as filtration, centrifugation, or external enrichment to reach these sensitivities, undermining true POC portability. While on-chip integration of lysis chambers, magnetic bead–based extraction, and self-contained cartridges reduces manual handling, these approaches introduce increased device complexity, fabrication cost, and limited multiplexing capability. Similarly, portable molecular diagnostics (e.g., handheld PCR and LAMP) demonstrate feasibility at the point of need but remain constrained by cost,

operator dependence, and turnaround time, while smartphone-based LFA readers improve analytical reliability yet remain limited by intrinsic LFA sensitivity and reproducibility issues.

Representative hybrid approaches highlight these trade-offs. Wang et al. [52] reported a turntable paper-based ELISA with a detection limit of 10^5 CFU/mL, whereas Wu et al. [53] achieved 10 CFU/mL in 30 min by integrating strand displacement amplification with LFAs, at the expense of increased workflow complexity and sample preparation.

In this work, these limitations are addressed by combining passive viscoelastic microfluidic enrichment with a lock-in photothermal LFA reader. Continuous-flow inertial–elastic focusing concentrates *E. coli* on-chip without filtration or centrifugation, preserving POC portability identified as lacking in prior studies [50,51]. The use of valve-free PDMS channels with passive multi-outlet collection reduces fabrication complexity and cost, while upstream enrichment preserves compatibility with standard LFAs and lowers the effective detection limit at the reader stage. Finally, lock-in photothermal detection improves quantitative robustness by mitigating ambient-light variability inherent to colorimetric and smartphone-based readouts, yielding a simplified and portable workflow with enhanced sensitivity suitable for practical POC deployment.

1.2.2 Bacteria focusing and enrichment

The process of concentrating solid contents such as biological cells, pathogens, and bacteria from large volumes of biofluids is a crucial step for effective downstream detection. This concentration is typically achieved through methods like centrifugation or membrane-based filtration. In centrifugation, solids settle at the bottom of a tube under the influence of centrifugal force, followed by the removal of the supernatant to reduce the sample volume. However, this method often requires expensive, bulky equipment and struggles to effectively process rare cells

in large-volume fluids. Alternatively, membrane-based filtration faces challenges such as membrane clogging and difficulties in recovering cells that become trapped or adhere to the membrane, making the process less efficient in certain scenarios [54–57].

The emergence of microfluidic technologies has introduced advanced methodologies for efficient volume reduction, enabling sample handling in compact and cost-effective formats. Various microfluidic strategies have been developed for target enrichment, including inertial microfluidics [58–60], electrokinetic techniques [61–63], acoustofluidics [64,65], magnetophoresis [66], and viscoelastic fluid–based approaches [67,68]. Despite their demonstrated efficacy, the majority of these methods rely on external field generators or necessitate trained personnel for operation, thereby constraining their practical utility in POC diagnostics. Furthermore, several microfluidic platforms have been specifically tailored to facilitate the enrichment of *E. coli*, as outlined in the subsequent section.

1.2.2.1 *E. coli* Enrichment

Some diagnostic strategies integrate enrichment and detection into a single process, making enrichment methods specific to the detection technique itself. For instance, Zhang et al. [69] introduced a novel one-step filtration protocol for separating and enriching bacterial cells from urine samples, tailored for droplet-based detection using molecular peptide nucleic acid probes; this method achieves up to 91% bacterial recovery and incorporates a syringe filter for buffer exchange, amplifying bacterial concentration by 10-fold but remains specific to droplet-based workflows and operates at an average flow rate of ~5.55 μL/min. Similarly, Kim et al. [70] developed a floating magnetic membrane method to concentrate pathogenic bacteria from large volumes, achieving a 92-fold increase from a 50 mL sample with >90% capture efficiency up to 1.2 mL/min, though performance drops to ~80% at 2.0 mL/min due to loss of magnetic nanoparticles and

reduced contact time; this method also relies on technician expertise. In another example, Kwon et al. [71] engineered a microfluidic chip using magnetic enrichment and photothermal DNA extraction, processing 20 mL samples followed by elution at 200 μL/min; although the fold increase *is not* reported, the chip supports high-throughput processing. Koo et al. [72] further proposed a thermoresponsive nanowire-integrated microfluidic chip combined with a gold-nanoparticle click-based colorimetric assay, enabling a red-to-blue visual signal and detecting pathogens such as *E. coli* at concentrations as low as 10^3 CFU; this system achieves ~5-fold enrichment at 1 mL/h but loses efficiency at higher flow rates.

In contrast to these detection-coupled approaches, inertial microfluidics offers a more modular enrichment technique; it focuses cells into defined streamlines and removes the surrounding fluid via separate outlets, thereby increasing target concentration and supporting integration with various downstream assays. Multiple concentrators have been developed based on this principle, highlighting inertial microfluidics' flexibility as a standalone enrichment platform.

1.2.2.2 Microfluidic *E. coli* Enrichment

Inertial microfluidics systems exploit inertial focusing, a regime in which suspended particles migrate toward well-defined equilibrium streamlines once inertial and viscous forces become comparable. As demonstrated in Figure 1-2 by Peng et al. [73], under these conditions, particles experience a combination of wall-induced and shear-gradient lift forces. In curved or spiralled geometries, an additional Dean drag force arising from secondary flows and Elastic force in non-Newtonian substances could be effective as well. The vector sum of these effects drives particles of different size, density, or shape to distinct lateral positions within the channel cross-section. By tailoring channel geometry and tuning flow rate, inertial microfluidics devices harness this behaviour to isolate, concentrate, or trap selected particles from complex samples [74].

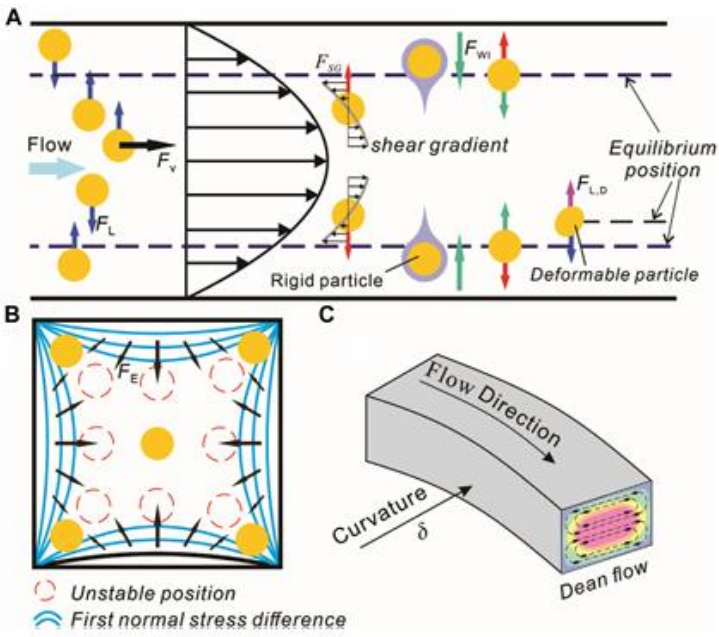

Figure 1-2 Schematic of hydrodynamic forces in microfluidics. (A) Inertial forces in a straight microchannel. (B) Elastic force distribution in a square cross-section microchannel. (C) Dean flow within a curved microchannel. Reprinted with permission from Frontiers [73]

Four general categories of inertial microfluidics geometries that have been implemented are straight, contraction–expansion array, curved, and spiral channels. Straight channels rely on the interplay of two primary lateral forces, which are the wall-effect lift force and the shear-gradient lift force [75,76]. The combined magnitude of these forces can be expressed as the net inertial lift forces (F_L) on microparticles can be scaled as:

$$F_L \sim \rho U^2 a_p^4 / D_h^2 \tag{1-1}$$

where ρ stands for the fluid density, a_p the particle diameter, and D_h the hydraulic diameter (defined later). The average fluid velocity U is calculated as:

$$U = \frac{Q}{h \times w} \tag{1-2}$$

In which Q represents the flow rate. Also, D_h denoted as the hydraulic diameter is calculated as below, with w and h referring to the channel's width and height, respectively.

$$D_h = \frac{2w \times h}{w + h} \tag{1-3}$$

Substituting these definitions into the scaling of the inertial lift force yields:

$$F_L \sim \frac{\left(\frac{1}{4}\rho Q^2\right)\left(a_p^4\right)(w + h)^2}{(wh)^4} \tag{1-4}$$

Non-dimensional Reynolds number ($Re = \rho U D_h/\mu$) is used to characterize the fluid flow regime inside a channel, where μ is the dynamic viscosity. The Reynolds number represents the ratio of inertial forces with respect to the viscous forces.

$$Re = \rho U D_h/\mu \tag{1-5}$$

As demonstrated in Figure 1-3, in curved microchannels, there is a velocity mismatch between fluid particles at different locations inside the channel. In curved microchannels, curvature introduces a centrifugal body force $F_c \sim \rho u^2/R$ that drives the high-momentum core toward the outer wall. The resulting transverse pressure gradient, together with viscous resistance near the walls, creates a cross-sectional recirculation: fluid moves outward near the channel center and returns inward along the walls, forming a pair of counter-rotating Dean vortices superimposed on the axial Poiseuille flow. This velocity mismatch would result in secondary vortices (called Dean vortices) in the channel cross-section.

Because of these secondary vortices, particles are subject to an additional drag force [74] (i.e. Dean drag) which could be scaled as:

$$F_D \sim \rho U^2 a_P D_h^2 R^{-1} = \frac{4\rho Q^2 a_P}{R(w + h)^2} \tag{1-6}$$

The balance between the net inertial lift forces and the Dean drag determines the equilibrium positions of microparticles within curved microchannels, as depicted below. A similar mechanism

can be observed in zigzag channels, where periodic directional changes in flow generate alternating Dean vortices analogous to those in curved geometries, resulting in comparable lateral migration and focusing behavior.

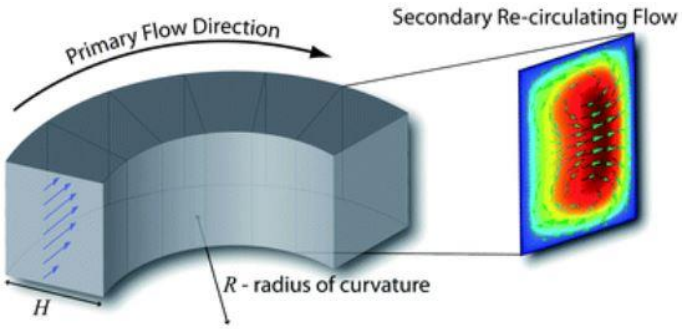

Figure 1-3 Dean flow in curvilinear microchannels. The fluid elements close to the channel center experience a higher centripetal force and travel to the outer side of the curve. The stagnant elements close to the walls travel inwards and this result in two symmetric vortices. Reprinted with permission from Royal Society of Chemistry[77]

The strength of these secondary vortices could be characterized by another non-dimensional number. Dean number (De) represents the ratio of inertial forces with respect to the centrifugal forces, where R stands for Radius of curvature.

$$De = Re \times \sqrt{(D_h/2R)} \tag{1-7}$$

In more complex channel geometries, such as zigzag or extraction/contraction microchannels, there is also the effect of Dean forces, but in a slightly different way due to the curvature radius. For instance, as shown in Figure 1-4**,** the Z-RISE study by Bazaz et al. [78] demonstrated that a rigid, 3D-printed symmetric zigzag channel could achieve inertial focusing of particles as small as 3 μm in a Newtonian fluid (water or MACS buffer), with effective focusing observed down to a blockage ratio of $\beta = a_P/D_h \approx 0.04$, where blockage ratio is defined as particle to the channel's hydraulic diameter ratio.

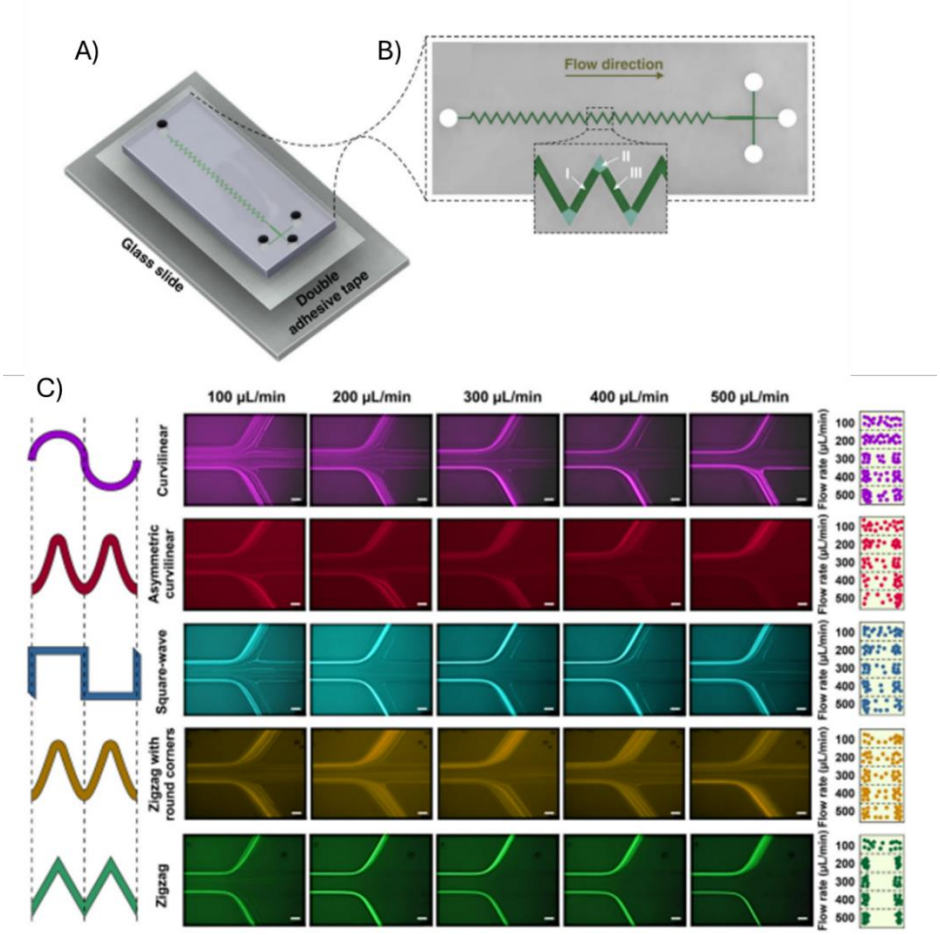

Figure 1-4 Description of the Z-RISE system. A) Macroscopically shown inertial microfluidic channel for the Z-RISE system. B) A close-up of the Z-RISE channel that reveals its 21 zigzag loops. C) Left: Fabricated curvilinear, asymmetric curvilinear, square-wave, zigzag with rounded corners, and zigzag-shaped channels with identical footprint, hydraulic diameter, sample volume, overall length, and breadth to allow comparison of the effects of the overall device geometry. The Z-RISE microchannel outperforms the curvilinear, asymmetric curvilinear, square-wave, and zigzag with round corner microchannels, according to fluorescent images of each device at increasing flow rates. The channel can concentrate 3 m particles on the sidewalls starting at flow rates of 200µL/min (scale bar is 100 µm). Right: A schematic representation of the particle location at each serpentine microchannel's output. The results show that 3 µm particles may be completely focused by Z-RISE at the channel sidewalls. Reprinted with permission from Royal Society of Chemistry (Great Britain).[78]

Recent research underscores the particular significance of focusing the submicron-sized particles, which pose distinct challenges due to their inherently weaker lift forces. It has been

demonstrated that microparticles with sizes corresponding to 0.07–0.2 times the hydraulic diameter of the microchannel (blockage ratio $\beta \geq 0.07$) are effectively influenced by two dominant inertial lift forces, dictating their equilibrium positions within the flow [74]. Here, the blockage ratio serves as a crucial parameter. Understanding and leveraging these factors is key to optimising inertial microfluidic performance, particularly for precise focusing and manipulation of particles at submicron scales.

Investigators have shown that replacing the Newtonian carrier with a weakly elastic polymer solution can magnify the size-selective lift forces and extend inertial focusing into the sub-micron regime. Liu *et al.* [79] employed a viscoelastic strategy in a straight rectangular channel, directing large extracellular vesicles (EVs) toward the channel core while leaving the exosome-enriched fraction in the peripheral streams. Similarly, Zhou et al. [80] consumed a dilute polyethylene-oxide (PEO) solution in a sequence of alternating-handed spiral microchannels to isolate exosomes from heterogeneous EV suspensions. In this design, the viscoelastic hoop stresses generated by the PEO fluid acted harmoniously with geometry-induced, reversing Dean vortices. Vesicles larger than ≈ 300 nm were guided into the centre sheath stream, whereas smaller exosomes (~100 nm) were retained near the side walls.

In viscoelastic flows, suspended particles experience an additional elastic force (F_E), as illustrated by the simulations of Charjouei et al. [81] in Figure 1-5. Elastic force scales as the equation below:

$$F_E \sim a_P^3 \, \lambda \, (\frac{Q}{hw^2})^3 \tag{1-8}$$

in which λ is the longest relaxation time of the fluid.

Inside a viscoelastic medium, the ratio of elastic forces to the inertial forces is presented by the Elasticity number ($El = \frac{\lambda\mu(h+w)}{\rho w h^2}$), where η_0 is the viscosity of the fluid:

$$El = \frac{\lambda\mu(h+w)}{\rho w h^2} \tag{1-9}$$

The application of viscoelastic fluids could further enhance the particle enrichment, especially at a smaller blockage ratio. Charjouei Moghadam et al. [81] conducted a parametric study on elasto-inertial focusing of microparticles in a straight microchannel, examining factors like Reynolds number, dimensionless channel length, and blockage ratio. Their findings highlighted that even a small blockage ratio (as low as 0.05) is effective for elasto-inertial focusing, contrasting with previous studies in non-elasto-inertial (Newtonian) focusing.

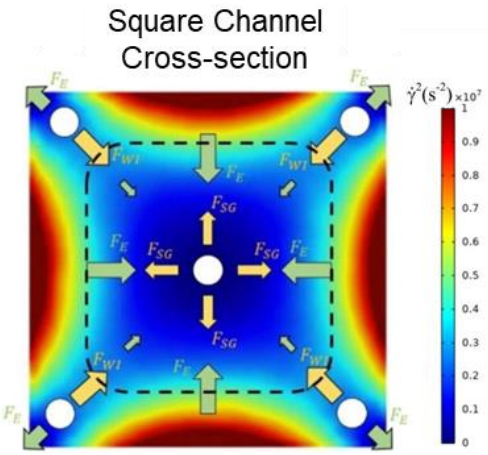

Figure 1-5 Particle focusing in a straight microchannel. The net lateral migration results from the balance of the elastic lift (F_E) with the wall induced (F_{WI}) and shear gradient (F_{SG}) components of the inertial lift, driving particles toward stable equilibrium positions across the channel cross section.. Reprinted with permission from AIP Publishing [81]

Similarly, Zhang et al. [82] explored the use of a viscoelastic microfluidic device for separating and enriching *E. coli* clusters from singlets as in Figure 1-6. Using polystyrene particles of 1 and 4.8 μm to simulate *E. coli* singlets and clusters, they found that inertial and elastic forces caused

size-dependent particle migration toward the channel center. The smaller particles remained closer to the sidewalls, while the larger ones aligned closer to the channel midline. Key variables impacting this size-dependent separation included channel length, the ratio of sheath to sample flow rate, and PEO concentration in the microdevice.

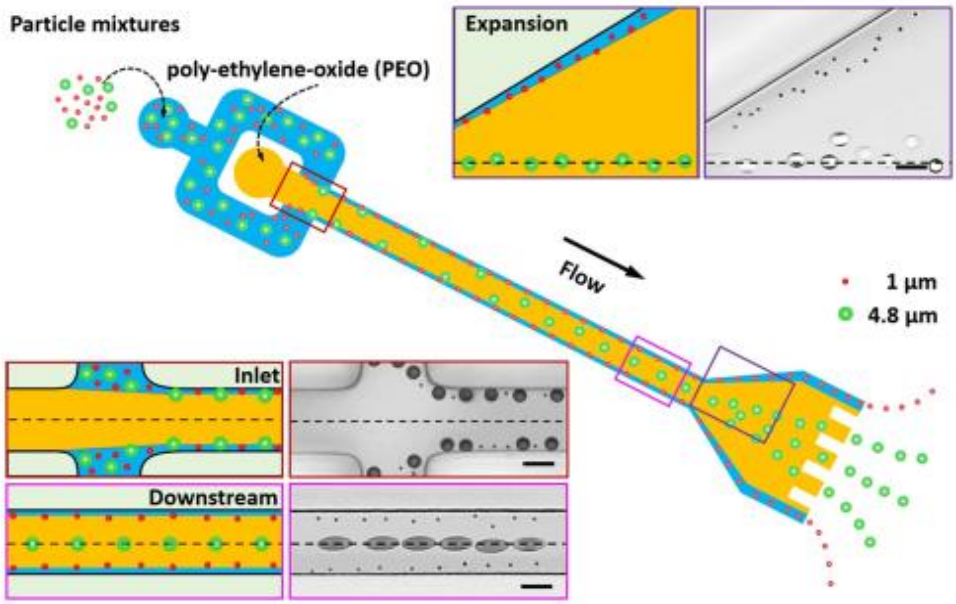

Figure 1-6 4.8 and 1 µm polystyrene particles are used in the experiment for size-based separation of polystyrene particles utilizing a co-flow of viscoelastic and Newtonian fluids. The lateral locations of polystyrene particles of various sizes at the inlet, downstream, and expansion zone are shown using schematics and experimental pictures with overlay images. The straight channel is 20 µm wide, whereas the scale bar is 10 µm broad. Reprinted with permission from Royal Society of Chemistry (Great Britain).[82]

In sheathless, Dean-assisted elasto-inertial focusing, device geometry and non-Newtonian rheology replace sheath flows to minimize dilution and simplify operation [83–85]. For instance, Zhou et al. [86] used reverse wavy channels that periodically invert Dean vortices to position cells/particles without sheath fluid, reliably focusing down to ~3 µm (with 1 µm alignment improvable by shrinking channel dimensions or adding viscoelastic media/auxiliary forces). Raoufi et al. [85] examined spiral microchannels with PEO solutions (1–17 µm particles) and showed that Dean

drag, together with fluid rheology, controls migration; notably, 1 μm particles did not focus well in 90 μm × 30 μm spirals, implying finer channels are needed. Complementing these, Bilican [87] demonstrated cascaded contraction–expansion structures, as in Fig. 1-7, with AR = 2 (contractions) and AR = 50 (expansions), constant height 10 μm, and widths of 20 μm/500 μm, achieving sheathless separation using 500–10,000 ppm PEO. Results demonstrated separation of 2 μm and 6 μm particles, and >98% isolation of Enterococcus from red blood cells was attained. Together, these studies highlight how Dean-enhanced secondary flows, channel width (blockage ratio), and viscoelasticity govern high-efficiency, sheathless focusing and separation.

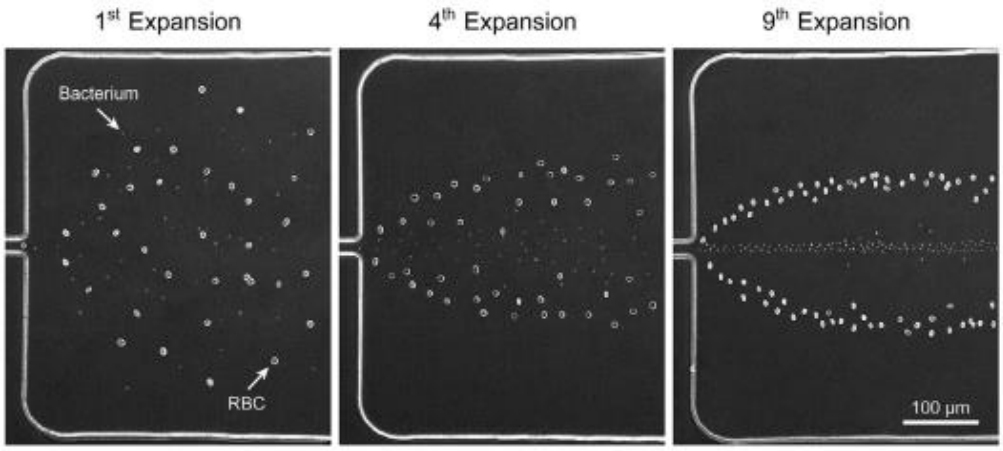

Figure 1-7 Separation of red blood cells (RBC) and Enterococcus faecalis was achieved using a 10000 ppm PEO 0.6 MDa concentration and a flow rate of 12 μl/min. Reprinted with permission from Elsevier. [87]

Even with advances in viscoelastic inertial focusing, existing sheathless techniques still struggle to focus submicron particles. For this reason, scientists are creating increasingly sophisticated microchannel geometries for further decreasing minimum blockage ratios necessary for successful sheathless, viscoelastic particle enrichment.

However, Suzuki et al. [88] showed that varying microchannel cross-sectional geometry substantially improves particle size discrimination for viscoelastic flows. Through a comparison

of rectangular channels of the same size but varying aspect ratios (AR ~ 0.5 and AR ~ 2.0) under elasto-inertial regimes as demonstrated in Figure 1-8. The higher aspect ratio channels produced clearer and more distinct equilibrium positions for particles differing by only a few micrometers in diameter, approximately doubling the resolution compared to lower aspect ratio channels. This enhancement was due to the modified balance between inertial and elastic lift forces arising from changes in velocity gradients within the channel cross-section. These findings highlight that adjusting microchannel cross-sectional profiles is a practical, passive method to enhance size-based particle sorting without external fields or sheath flows. Extending this, Raoufi et al. [89] combined experiments and simulations in PEO to show that increasing AR (W/H) drives a transition from single to double focusing bands, consistent with a relative reduction of elastic forces versus inertial effects; sharper corner "rigidity" further biases particles toward the midline. Their intricate cross-section improved resolution over conventional designs, enabling stable focusing of smaller particles (≈3–5 μm), highlighting aspect-ratio tuning as a passive, sheathless route to enhance size-based sorting.

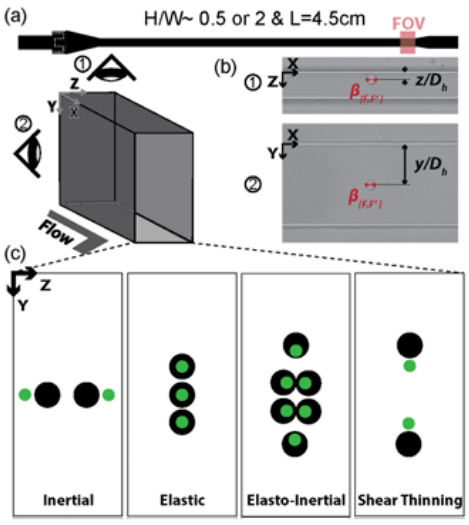

Figure 1-8 Experiment design overview: (a) the schematic depicting the experimental setup. (b) High-speed microscopic images of hydrodynamically focused MIN6 cells in the microchannels with the cross-

section of high and low aspect ratios. The high-speed videos were captured at the field of view (FOV) located at 4.5 cm from the inlet. The annotations indicate the dimensionless lateral focusing positions of cells y/Q_{2} and 2P and the blockage ratios,. (c) The schematics illustrate the cross-sectional cell focusing arrangements under the tested various flow conditions, namely, inertial, elastic dominant, elasto-inertial, and elasto-inertial with strong shear thinning. Reprinted with permission from the AIP Publishing.[88]

Specifically talking on *E.coli*, Liu et al. [90] demonstrated a considerable centreline focusing of *E. coli* at Reynolds numbers between approximately 0.07 and 0.7, using channels with AR = 4 and H=10 μm. Employing a denatured PEO (in glycerin) solution with an elasticity number around 100, their system partially pushed 1 μm-scale particles to the channel centerline. Worth mentioning, Liu et al. also used 1 μm beads for mimicking *E. coli*, observing similar focusing behaviors. This study also highlights the potential of viscoelastic microfluidics for precise bacterial manipulation and enrichment in diagnostic applications.

1.2.2.3 Challenges and Future Directions

Inertial microfluidics technologies have emerged as efficient, label-free platforms capable of processing of routine clinical samples such as blood, urine, and mucus, significantly streamlining laboratory workflows by reducing manual intervention. Leveraging size- and deformability-dependent inertial forces, inertial microfluidics devices have demonstrated superior performance compared to traditional methods in isolating rare cells, including circulating tumour cells (CTCs), and specific white blood cell subsets, all without reliance on fluorescent labels or biomarkers. This preserves cell viability and enhances the reliability of downstream analyses. Additionally, the use of viscoelastic carrier fluids extends inertial microfluidics capabilities down to the nanoscale, facilitating rapid and sensitive enrichment of extracellular vesicles and pathogenic microorganisms critical for timely diagnostics.

Overall, in this case, a detailed parametric study is still required to investigate the affecting parameters on particle motion inside microchannels with complex geometry. This study will help uncover how particles interact with the viscoelastic fluid under different conditions, guiding the optimization of particle enrichment techniques especially with a lower blockage ratio.

By harnessing the power of inertial microfluidics, *E. coli* particles can be efficiently enriched and concentrated, enhancing the sensitivity and speed of the LFA process. These enriched samples are then seamlessly integrated into lateral flow assays, enabling rapid and precise identification of *E. coli*. Finally, cutting-edge photothermal readers provide accurate and real-time results, revolutionizing the UTIs diagnosis and management.

Apart from all the above-mentioned benefits, the inherent simplicity of inertial microfluidics makes it easy to integrate with complementary on-chip operations, yielding "hybrid devices" that add in-line manipulation steps and deliver either higher enrichment efficiency or entirely new functions compared with inertial microfluidics alone. By embedding multiple unit operations on the same chip, these hybrids can bypass many of the off-chip pre- and post-processing steps that slow conventional workflows, making them attractive drop-in upgrades for existing pipelines.

For example, Ramachandraiah et al. [91] and Zhu et al. [92] inserted spiral inertial channels downstream of on-chip red-blood-cell lysis to isolate nucleated cells and white blood cells, respectively; the gentler hydrodynamics preserved cell viability while delivering higher purity at faster throughputs than density-gradient centrifugation, all with fewer manual steps.

Motivated by these precedents, an integrated workflow is supposed to be investigated in which an inertial microfluidic enrichment module is placed upstream of a lateral flow immunoassay (LFA), and the developed LFA is subsequently analyzed by an LFA reader.

1.2.3 LFA Readers: Overview and Applications

LFAs are widely used POC diagnostics that provide rapid, inexpensive detection of analytes such as proteins, pathogens, and antibodies in diverse sample matrices, including urine, saliva, and blood. Common examples include pregnancy tests, COVID-19 diagnostics, and applications in medicine, food safety, and environmental monitoring. LFAs operate on the principle of capillary action, where liquid samples migrate along a test strip and interact with immobilized reagents to generate a visible signal.

Despite their speed and ease of use, LFAs typically suffer from relatively high limits of detection. Enrichment pretreatment can reduce this limitation by concentrating the analyte prior to testing. Incorporating an LFA reader can further improve sensitivity and add quantitative capability, allowing faint or imperceptible signals to be measured accurately. Depending on the sensing technology employed, LFA readers can be categorized as colorimetric, fluorescence-based, magnetic, electrochemical, photothermal, or dual-signal systems [93].

1.2.3.1 Overview and Applications

Colorimetric readers are among the most widely used due to their simplicity, affordability, and ease of implementation. These readers read color change intensity on the test line, commonly due to selective reflectance of ambient light by colloidal gold or dyed latex particulates. [94] Color change intensity is often read with charge-coupled device (CCD) or complementary metal-oxide-semiconductor (CMOS) cameras, enabling a simple interpretation of test outcomes [95]. Commercially viable examples range from integrated products like the Clearblue® pregnancy test to recent spinoffs harnessing smartphone cameras with custom mobile applications for fast and transportable diagnostic tests [96]. However, the intrinsic limit of detection is generally not improved

by these implementations, which primarily standardize interpretation and data handling and remain constrained by assay chemistry and labeling. Fluorescence readers offer higher sensitivity compared to their colorimetric counterparts due to the measurement of fluorescent emission signals. After excitation with an appropriate lighting source, fluorescent particulates generate emission signals, which are read with optical filters, high-sensitivity sensors, often CCD or CMOS sensors. Fluorescence technology systems, like Alere's Triage® system [97], became popular due to their advantage of reading analytes at much lower concentrations. Recent advancements encompass readers using up-converting phosphors, which convert excitation in infrared into visible emissions, enabling further elevated assay sensitivity as well as improved assay stability. Despite their enhanced sensitivity, fluorescence readers using up-converting phosphors may suffer from weak emission intensity, require more sensitive detectors, and remain vulnerable to photobleaching and environmental quenching, all of which can limit throughput and quantitative accuracy. Furthermore, these systems depend on fluorescent particles that are relatively expensive and have limited shelf life, which further restricts their practicality for widespread or long-term applications.

Magnetic readers represent a particularly sensitive approach that utilizes magnetic particles as labels. The principle behind magnetic readers is the detection of magnetic fields generated by paramagnetic or superparamagnetic nanoparticles collected on test lines. Common sensors include giant magnetoresistive (GMR) and tunnel magnetoresistive (TMR) sensors, as well as inductive coils. Magnetic readers offer significant advantages, such as minimal interference from assay background colors, deep signal penetration, and the ability to concentrate analytes magnetically. A commercial example includes readers developed by MagnaBioSciences, demonstrating their effectiveness in clinical diagnostics [98]. Despite their advantages, magnetic readers can be limited

by the need for precise alignment of magnetic sensors with the test line, potential signal variation due to particle aggregation or uneven distribution, and the relatively high cost and complexity of sensor integration compared to optical systems.

Electrochemical readers offer another quantitative analysis approach by detecting shifts in electrical properties like voltage, current, or impedance produced from labels with incorporated metals or enzyme-coated particulates [99]. Commonly incorporating electrodes embedded within assay strips, electrochemical readers utilize a few simple electronic parts like potentiometers or galvanometers. Because of their simplicity and miniaturizable nature, electrochemical readers can be easily adapted for incorporation into field-friendly diagnostic units [100] A good example is assays using traditional glucose meters for quantitative measurement of biomarkers like prostate-specific antigen (PSA) [101]. Despite their portability and low cost, electrochemical readers may face limitations such as susceptibility to interference from sample matrix components (e.g., salts, proteins), limited multiplexing capability, and the need for precise control of assay conditions to maintain measurement accuracy and reproducibility.

Photothermal readers utilize the existing gold nanoparticles of low-cost LFAs for generating amplified thermal waves upon absorption of an incident light. These thermal signals, captured by infrared cameras or thermal detectors, allow quantification of analytes with high sensitivity. Due to their effective penetration depth, photothermal readers are particularly valuable when label particles are embedded within the assay membrane[102]. Advanced methods such as thermophotonic lock-in imaging (TPLI) have shown superior performance, significantly enhancing the limit of detection compared to traditional colorimetric methods, as they register amplified signals from a very small number of analyte-nanoparticle complexes that normally do not produce a detectable colorimetric signal [103]

Finally, dual-signal readers integrate two complementary detection techniques, for example, colorimetric and photothermal, or colorimetric and electrochemical approaches. Dual-mode detection overcomes the restrictions of a single-mode detection approach, offering more reliability, strength, and versatility in quantitative measurements [104]. Some examples are assays with dual-mode MnO_2-Au particles enabling both qualitative colorimetric measurement as well as quantitative photothermal detection, as well as smartphone platforms integrating color as well as detection of fluorescence for improving detection accuracy [105,106]

These advanced reader technologies significantly enhance the applicability and reliability of LFAs, enabling rapid, sensitive, and accurate diagnostics in POC settings, often integrated with portable and smartphone-based platforms. Given the strong enhancement in sensitivity offered by PT, this thesis employed lock-in thermography (LIT) to achieve an additional improvement in detection limit. By leveraging lock-in amplification, even weak PT signals from low-abundance analytes could be reliably extracted from background noise, thereby enabling more accurate and sensitive quantification than conventional or dual-mode readers.

1.2.3.2 LIT and its Use for Amplified Reading of LFAs

In LFA readers utilizing lock-in thermography, the LFA is typically illuminated with a modulated optical beam, often a laser diode with its power cycled on and off at some modulation frequency (e.g., 1 Hz). The wavelength of the optical excitation is chosen as the peak of light absorption by the gold nanoparticles used in the LFA due to the phenomenon of localized surface plasmon resonance (LSPR). Cyclic absorption of energy of this modulating excitation causes localized heating, generating a modulated temperature field (aka. a thermal wave field). Thermal waves propagate outward from an energy-absorbing sample with a characteristic depth determined by a modulation frequency and a material's thermal characteristics.

The propagation of this heat can be monitored with various methods. A well-known approach is photothermal radiometry (PTR) [107], in which an infrared sensor (or camera) monitors the cyclic infrared radiance of the heated surface after taking advantage of the Stefan-Boltzmann law, connecting radiance of emitted energy with surface temperature.

$$W = \varepsilon\sigma T^4 \tag{1-10}$$

The total radiant emittance from an interrogated point is denoted as W, σ as the Stefan-Boltzmann constant value of 5.67×10^{-12} W/(cm^2 K^4), and emissivity as ε.

Alternatively, as demonstrated in Figure 1-9, a heated zone above a sample can induce refractive index variations, creating a gradient responsible for defocusing probe beams passing in proximity to a sample surface, a phenomenon known as the mirage effect. Deflected probe beams can be monitored sensitively for the detection of a thermal gradient [108].

Additionally, periodic heating generates thermoelastic deformation on the sample surface, yielding mechanical vibrations or sound waves. Such subtle displacements can be monitored with microphones in photoacoustic detection, or with sensitive interferometric techniques. Lastly, thermal waves moving into a material like pyroelectric sensors create voltage responses proportional to temperature changes, a technique referred to as photopyroelectric detection [108].

Each of these detection methods offers its distinct sensitivity as well as depth-selectivity, and the selection of a method depends on sample properties, detection thresholds, as well as experimental demands. Of these methods, PTR is a commonly used approach that is also adopted in this thesis.

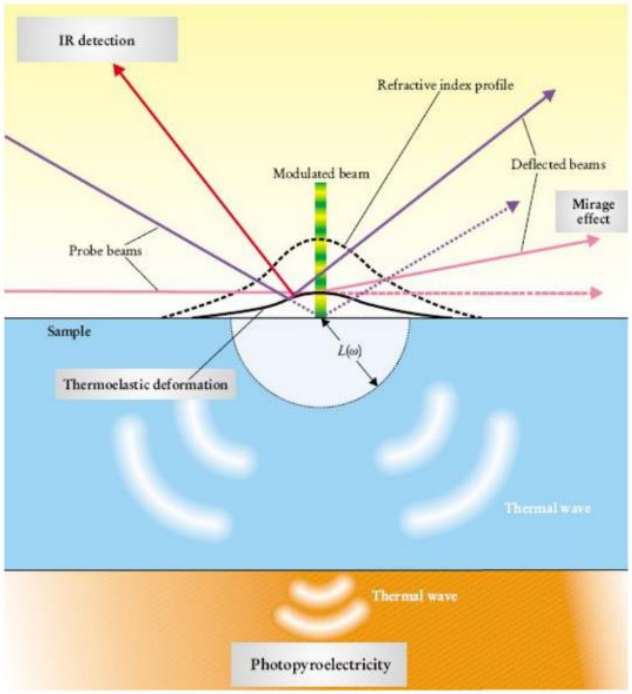

Figure 1-9 Schematic representation of different detection schemes [108]

A standard photothermal radiometric (PTR) arrangement entails the creation of a thermal wave field in the sample due to absorption of modulated optical radiation, either continuous-wave or pulsed. Radiometric detection often uses a cooled infrared sensor, a so-called liquid nitrogen-cooled mercury cadmium telluride (MCT) detector, for example, that measures fluctuations of sample surface temperature due to radiated infrared emission. Based on the Stefan-Boltzmann law, a minor sample temperature change (δT) generates a linear change of radiant emittance (δW), given by the relation:

$$\delta W = 4\varepsilon\sigma T^3 \delta T \tag{1-11}$$

Consequently, PTR systems are capable of reliably detecting temperature variations caused by subsurface features such as absorbers or defects, through non-contact interrogation of the sample's surface. Photothermal radiometry itself can be classified based on various criteria, including the optical excitation method, wavelength, and intensity. Generally, PTR employs two main excitation

schemes: pulsed excitation and continuous-wave (CW) excitation. In pulsed photothermal radiometry (P-PTR), a short, high-power optical pulse, lasting from milliseconds up to a few seconds depending on material properties, is directed onto the sample, followed by monitoring its thermal response with either a single infrared detector or an infrared camera (pulse thermography (PT)). Initially, the sample temperature rises sharply due to the energy absorption from the pulse. Subsequently, heat dissipates gradually into the bulk, causing the temperature-decay over time [109].

Nevertheless, if subsurface anomalies or defects are present in the sample, thermal conductivity at those locations is decreased, decreasing the rate of heat dissipation locally. Thus, defective spots are maintained at high temperature for a relatively longer time with respect to defect-free spots, creating characteristic cooling profiles. Such a contrast in dissipation rates is evident in thermal images, wherein defective spots are observed to be more luminous due to increased infrared emission. As a result, photothermal radiometry, with proper viewing of temperature profiles, offers sensitive as well as non-destructive subsurface feature as well as defect detection [110].

Several signal processing methods have been proposed to enhance the sensitivity and accuracy of photothermal radiometry. The most common approach involves subtracting the temperature decay profile measured over a semi-infinite, defect-free area from the temperature profiles observed over defective regions. This subtraction highlights the subtle, delayed cooling effects caused by subsurface anomalies [110]

P-PTR finds wide appeal in industrial non-destructive tests because of its fast measurement rate and simple interpretation. Nonetheless, it has some challenges as well: because thermal waves produced with short optical pulses inevitably consist of a broad distribution of frequency components, it becomes hard to distinguish from them the contribution of a given individual frequency. Also, because amplitude-based thermal responses are observed for a measurement with

a pulse, the observed values prove to be sensitive to optical excitation intensity non-uniformities, emissivity variations of surfaces, presence of ambient reflections, and various sample surface irregularities.

To address some of these limitations, frequency-domain photothermal radiometry (FD-PTR) emerged based on foundational theories introduced by Fourier in 1822, who demonstrated that heat conduction in solids can be effectively analyzed by decomposing thermal excitation into waves at distinct frequencies. [111] Building on this concept, Ångström introduced a temperature-wave method in 1863 to measure thermal diffusivity. In modern FD-PTR, the excitation source is typically a low-power, continuous-wave laser or light emitting diode (LED), amplitude-modulated at a single frequency. This creates a stable, spatially decaying thermal-wave field within the sample, precisely at the modulation frequency [112].

As opposed to the more straightforward pulse method, FD-PTR involves more advanced signal processing, often utilizing quadrature demodulation (lock-in detection) to pick up both amplitude and phase content of the signal being measured. Quadrature-based phase detection offers distinct benefits, particularly because the phase signal is emissivity-normalized and therefore more resilient to variations in excitation strength, emissivity, or surface finish. Lock-in thermography takes its FD-PTR principle into two dimensions using an infrared detector array, in effect an IR camera, instead of a point detector, allowing for spatial mapping of subsurface flaws with amplitude as well as phase sensitivity.

Despite the early promise of FD-PTR in non-destructive evaluation, its industrial use was initially limited due to the long measurement times required for surface raster scanning with single-point infrared detectors. This limitation was effectively overcome between the late 1970s and early 1990s through the integration of infrared cameras into the FD-PTR system, giving rise to LIT. By

imaging larger surface areas simultaneously, LIT significantly increased inspection speeds and made frequency-domain methods practical for industrial-scale defect detection [113–116].

A literature survey of photothermal radiometry and lock-in thermography demonstrates that while these methods are well established for non-destructive testing of industrial materials [117–120], their uses for biomedical diagnostic imaging are quite confined, indicating an arena that would benefit from more research.

The lock-in demodulation algorithm acquires image sequences at a specified frame rate with concomitant acquisition of corresponding in-phase and quadrature reference signal values. It then performs a calculation of the weighted average of image sequences, with each sequence length precisely an integer multiple of a modulation period. Such weighted frames are added to obtain in-phase (S_0) and quadrature (S_{90}) images.

Mathematically, the process involves multiplying the captured signal by synchronized sinusoidal reference signals (mixing), followed by low-pass filtering to remove high-frequency components. As described by the equation below, this approach allows precise extraction of the amplitude and phase components of the original thermal-wave signal:

$$\begin{cases} \boldsymbol{sin}(\omega ot) \times A\boldsymbol{sin}(\omega ot + \phi) \\ \boldsymbol{sin}(\omega ot + 90) \times A\boldsymbol{sin}(\omega ot + \phi) \end{cases} \longrightarrow \begin{cases} \frac{A}{2}[cos(\phi) - cos(2\omega ot + \phi)] \\ \frac{A}{2}[sin(\phi) - cos(2\omega ot + \phi + 90)] \end{cases}$$

$$\begin{cases} \frac{A}{\sqrt{2}}[\boldsymbol{cos}(\phi) - \boldsymbol{cos}(2\omega ot + \phi)] \\ \frac{A}{\sqrt{2}}[\boldsymbol{sin}(\phi) - \boldsymbol{cos}(2\omega ot + \phi + 90)] \end{cases} \longrightarrow \begin{cases} S0 = \frac{A}{\sqrt{2}}\boldsymbol{cos}(\phi) \\ S90 = \frac{A}{\sqrt{2}}\boldsymbol{sin}(\phi) \end{cases}$$

$$\longrightarrow A = \sqrt{(S0)2 + (S90)2}\,, \phi = \boldsymbol{arctan}(S0/S90)$$

This processing ensures accurate and noise-robust extraction of thermal-wave information from the measured images.

Recent advancements in LFA reader technologies have aimed to overcome the limitations of conventional visual detection methods, particularly the poor sensitivity and lack of quantitative output at low analyte concentrations. To address these challenges, photothermal detection mechanisms have been increasingly integrated into LFA platforms. These approaches convert heat generated by nanomaterial labels into measurable thermal signals, allowing for more sensitive and quantifiable analyte detection.

Photothermal strategies have also been directly applied to bacterial detection, particularly in the context of food and water safety or clinical diagnostics. Shirshahi et al. [121] demonstrated a novel LFA platform employing reduced graphene oxide (rGO) as a photothermal label to detect *Escherichia coli* O157:H7. Due to its high light absorption and efficient heat conversion properties, rGO significantly enhanced the thermal signal generated at the test line, enabling a linear detection range from 5×10^5 to 5×10^7 colony-forming units per milliliter (CFU/mL). This represented a tenfold increase in sensitivity compared to conventional visual readouts. In this study, the detection relied on a simple temperature-rise measurement by turning on a laser for 60 s and monitoring the bulk heating response. While effective in showing a relative enhancement, this approach is susceptible to external variations such as ambient temperature changes or airflow, which can strongly influence the absolute signal. Specificity analysis confirmed the platform's ability to distinguish the target strain from non-specific bacterial species, thereby validating its suitability for rapid pathogen detection, though the absence of modulation-based techniques like lock-in limits robustness. This work is particularly relevant for applications such as urine-based

diagnostics for urinary tract infections (UTIs), where sensitive and selective detection of bacterial agents is critical.

One notable development is the TPLI platform introduced by Ojaghi et al. [103] **(** Figure 1-10 **)**, which utilizes frequency-domain imaging to capture thermal emissions produced by plasmonic gold nanoparticles upon modulated photothermal excitation. This method enabled the detection of subtle signals invisible to the naked eye, achieving performance comparable to fluorescence and surface-enhanced Raman scattering (SERS) while maintaining a simpler and more accessible system configuration. The integration of TPLI into LFAs thus represents a promising strategy for enhancing the analytical performance of point-of-care diagnostics.

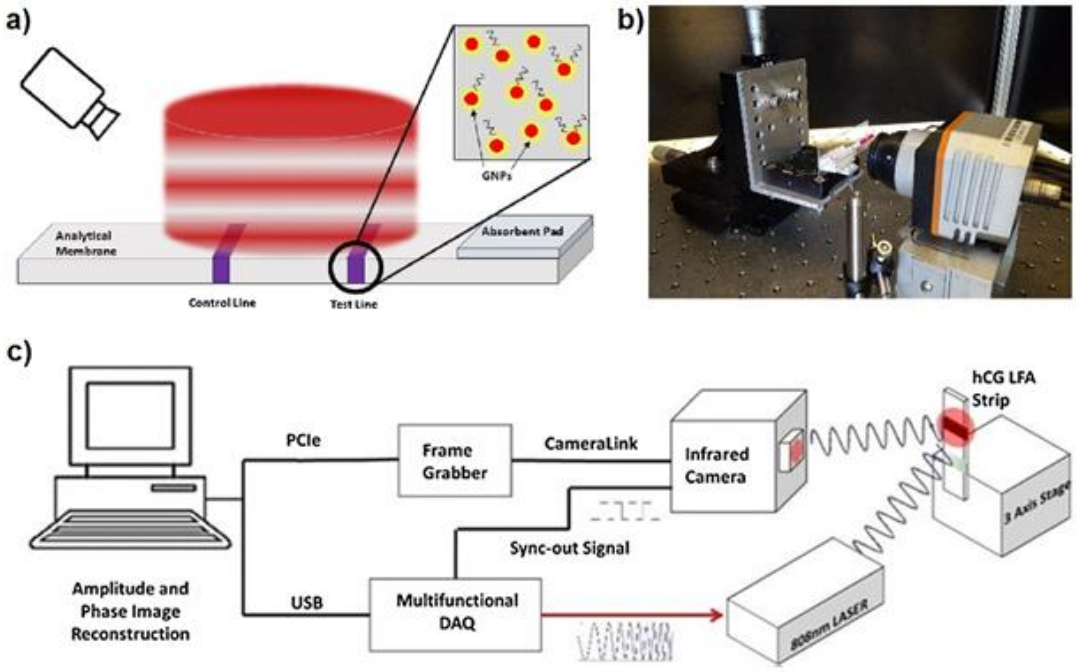

Figure 1-10 Schematics illustrating (a) the working principle and (b, c) the system components of TPLI used for the interpretation of LFIA results. Reprinted with permission from Springer [103]

In a related effort focused on serological testing, Thapa et al. [122] developed a handheld thermo-photonic device capable of quantifying anti-SARS-CoV-2 antibodies, which is depicted in Figure

1-11. The system was based on the detection of infrared thermal radiation emitted from gold nanoparticles upon laser excitation, enabling discrimination among varying concentrations of monoclonal IgG antibodies targeting the viral spike protein. Compared to laboratory-based methods such as enzyme-linked immunosorbent assay (ELISA), chemiluminescent immunoassays (CLIA), and neutralization tests, the proposed device offered significant advantages in terms of portability, cost-effectiveness, and speed of analysis [123]. Although initially intended for monitoring immune responses in COVID-19 patients and vaccine recipients, the underlying detection strategy holds promise for broader applications, including multiplexed detection of other pathogens or biomarkers in field-deployable settings.

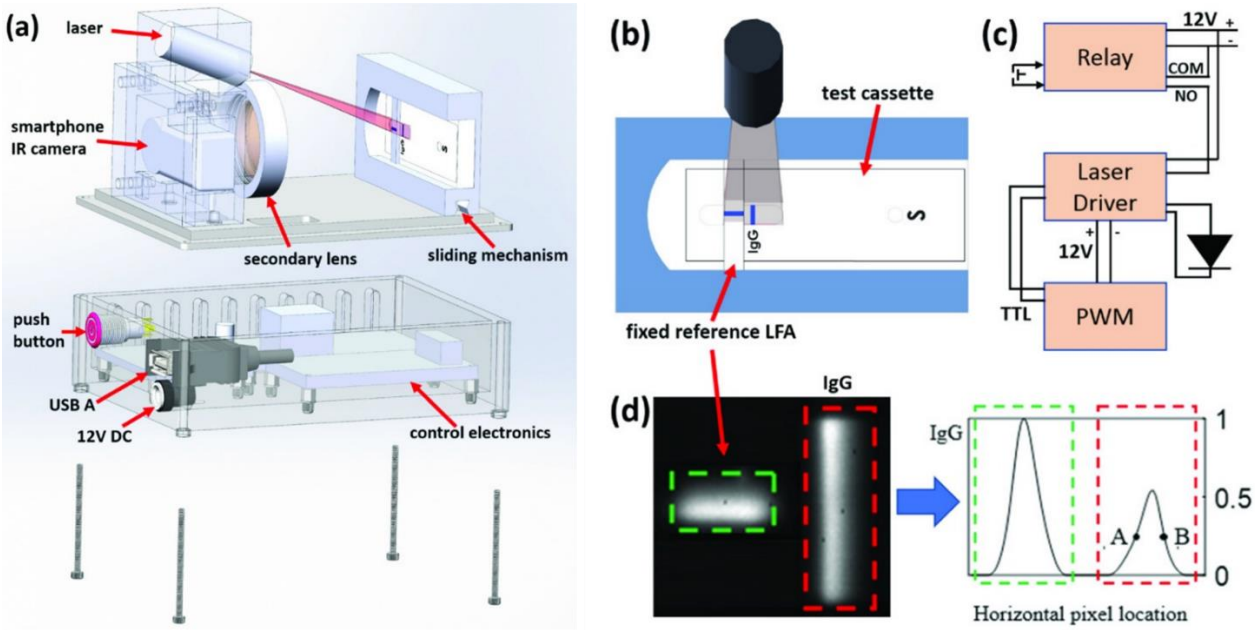

Figure 1-11. (a) Exploded schematic of a portable thermo-photonic lock-in thermography (TPLI) device. (b) Laser alignment with the test cassette and reference LFA. (c) Compact electronic control circuit. (d) Representative amplitude image used for normalization and signal quantification. Reprinted with permission from IEEE. [122]

Finally, the feasibility of low-cost, miniaturized photothermal readers was explored by Hayden et al. [124], who developed an Arduino-based photothermal radiometry (PTR) device capable of

frequency-domain signal processing. The system incorporated a low-cost single-element far-infrared sensor and an intensity-modulated laser, achieving a tenfold improvement in the limit of detection (LOD) for tetrahydrocannabinol (THC), reducing it from 25 ng/mL to 5 ng/mL. Additionally, the device enabled semi-quantitative categorization of analyte concentration. With a total material cost of approximately 51 USD, this proof-of-concept demonstrated that sophisticated photothermal analysis can be achieved in compact, affordable formats suitable for point-of-need diagnostics. While the initial application targeted small-molecule drug detection, the underlying principles are broadly applicable to infectious disease diagnostics, including bacterial targets.

Although research has investigated LFAs' improved sensitivity and quantitative potential with photothermal properties using various materials, for example, *E. coli* detection with rGO and gold nanoparticles (AuNPs) for wider targets, no research appears to have especifically investigated the PT detection of *E. coli* with LFAs containing AuNPs. Notably, the few existing photothermal LFA approaches do not employ lock-in detection; instead, they rely on observing the absolute temperature rise. This method is inherently prone to environmental fluctuations, as results can vary significantly depending on ambient temperature or airflow conditions (e.g., cold vs. hot days or drafty environments), in contrast to lock-in thermography, which isolates modulated thermal signals and offers robustness against such variability. Such a gap indicates a potential for further investigation into the potential of using LIT-PT detection of AuNPs to improve *E. coli* detection with commercial LFAs. Such a study could prove fruitful in terms of improving sensitivity as well as specificity for more reliable LFA-based rapid detection of pathogens in diverse applications.

1.3 Scientific and Technological Gaps

E. coli-induced UTIs are both common and severe, yet the traditional methods for detection, such as culturing and urine microscopy, face significant challenges, particularly in POC settings. These methods are hampered by slow processing times, reliance on skilled technicians, limited detection capabilities, and insufficient specificity for *E. coli*. While recent advancements in POC technology have sped up processing, they still heavily depend on technician involvement. LFAs are a quick, portable, and cost-effective alternative, but their high Limit of Detection (LOD) is a major concern. This research aims to enhance LFAs by integrating microfluidic enrichment with a photothermal LFA reader, thus improving their sensitivity while preserving their inherent advantages.

This thesis addresses, in an attempt towards integrated manner, the fundamental and applied questions that determine whether *E. coli* can be concentrated on-chip and read out sensitively on an LFA in clinically relevant matrices. It first interrogates how confinement ratio (β), channel aspect ratio, and zigzag-induced secondary flows govern lateral focusing and recovery of micron-scale objects in sheathless visco-inertial and PEO-assisted viscoelastic regimes, and then establishes practical geometric and flow operating windows that enable reproducible manipulation and concentration of ~1 μm *E. coli* at microliter-per-minute throughputs without sheath fluids or external fields. The work quantifies how microfluidic pre-enrichment factors translate into photothermal signal gains at the LFA test line under fixed assay conditions. Analytical performance of the lock-in photothermal reader is characterized in urine-relevant matrices in terms of dynamic range, repeatability, and coefficient of variation, lot-to-lot robustness, and improvement over intensity imaging.

1.4 Thesis Statement and Objectives

This work focuses on reducing the sample volume to concentrate bacteria present in larger-volume fluids, thereby effectively increasing the bacterial concentration in smaller samples. Traditional enrichment methods, which are impractical for integration into portable diagnostic platforms due to their size, are compared with microfluidic devices that offer the benefits of portability and cost efficiency. However, enriching small particles like bacteria remains a significant challenge. This approach uses viscoelastic forces to enhance the isolation and concentration of these small bacteria.

Additionally, photothermal techniques are utilized in the LFA reader to detect subtle temperature changes resulting from binding events on the test strip. This provides a more sensitive and accurate quantitative analysis than traditional visual methods. By integrating these technologies, this research aims to overcome the current limitations of existing diagnostic approaches for *E. coli* in UTIs, leading to more effective and precise tools. Although the current device has not yet been translated into a POC format, the methods developed here establish the foundation for future POC adaptation. This thesis is designed with these objectives in mind. To achieve this goal, the work is organized into four objectives as discussed below.

Objective 1: *E. coli bacteria enrichment of at least one order of magnitude within an hour*

The progression toward this objective is organized into the following milestones:

Stage 1: Characterization of Particle Focusing Across Channel Geometries

The focusing behavior of 1 μm and 4 μm fluorescent particles will be systematically investigated in various microchannel designs, including straight, symmetric zigzag, and

asymmetric zigzag geometries. A range of channel widths and heights will be tested to evaluate the influence of aspect ratio and hydraulic diameter. Viscoelastic effects will be induced by incorporating 1000 ppm PEO into the carrier fluid. Experiments will be conducted at flow rates up to 25 μL/min to establish size-selective focusing conditions, which will serve as a proxy for *E. coli* behavior.

Stage 2: Mapping Particle Focusing Behavior to *E. coli* Positioning

The focusing profiles obtained from particle experiments will be compared with the behavior of *E. coli* under equivalent flow and geometric conditions. This comparison will help identify the most appropriate surrogate particle and focusing regime for simulating bacterial motion and enrichment inside the channels.

Stage 3: Design and Integration of Multi-Outlet Separation Systems

Microfluidic devices will be fabricated with three outlets to enable continuous-flow separation of the focused stream. The central outlet will be designed to capture the middle 10% of the channel width, which corresponds to the expected position of focused particles or bacteria. To ensure balanced flow across all outlets, hydraulic resistance will be tuned by modifying the outlet lengths and cross-sectional dimensions accordingly.

Stage 4: Viability Assessment of Enriched Bacteria

To confirm the biological integrity of enriched *E. coli*, viability will be assessed by plating samples on LB agar and enumerating CFU. Sample groups include 0, 1000 ppm, and 4000 ppm PEO for comparison. This step will validate that the enrichment process preserves bacterial viability for subsequent detection or culturing steps.

Stage 5: Visual Enrichment Assessment Using LFA

The effectiveness of enrichment will be evaluated by applying the collected *E. coli* samples to lateral flow assays. The resulting test line intensities will be compared with those of the unprocessed input samples, allowing for the estimation of enrichment fold. This approach provides a rapid, application-relevant assessment of enrichment performance under practical conditions.

Objective 2: *Design and Adjustment of Photothermal Reader for E. coli specific LFAs*

Photothermal imaging will be employed as an advanced reader to improve the limit of detection (LOD) and enable quantitative analysis in lateral flow assays (LFAs). By leveraging light absorption and heat generation from gold nanoparticles, photothermal imaging enhances the sensitivity of LFAs and produces thermal signals that can be measured with high precision. This integration provides a promising approach for quantitative diagnostics with significantly improved sensitivity compared to colorimetric detection. The following milestones outline the phases of this objective:

Stage 1: Compatibility Testing with Viscoelastic Samples

Since the enriched *E. coli* samples originate from viscoelastic microfluidic flows containing PEO, it is essential to verify the compatibility of LFAs with these non-Newtonian solutions. Tests will be conducted to ensure that PEO does not interfere with capillary flow, reagent rehydration, or signal development. This step ensures that LFAs maintain reliable performance when used with viscoelastic samples.

Stage 2: Experimental Investigation of *E. coli* Concentrations

A broad range of *E. coli* concentrations, from 10 CFU/mL to 10^5 CFU/mL, will be tested on LFAs to assess detection sensitivity and quantitative response. Each assay will be imaged using a

thermo-photonic lock-in (TPLI) technique, which measures modulated thermal signals corresponding to the nanoparticle-based test and control lines.

Stage 3: Data Acquisition and Processing Framework

Thermal data will be captured using a custom-developed LabVIEW interface designed for precise synchronization of laser modulation and image acquisition. The resulting image sequences will be processed using MATLAB to perform lock-in demodulation, extract amplitude and phase information, and quantify signal intensity. This integrated workflow allows for robust, noise-resistant measurements of thermal responses across different bacterial concentrations.

Stage 4: Quantification and Limit-of-Detection (LOD) Analysis

Statistical analysis will be conducted to determine the LOD of the photothermal LFA reader and to compare signal intensities across the tested *E. coli* concentration range. Quantitative calibration curves will be generated by plotting photothermal amplitude versus bacterial concentration, providing a reliable framework for future diagnostic applications in health and environmental monitoring.

Objective 3: *Coupling Microfluidic Enrichment and Photothermal Readers in Lateral Flow Assays*

In this study, another aim is to study the feasibility of integration of microfluidic enrichment and photothermal readers into lateral flow assays to create a more effective diagnostic platform for detecting *E. coli* in UTIs. This integration will involve the use of microchannels for upstream enrichment of the sample before spiking to the LFA. To achieve this, a coupled diagnostic system was established, where the initial sample undergoes microfluidic enrichment to increase the target concentration before being applied to the LFA strip and analyzed through photothermal

thermography for quantitative detection. This innovative approach is expected to significantly enhance the sensitivity and specificity of existing LFA-based UTI diagnostics, and while the current prototype is not yet a fully POC device, the framework developed here establishes the foundation for future POC translation.

1.5 Thesis Outline

This thesis consists of 4 chapters, starting with an introduction to UTI and microfluidic particle focusing, followed by an overview of the underlying physics of the LFA readers and photothermal detection. In the second chapter, experimental methods and materials utilized in this thesis are reviewed, including the microdevice fabrication, solution preparation, and particle analysis methods, as well as photothermal LFA reader setup components and the preparation of biological samples. The third chapter establishes elasto-inertial focusing design rules for viscoelastic (1000 ppm PEO) flows by testing 1 µm and 4 µm surrogates and GFP-*E. coli* across straight, symmetric-zigzag, and asymmetric-zigzag microchannels and implementing a multi-outlet architecture that achieves ∼10-fold of particle enrichment (Obj. 1). Later, it validates *E. coli* enrichment and improves the visual LOD of LFAs from ~5×10^4 to ~5×10^3 CFU mL^{-1} after enrichment within ∼60 min. Finally in chapter four, it explains development of a portable lock-in photothermal LFA reader with a Python acquisition and MATLAB analysis pipeline, characterizes concentration response from 0–10^7 CFU/mL (Obj. 2). Also, it investigates integration of the enrichment module and photothermal reader to deliver quantitative readouts at clinically relevant concentrations ending up achieving photothermal LODs of 10^3 CFU mL^{-1} without enrichment and 10^2 CFU mL^{-1} with pre-enrichment (Obj. 3). Chapter five summarizes contributions, limitations, and future directions.

Chapter 2

2 Materials and Methods

This chapter reviews the material preparation and experimental methods used throughout this thesis. It begins with the design and fabrication techniques for microfluidic devices, followed by the methods for solution preparation. The experimental setup is then described, and the data analysis approach is explained.

2.1 Microfluidic Device Fabrication

2.1.1 Material and Chemicals

To study particle behavior, viscoelastic PEO solutions were created by dissolving PEO powder (Mw = 2×10^6 Da, Sigma-Aldrich, USA) in DI water at concentrations of 0 ppm (DI water), 500 ppm, and 1000 ppm. These solutions were stirred continuously for 12 hours at room temperature at 350 rpm using a magnetic stirrer (Thermo Scientific- SP88857104, Canada).

The rheological properties of the PEO solutions were characterized by Nikdoost at al. [125] with results summarized in Table 2-1. Both 500 ppm and 1000 ppm PEO solutions showed shear-thinning behavior (viscosity decreasing at higher shear rates), and the 1000 ppm solution consistently exhibited higher viscosity, confirming concentration-dependent viscoelasticity.

Table 2-1 Detailed results of the rheological characterization of PEO solutions: (Viscosity of PEO solutions at different shear rates (mPa.s))

PEO concentration / Shear rate (1/s)	500 ppm	1000 ppm
99.3	1.93	2.73
125	1.82	2.58
198.2	1.72	2.34
249.5	1.67	2.26
395.1	1.62	2.09
622	1.5	1.89
783.8	1.47	1.84
1240.7	1.46	1.77
1563.7	1.4	1.73
2469	1.39	1.66
3121.6	1.37	1.64
4945.6	1.33	1.59
7850.4	1.38	1.64
9880	1.35	1.6

Particles of two different sizes were used: 1.12 µm (~1 µm, CM-50-10, 2.5% w/v) and 3.93 µm (~4 µm, CM-53 100-10, 1% w/v), both nile red fluorescent with a density of 1.05 kg/m³, supplied by Spherotech Inc., USA. Each solution was prepared to have a particle concentration of approximately 10^6 particles/mL. Oakey et al.[126] systematically investigated the influence of particle concentration on inertial focusing in microchannels and reported optimal performance at approximately 0.1% (w/v), with device effectiveness improving as concentration increased within the examined range. In comparison, the highest concentration used in this study, 10^6 particles/mL, corresponds to a volume fraction of only 0.00335% for 4 µm beads and 0.000052% for 1 µm beads, values that are more than an order of magnitude lower than the lowest concentration range where Oakey et al. observed interaction-driven effects. These results clearly place the studied system well within the dilute regime, indicating that particle–particle interactions are negligible and that focusing behavior will remain unchanged even under further dilution. It is worth mentioning that the manufacturer noted some size variation in the products, which could lead to uncertainties and affect accuracy.

2.1.2 Biological Materials and Culture

E. coli GFP50 bacteria were cultured from a source colony. One colony was added to 10 mL of LB broth solution (Sigma Aldrich, USA) and incubated at 37°C with stirring at 240 rpm for 24 hours. The resulting bacterial solution was then serially diluted with LB solution to achieve a concentration of 10^3- 10^4 CFU/mL.

All equipment and consumables were sterilized prior to use. Sterilization was performed by autoclaving for items that tolerate heat, and by treatment with 70% ethanol or ultraviolet exposure for components that are sensitive to heat and the surfaces. All manipulations that involved live bacterial cultures, including preparation of serial dilutions, plating, and liquid transfers, were

conducted inside a certified Class II biological safety cabinet to maintain aseptic conditions and minimize contamination. Cabinet surfaces were disinfected before and after each session, and the blower was run to establish stable laminar airflow. Sterile tips, tubes, and media were handled with gloved hands, and gloves were changed and disinfected each time hands were taken out of the safety cabin. Waste was collected in approved containers and autoclaved before disposal in accordance with institutional biosafety procedures.

Serial dilution [127], a gold standard methodology for enumerating microorganisms globally, involves the systematic reduction of a known or unknown entity (such as a solute or organism) through successive re-suspension in fixed volumes of a liquid diluent (blanks). This technique is essential for obtaining manageable concentrations of desired organisms and is complemented by Petri dish streaking and spreading, among other microbiological plating techniques. In serial dilution, a 1 mL aliquot of the stock solution was added to 9 mL of LB in tube 1, creating solution 1. This process was repeated by transferring 1 mL from solution 1 to tube 2, and so on, with each step diluting the stock concentration by a factor of 10. Tubes 6, 7, and 8 of the serial dilution were then cultured on LB+Agar (Sigma Aldrich, USA) petri dishes to determine their concentration. To prepare the LB+Agar plates, 1 L of deionized (DI) water was measured, and the LB+Agar powder was added to it. The mixture was shaken until the powder was completely dissolved, then sterilized and returned to the biosafety cabinet. As the solution cooled, it began to solidify; therefore, it was dispensed into sterile plates within 15 minutes. A volume of 25 mL of solution was pipetted into each plate. The filled plates were left in the biosafety cabinet for 3–4 hours to cool and solidify, after which they were sealed with silicon tape and stored in the refrigerator for further use.

Spread plating, which does not further dilute samples, uses a sterile plastic L-shaped cell spreader (FisherBrand, catalog No. 14-665-230, USA) to distribute an aliquot of suspension media

across an entire Petri dish. A 100 µL aliquot from each of tubes 6, 7, and 8 was spread on Petri dishes in triplicate to ensure proper distribution. The dishes were then incubated at 37°C for 24 hours. The colonies that grow on the spread plate originate from single cells, and counting these colonies provides an estimate of the number of colony-forming units per milliliter (CFU/mL). To ensure a reliable measurement, at least one of the cultured dilutions should have a bacterial count between 30 to 300 CFUs. The three dishes within this range were then counted. Counts exceeding 300 colonies were considered too high to count (THTC), and counts below 30 were too low to count (TLTC). Finally, back calculations were performed to determine the concentration of the original source tube.

The effect of PEO on bacterial growth and viability was tested. An LB solution was prepared, and polyethylene oxide was added to reach a concentration of 4000 ppm. A sterile magnetic stir bar was placed in the flask, the mixture was sterilized, and it was left to stir overnight to ensure that polyethylene oxide fully dissolved in the LB solution. In parallel, a second LB solution without polyethylene oxide was prepared. On the following day, all manipulations were carried out in a safety cabinet to maintain sterility. The 4000 ppm LB with polyethylene oxide was diluted with plain LB to obtain a 1000 ppm LB with polyethylene oxide. The main *E. coli* culture was then serially diluted, using the corresponding diluent for each condition, so that LB alone was used for the control plates, LB with 1000 ppm polyethylene oxide was used for the 1000 ppm plates, and LB with 4000 ppm polyethylene oxide was used for the 4000 ppm plates. For each condition, the full serial dilution and plating procedure was performed independently, plates were incubated at 37° C for sixteen to eighteen hours, and colonies were enumerated as colony-forming units per plate. The results are presented in the next paragraph.

2.1.3 Microfluidic Enrichment Device Design

Various microfluidic channel geometries were utilized for parametric studies of particle and bacteria focusing and enrichment in this thesis. As in Figure 2-1, three types of microchannel geometries were examined: straight, symmetric zigzag, and asymmetric zigzag, all with an effective length of 8 cm, constrained by the maximum size of the available silicon wafers. The symmetric and asymmetric zigzag microchannels each contained 21 zigzag loops. In the symmetric zigzag, each side measured 1.8 μm, while in the asymmetric zigzag, the shorter arm was 0.9 μm and the longer arm was 2.7 μm. These sizes were chosen considering the size limitations for the straight channel (wafer size = 4 inch) and the fact that channel length was fixed for all geometries. The angles between the zigzag arms, both symmetric and asymmetric, were 60 degrees.

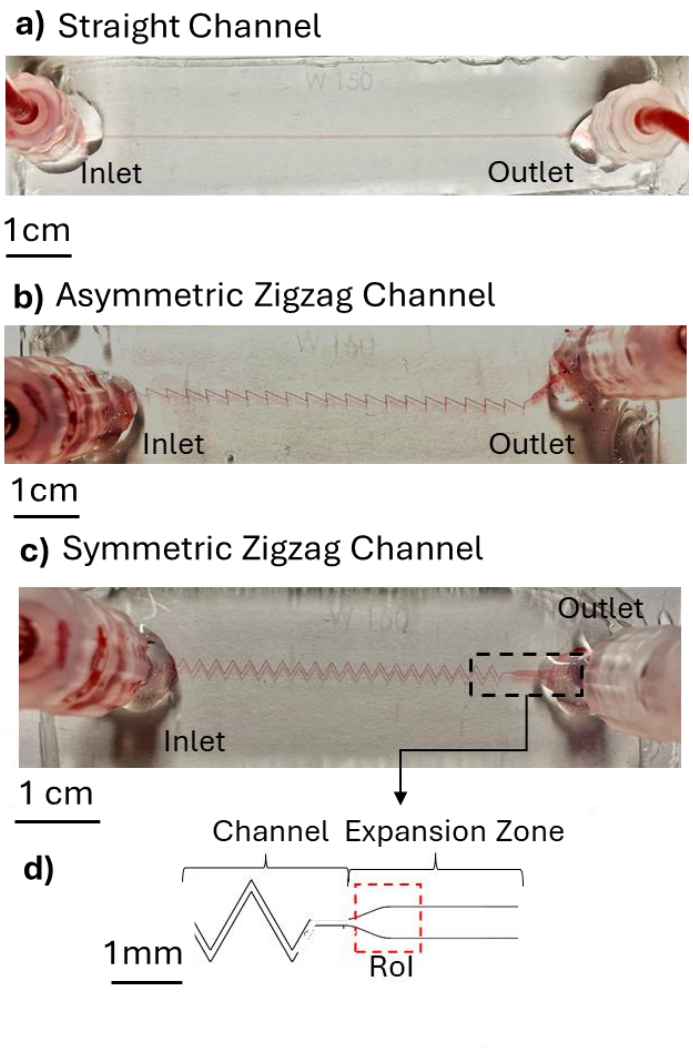

Figure 2-1 Microchannel with dimensions of 75 µm × 45 µm and a total length of 8 cm, fabricated in three geometries: (a) straight, (b) asymmetric zigzag, and (c) symmetric zigzag, each containing 21 zigzag loops with 60° angles. (d) Expansion zone at the channel outlet with a width of 800 µm and the region of interest (RoI).

Different combinations of height (H = 25, 45, 75 µm) and width (W = 25, 45, 75 µm) were tested to investigate the effects of AR and D_h. The expansion zone, designed to observe particle behavior before entering the outlet after being influenced by inertial forces in the microchannel, had a width of 800 µm.

For 4 μm particles, a blockage ratio of approximately β=0.04–0.07 is targeted. This range is widely reported as the minimum effective regime for reliable focusing and subsequent enrichment in viscoelastic and/or zigzag microchannels, with β≈0.07 often cited as the practical threshold for inertial focusing in straight channels in Newtonian (water) flows [128]. For 1 μm particles, achieving β of 0.03, known to be the minimum effective blockage ratio, was not feasible within fabrication, cost, and pressure-drop constraints; therefore, the smallest manufacturable channel dimensions is selected to maximize β and preserve the highest possible confinement, thereby promoting focusing and enriching performance despite operating below the canonical threshold. Moreover, these dimensions were designed to yield comparable aspect-ratio values (AR ≈ 0.5, 1, and 2) across both particle sizes, enabling direct comparison of focusing behavior under geometrically consistent conditions.

After studying particle behaviour through the region of interest (RoI), as shown with a red box in Figure 2-1-d, the best performing channels are chosen, and redesigned to have 3 outlets to enrich the initial sample by collecting the mid 10 % of the fluid that contains focused particles or bacteria and letting out the rest of the solution as waste.

As depicted in Figure 2-2, each device featured one inlet and three outlets, with 10% of the channel width designated to the center outlet and 45% of the flow collected independently from both the left and right sides. As seen in Table 2-3, using (2-1), the hydraulic resistance of each division specific to each channel height was calculated [129].

$$R \approx \frac{12\mu L}{wh^3} \frac{1}{1 - 0.63\left(\frac{h}{w}\right) + 0.053\left(\frac{h}{w}\right)^5} \tag{2-1}$$

Because the outlet sections are comparatively wide, the resulting wall shear rates at the tested flow rates are low. Accordingly, the apparent viscosity of the 1000 ppm PEO solution was treated

as constant and set to 2.8 mPa.s for all outlet-region calculations (Table 2-1). The channel outlet was designed as seen in Figure 2-2 with the lengths adjusted as in Table 2-2, so that all the segments had the same resistance, which helps the device have an equal pressure difference.

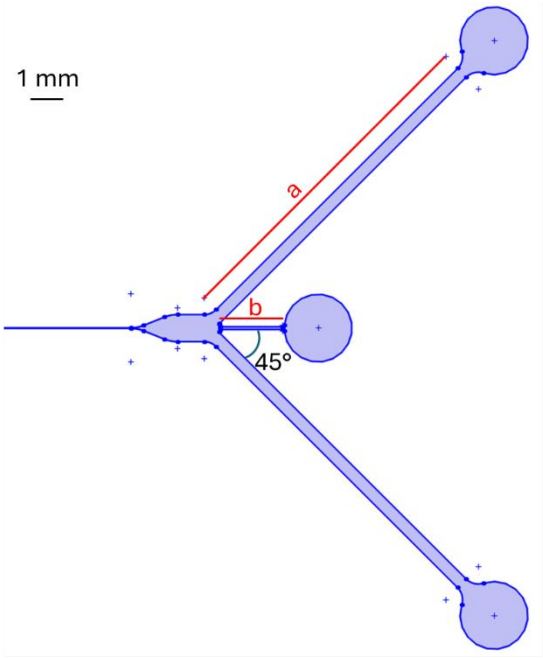

Figure 2-2 Schematic of the Y-shaped microchannel outlet with adjusted branch lengths to ensure equal hydraulic resistance in each pathway. The primary branch length (a) and lateral offset (b) are tuned at a 45° bifurcation angle to balance flow distribution.

Table 2-2 Geometric parameters of the microchannel design shown in Figure 2-2

Channel W (μm)	**Channel H (μm)**	**a (mm)**	**b (mm)**	**R_a**	**R_b**
25	25	10	1.85	$R \approx 6.2\times10^4$ Pa·s/μL	$R \approx 6.2\times10^4$ Pa·s/μL
25	45	10	4.40	$R \approx 1.1\times10^4$ Pa·s/μL	$R \approx 1.1\times10^4$ Pa·s/μL

2.1.4 Device Fabrication

The replication molds were fabricated using photolithography, and the microfluidic devices were fabricated using soft lithography. As the whole process is illustrated in Figure 2-3, the master molds were prepared in two steps: first, the suitable photoresist material from the SU-8 2000 photoresist series (MicroChem Corp., USA) was spin-coated onto silicon wafers (Wafer World Inc., USA). Initial preparation involves cleaning a 4-inch silicon wafer. The wafer undergoes sequential treatments: a 4-minute immersion in acetone, followed by blow drying and subsequent drying on a hot plate for 4 minutes. After allowing sufficient cooling for 4 minutes, this cleaning process is repeated using an isopropyl alcohol (IPA) bath. After cleaning, an Oxygen plasma (Harrick Plasma Inc., USA) pre-exposure followed, and afterward the negative photoresist was spin-coated. Depending on the target channel height, spin speed, UV dose, and bake times were adjusted, as explained in Table 2-3. For example, if a mold is needed for a 25 µm high channel, the spin coating was done at 3000 rpm for 30 s using SU8-2025. The photoresist was pre-exposure baked on a hotplate at 65°C for 1 minute and then for 5 minutes at 95°C. Pre-baking made the resist ready for UV exposure up to 150 mJ/cm² with a photomask (ArtnetPro Inc., USA) and a UV exposure system having an exposure gap of 0.4 mm (UV-KUB 2, KLOE, France). Post-baking was performed for 1 minute at 65°C and 5 minutes at 95°C before developing the master mold in SU-8 developer. A final hard bake at 200°C was subjected to the silicon master mold for 10 minutes. Microchannel geometries were examined by measuring width and height at five distinct cross-sections using 10× magnified micrographs analyzed in ImageJ. Later, microfluidic devices were made by casting a 10:1 mixture of Polydimethylsiloxane (PDMS) prepolymer (Sylgard 184 kit, Dow Corning, USA) on the molds using a standard soft lithography process114 and bonding the layers onto glass slides using pre-exposure to oxygen plasma.

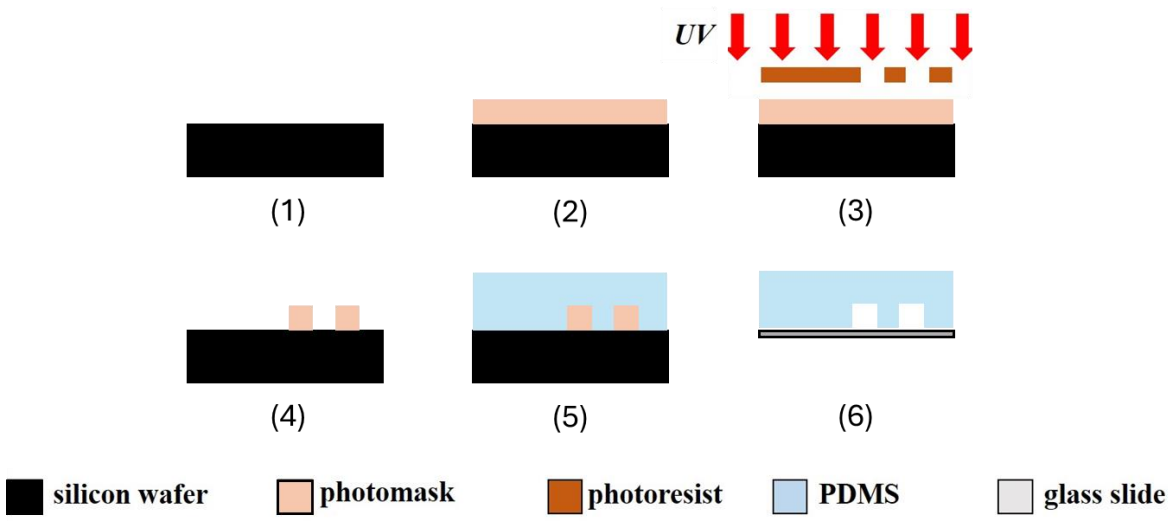

Figure 2-3 Photolithography and soft lithography steps for microfluidic device fabrication. Silicon substrates are initially cleaned (1), and then a layer of photoresist is spin coated (2), followed by a pre-exposure bake step. Then, the substrate is exposed to UV using a photomask to create the desired patterns (3). After a post exposure bake step, the photoresist is developed to prepare the final mold (4). Finally, a layer of PDMS is used to create the microchannels (5), which is peeled off the silicon mold and bonded to a glass slide using oxygen plasma (6).

Table 2-3 Microfabrication processing guideline with SU-8 2075 photoresist.

Channel Height (µm)	**SU8 Type**	**Spin Speed (rpm)**	**Pre-bake time (min)**		**Exposure Dose (mJ/cm^2)**	**Post exposure bake time (min)**		**Development Time(Sec)**
			at 65°C	**at 95°C**		**at 65°C**	**at 95°C**	
75	2075	2700	3	9	210	2	7	60
45	2025	2000	1	6	160	1	6	30
25	2025	3000	1	5	150	1	5	30

2.1.5 Experimental Setup

The experimental setup is shown in Figure 2-4. It consisted of a microfluidic enrichment device, a syringe pump (Legato 110, KD Scientific Inc., USA), a DMIL LED conventional inverted fluorescence microscope (Leica, Germany), FLIR Grasshopper3 USB3 Camera (GS3-U3-51S5M-C), and a personal computer to control and record Fluorescent Images of the particles in the expansion zone of the microfluidic enrichment device using the manufacturer's software (FlyCap2 Viewer, Teledyne FLIR Integrated Imaging Solutions Inc., USA.).

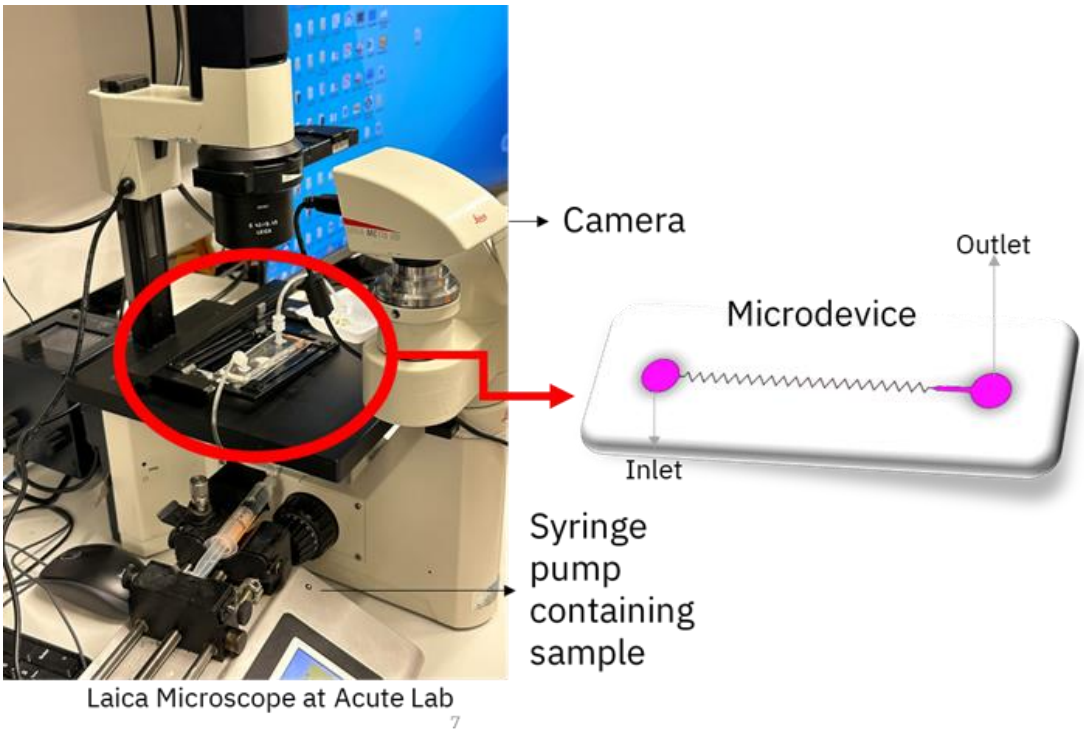

Figure 2-4 Experimental setup for microfluidic testing. The microdevice is placed on an inverted optical microscope (Leica DMi1) for real-time observation, with fluid introduced via a syringe pump for controlled flow. The schematic on the right highlights the microdevice channel geometry.

2.1.6 Device Operation

To observe particle behavior, nile-red fluorescent particles in PEO solutions of varying concentrations were introduced into the microchannel at flow rates between 2 and 25 µL/min,

resulting in average axial velocities from 0.029 to 0.21 m/s. These velocities were determined by dividing the volumetric flow rate by the square cross-sectional area of the microchannel. An example of the images obtained from the video recording through the microscope is presented in Figure 2-5.

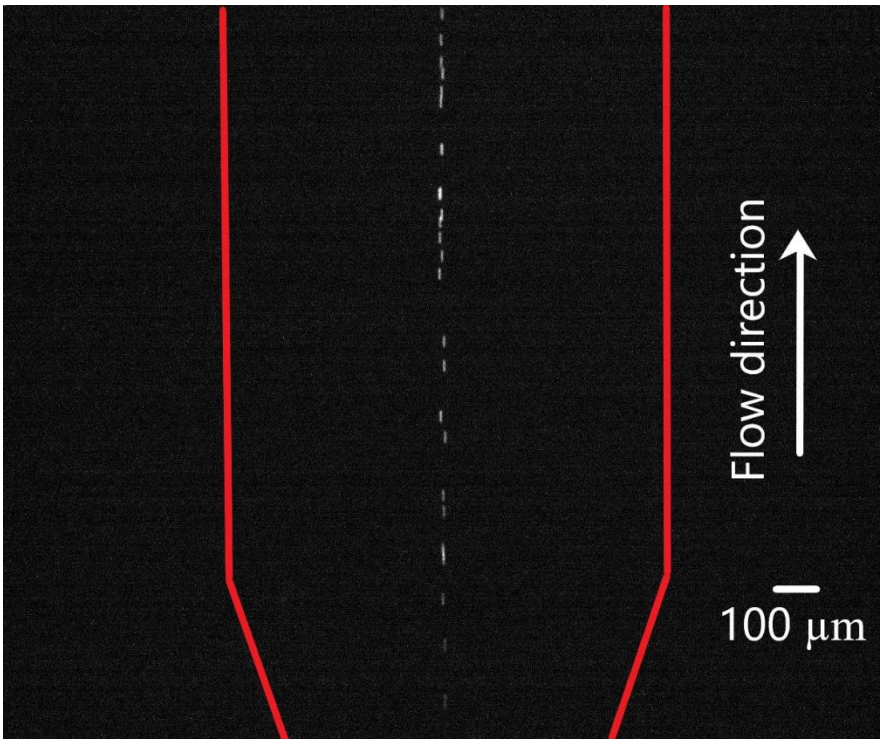

Figure 2-5 RoI within the straight microchannel where particle dynamics were monitored. The downstream expansion zone was designed to slow the local flow velocity, facilitating high-resolution imaging and accurate tracking of particle motion. Fluorescent particles appear as bright spots against a black background. The image corresponds to experimental conditions of a straight channel of 75 µm × 45 µm operated at 15 µL/min with 4 µm fluorescent particles suspended in a 1000 ppm PEO solution. Channel walls within the RoI are indicated by red lines.

Microparticle trajectories in the expansion zone were recorded using a FLIR Point-Grey camera mounted on an inverted microscope at 10x magnification, with a maximum frame rate of 151 fps. Each experiment was repeated three times. The video recordings were processed and analyzed using ImageJ[130], an open-source software, followed by further analysis with MATLAB.

2.1.7 Data Analysis

In ImageJ, the frames were cropped to remove any area outside the expansion zone as in Figure 2-6 leading to approximately 620 × 450 pixel frames. Since particles appeared multiple times based on their velocity within the expansion zone, every several frames were retained based on particles' axial velocity while the rest were discarded to ensure each particle was observed only once.

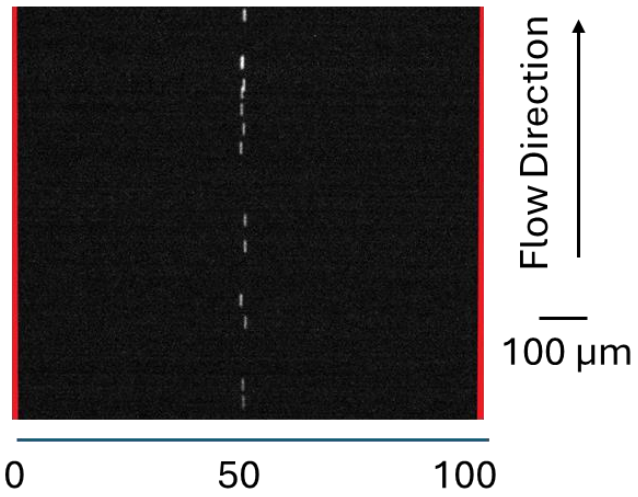

Figure 2-6 Cropped frame corresponding to the experimental conditions of straight channel with 15 µL/min flow rate of 4 µm fluorescent particles in 1000 ppm PEO solution, and a straight channel size of 75 µm × 45 µm. Channel walls in the RoI are designated with red lines and the channel width marked to from 0 to 100 parts.

Particle counting was performed using image stacks recorded from the expansion zone of the microchannel. Initially, the raw frames were processed in ImageJ to ensure that each particle was counted only once; this involved selectively keeping frames at specific intervals based on the particles' velocity within the expansion zone. Additionally, the frames were cropped to a size of 360×450 pixels, corresponding precisely to the channel expansion region. These preprocessed image stacks were subsequently analyzed using customized MATLAB code, which is reported in Appendix 149. The code was developed mainly by Sachin Satahoo and further refined to suit the

specific requirements of this analysis. In the MATLAB processing pipeline, as demonstrated in Figure 2-7, background subtraction was performed first, followed by applying a blur filter to reduce image noise. The processed images were then segmented by dividing the channel width into a defined number of sections, set to 100 sections in my analysis, as increasing the number of sections beyond this did not yield significant improvements.

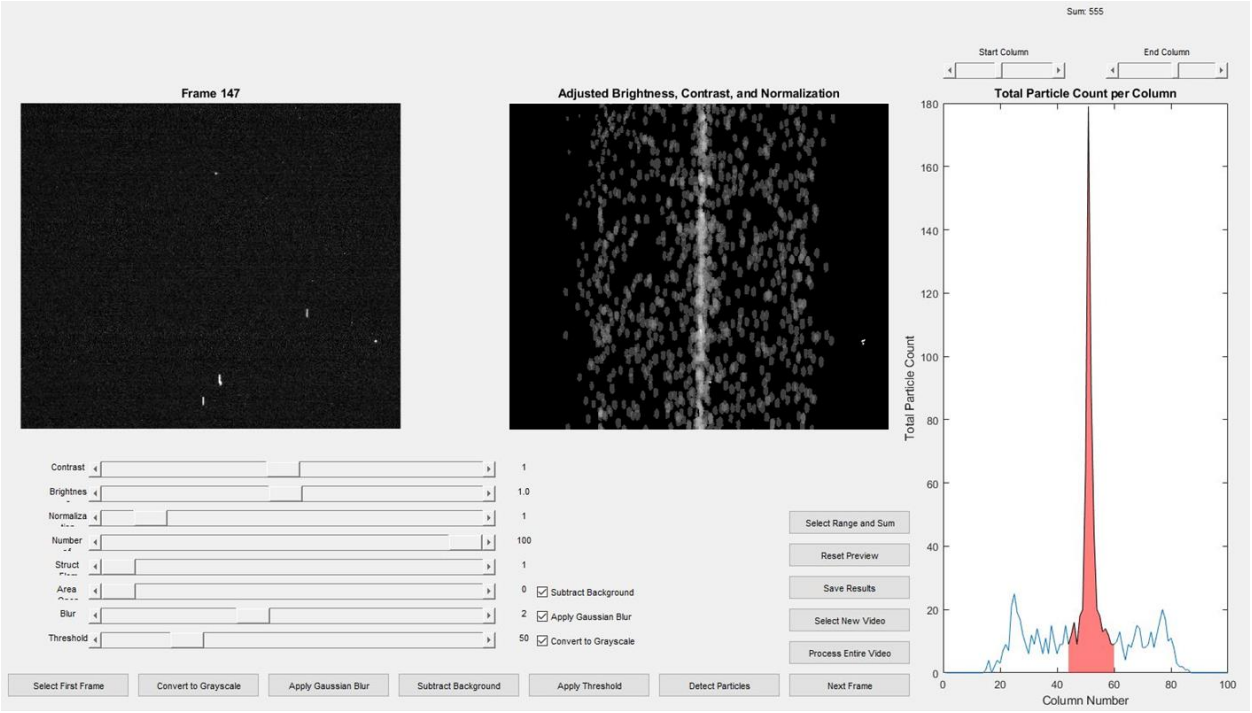

Figure 2-7 Custom particle tracking code for analyzing particle distribution across the channel width. The left panel shows a raw video frame, the middle panel displays an overlapped image after brightness, contrast, and normalization adjustments, and the right panel is the particle distribution graph along the channel width based on the number of divisions chosen in the settings.

The code proceeded to count the particles in each of these sections for every frame and exported the cumulative particle counts to an Excel file. To minimize counting errors, the MATLAB script included filters based on particle shape and size criteria. Additionally, the script generated binary image overlays, allowing intensity measurements on the composite image.

However, this particle-counting approach proved unsuitable for actual bacterial experiments due to the low intensity and smaller size of bacterial cells, making direct counting unreliable. Therefore, for bacterial experiments, the MATLAB code was adapted to analyze intensity distributions instead. By comparing the intensity distributions from experimental images with simulated distribution graphs, the optimal simulation conditions matching the bacterial focusing behavior were identified.

The parameters that are considered to study the data within are Re, El, and AR, as described in chapter 1. Another parameter is defined as Zf, which shows the geometrical complexity of the channel, which stands for straight, symmetric-zigzag, and asymmetric-zigzag channels with values of 0, 1, and 2, respectively. The focusing efficiency of particles was quantitatively assessed by studying the average fraction of particles passing through the central 10% width of the channel outlet from three repeats of experiments. As seen in Figure 2-8, based on these measurements, particle focusing performance was classified into five distinct categories: Group A (≥90%), Group B (70–90%), Group C (50–70%), Group D (30–50%), and Group E (<30%).

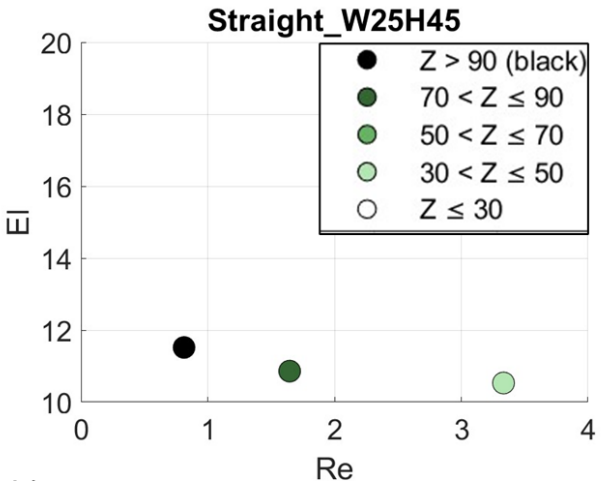

Figure 2-8 a) Quantitative classification of particle focusing performance in straight microchannels with dimensions of 25 μm × 45 μm. The focusing efficiency was evaluated as the fraction of particles passing

through the central 10% width of the channel outlet. Based on these measurements, focusing performance was categorized into five groups: Group A (≥ 90%), Group B (70–90%), Group C (50–70%), Group D (30–50%), and Group E (< 30%). Data points are color-coded accordingly, plotted as a function of Reynolds number (Re) and Elasticity number (El).

2.2 Photo-Thermal Readers for LFAs

2.2.1 Equipment and Materials

The thermal camera integrated into this system is a smartphone IR camera from Seek Thermal (Compact XR model). This camera is employed to capture infrared thermal images from out LFAs. As in Figure 2-9, the system also uses a ZnSe secondary lens (CO2 Laser lens, Shanghai, China) to form a microscope system zooming predominantly on the control and test lines of the LFA.

A crucial element of the laser system is its diode. The laser utilized in this device is an Infrared IR TO5-9mm diode from China, which has a maximum power of 1W and operates at a wavelength of 532 nm. The sample absorbs 0.565 watts. The diode is housed in a TO-5 Laser Diode LD Metal Housing, which features a focusable lens for improved laser light illumination.

The laser driver for the system is a Circuit Power Driver Board from China, compatible with 532 nm laser diodes. It allows for adjustable output current and power and includes a TTL port for modulation. A signal generator module board provides an electrical square wave signal at the desired frequency, serving as the excitation source in the device. An adjustable trigger relay module switches on the laser driver and disconnects it after a specified time. The relay used is a DC 12V Trigger Delay Time Switch from China. A stainless steel push button is used to control the system, starting operation with a single push. The system includes a power adapter and a power

socket for operation. LFAs specific to *E. coli* O157:H7 were purchased from Romer Labs company.

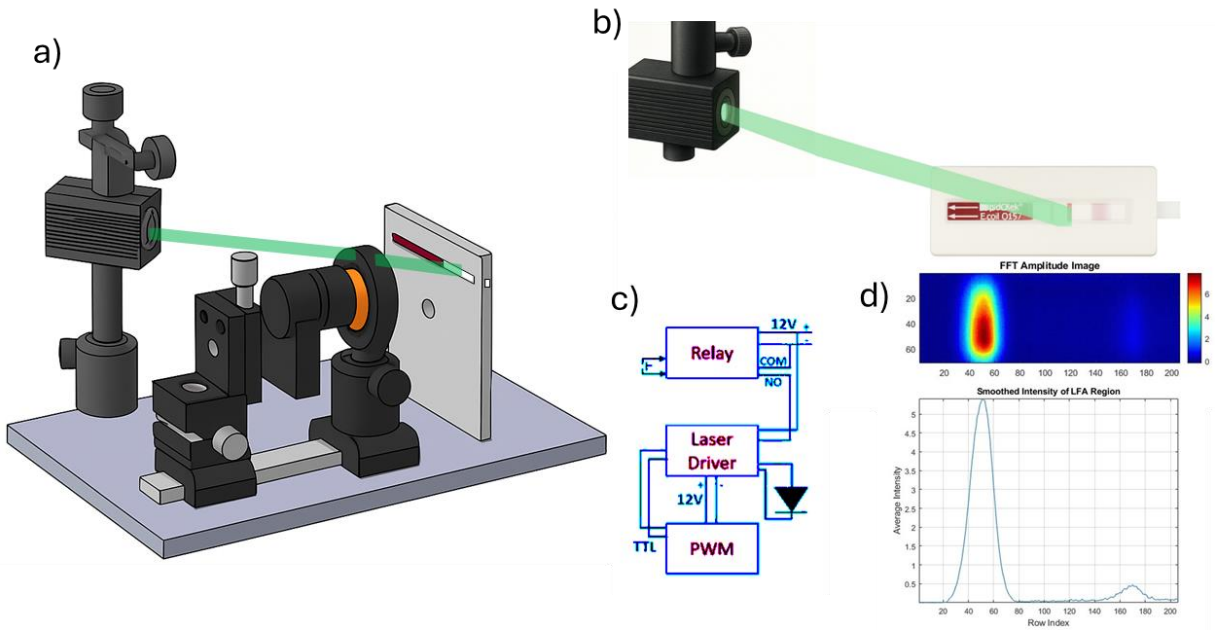

Figure 2-9 a) Exploded schematic of the developed portable TPLI device, illustrating its compact optical and mechanical components. b) Schematic representation of laser alignment toward the lateral-flow cassette. c) Simplified circuit diagram of the low-cost electronic control system integrating a pulse-width-modulated (PWM) laser driver and relay switch for laser modulation. d) Representative FFT-based amplitude map obtained from a cassette spiked with a 10^5 CFU/mL *E. coli*, alongside the corresponding smoothed intensity profile along the strip.

2.2.2 Biological Materials

To study LFAs with the photothermal reader, LFAs as in Figure 2-10 were prepared using *E. coli* O157:H7 bacteria in artificial urine (Sigma Aldrich, USA) containing 1000 ppm of polyethylene oxide (PEO). The bacteria (Sera Care, BacTrace *E. coli* O157: H7 Positive Control. No. 10174333) were supplied in powder form as heat-killed cells with a pre-determined concentration. First, 5000 ppm PEO was dissolved in water following the procedure described in

Section 2.1.1.1 for dissolving PEO in water. The artificial urine was then mixed with the PEO solution at a volumetric ratio of 4:1. This PEO–urine solution was subsequently spiked with the bacteria, and the resulting suspension was serially diluted to achieve concentrations ranging from 0 to 10^6 CFU/mL. For each test, 150 µL of the prepared bacterial solutions at the specified concentrations was applied onto the LFAs using a pipette, incubated for 5 minutes, and then left to dry overnight.

Figure 2-10 Commercial lateral flow assays (LFAs) specific for *E. coli* O157:H7, supplied in disposable test strips as sandwich style LFAs with a nominal LoD of 10^5 CFU/mL.

2.2.3 Device Design

The device was configured such that the LFA was positioned 5 cm from the camera, with the lens installed at 1 cm from the camera, as can be seen in Figure 2-11. A 532 nm wavelength laser, modulated at 1 Hz, was aligned to illuminate the center of the LFA, ensuring uniform excitation of both the control and test lines. The laser is placed 15 cm from the LFA strip at a 45° angle. The setup is depicted in the figure below.

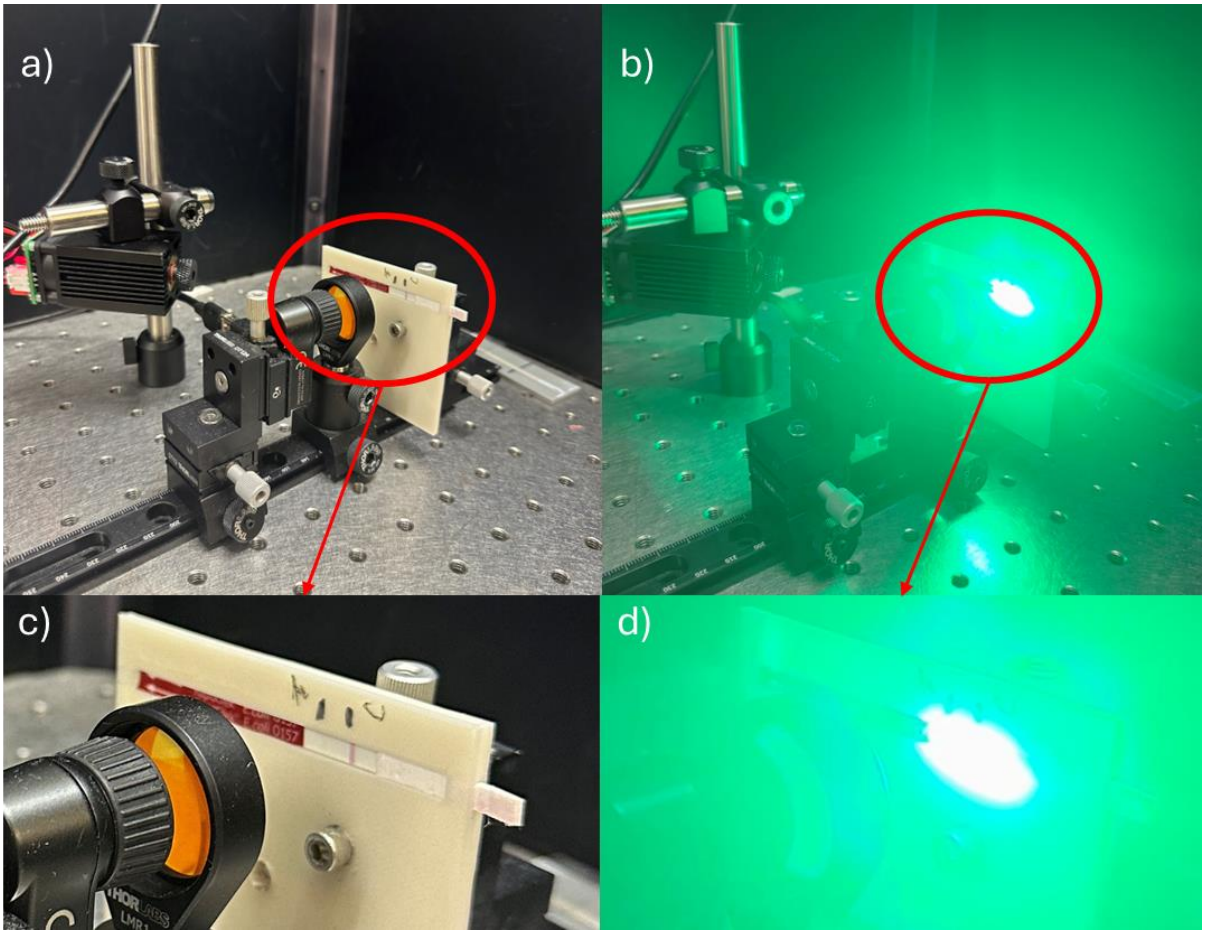

Figure 2-11 Photothermal LFA imaging setup. The LFA strip is positioned 5 cm from the camera, with the imaging lens mounted 1 cm from the camera. A 510 nm laser, 1 Hz intensity-modulated, is aligned to the center of the strip to uniformly excite the control and test lines. The photograph shows the camera, lens, and LFA mounts on an optical rail for precise alignment. Panel (a) shows the system with the laser turned off, and panel (b) shows the same setup with the 532 nm laser turned on and panels (c) and (d) are zoomed-in views of (a) and (b), respectively, highlighting the control and test line regions under ambient conditions (c) and under laser excitation (d).

The setup was powered by a 12 V supply and connected to a computer via a USB interface for data acquisition and control. The laser driver, signal generator, and relay were assembled in Figure 2-12.

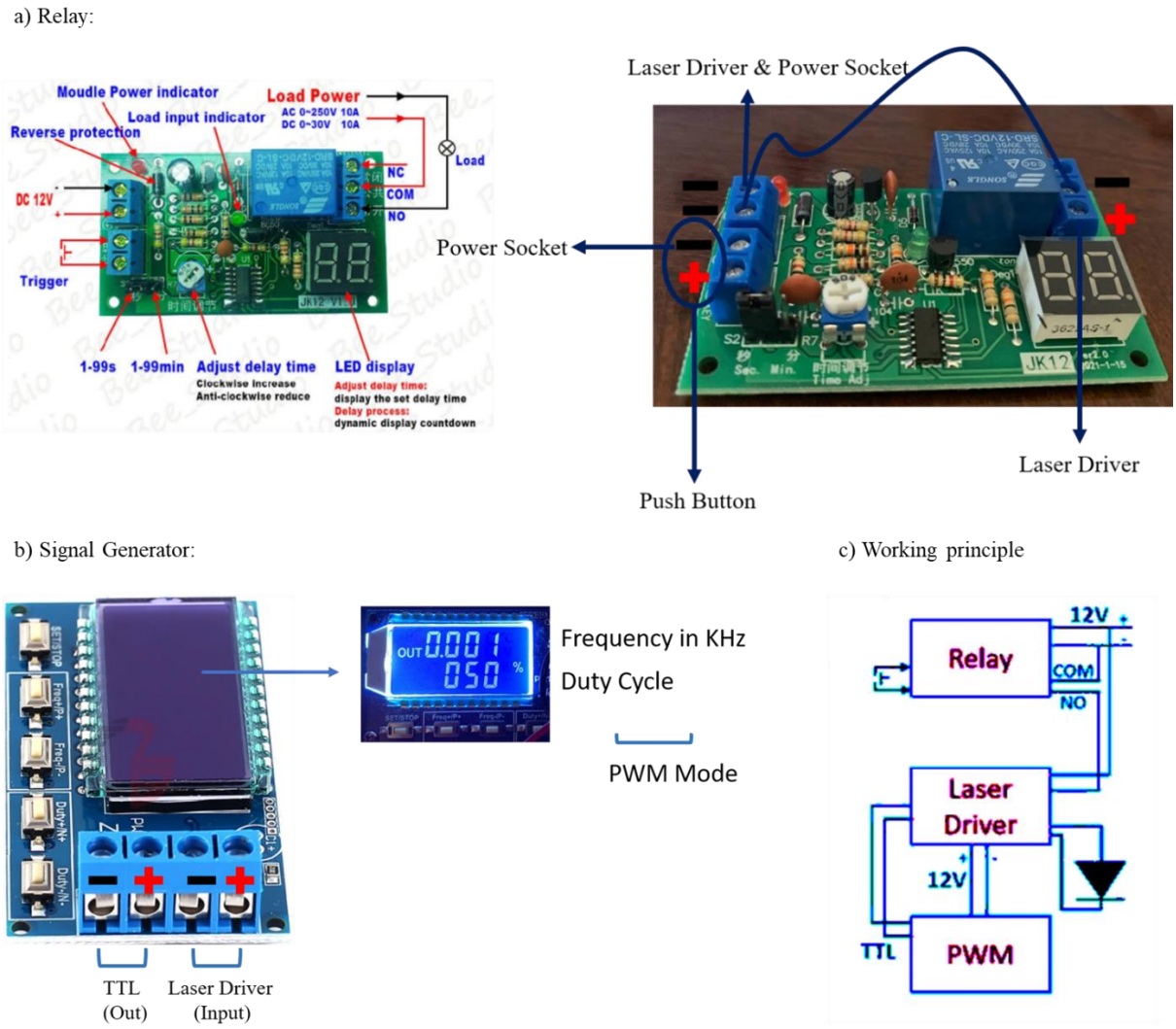

Figure 2-12 Power and timing electronics for laser modulation. A 12 V relay/timer module gates the laser driver under command from the signal generator and the USB-connected controller. Left:pinout showing DC power input, trigger, and relay load terminals (NO/NC/COM). Right: Assembled board with supply polarity and relay outputs annotated; the laser driver to switch the beam during 1 Hz operation.

2.2.4 Device operation

After placing the lateral flow assay (LFA) in its designated case within the photothermal reader, the measurement is initiated by pressing the activation button.

This triggers exposure of the LFA to modulated laser illumination. Concurrently, a custom-developed Python script is executed, initially incorporating a fixed delay period set to 20 seconds

to ensure stable conditions prior to data acquisition. Following this delay, an infrared camera begins recording for a duration of 50 seconds at a frame rate of approximately 9 Hz to yield a sequence of 520 frames. Each acquired frame and the corresponding timestamp are saved systematically into a text file for subsequent analysis.

2.2.5 Data Analysis

After acquiring frames, a fast Fourier transform (FFT) is applied to the time series waveform of each pixel, followed by determination of the magnitude and phase of the complex number corresponding to the laser modulation frequency in the Fourier domain. A detailed explanation of lock-in demodulation that describes the process of obtaining amplitude and phase images from the camera row frames can be found in previous papers[113,131].

Amplitude and phase images were acquired for each LFA with a camera capturing frequency of 9 Hz, and the raw signal data were extracted from the amplitude images. For instance, in Figure 2-13, three pixels from the control line, the test line, and the background are chosen, and the obtained signal over time is presented for each of them. Later, for each pixel by doing the FFT, an alternation from time to frequency domain is obtained, as in Figure 2-15b the modulation frequency (1 Hz) has the amplitude peak of the signal for every point, but the absolute value of the peak respectively from control line, to test line and the background (Figure 2-15c) , corelated to the amount of GNPs existing in each region.

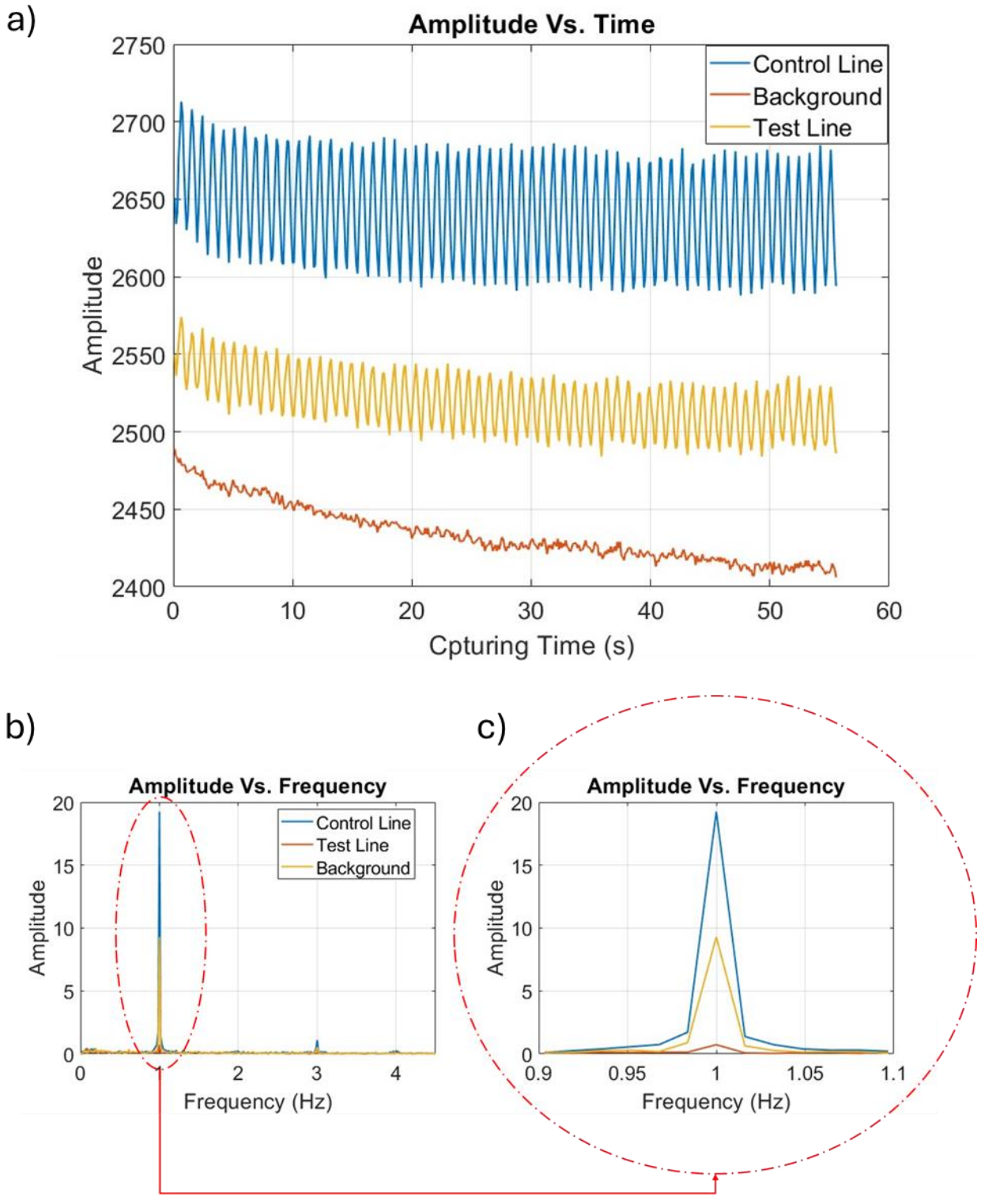

Figure 2-13 Representative lock-in signal extraction and frequency analysis from photothermal amplitude data. (a) Temporal amplitude variations of selected pixels from the control line (50, 80), test line (175, 80), and background regions (120, 80), recorded over a 60 s capture period. (b) Corresponding

frequency spectra obtained via Fast Fourier Transform (FFT) showing the 1 Hz modulation frequency peak for each region. (c) Magnified view of the amplitude peak near 1 Hz, where the relative magnitudes of the control, test, and background peaks.

Each amplitude image initially consisted of 156 rows by 206 columns of pixels. These amplitude images were subsequently cropped to a region measuring 156 rows by 60 columns, specifically corresponding to the locations of the control and test lines on the LFA strips. Histograms representing pixel intensity distributions of the cropped amplitude images were generated (Figure 2-14a). A notable peak in intensity between the test line and the control line was identified as background noise. This background intensity, calculated as the average pixel intensity between pixels 110 and 120, was subtracted from the entire dataset to minimize systematic noise effects.

To quantitatively compare the intensity values of the test and control lines, the maximum intensity peak from the histogram was identified and designated as the control line peak. The area under the intensity curve from M pixels before to M+25 pixels after this peak was integrated to represent the control line intensity. Subsequently, a second peak corresponding to the test line was located approximately 120 pixels following the control line peak. The intensity for this test line peak was similarly calculated by summing the area under the intensity graph from N pixels before to N pixels after the identified peak. The ratio of test line intensity to control line intensity was then computed to facilitate comparison across LFAs with varying bacterial concentrations. Throughout this manuscript, this calculated ratio will be referred to as the normalized amplitude value and will serve as the metric for calibration and quantitative evaluation of LFAs at different bacterial concentrations. Then the control to test line intensity ratios for each LFA are calculated and compared.

Each LFA strip was spiked three times at each bacterial concentration and subsequently tested three times, generating nine individual measurements per concentration. These nine data points were analyzed to determine their average intensity, minimum and maximum values, and the corresponding 90% confidence intervals. Based on these statistical measures, a calibrated comparison was performed across the concentration range to establish the LOD.

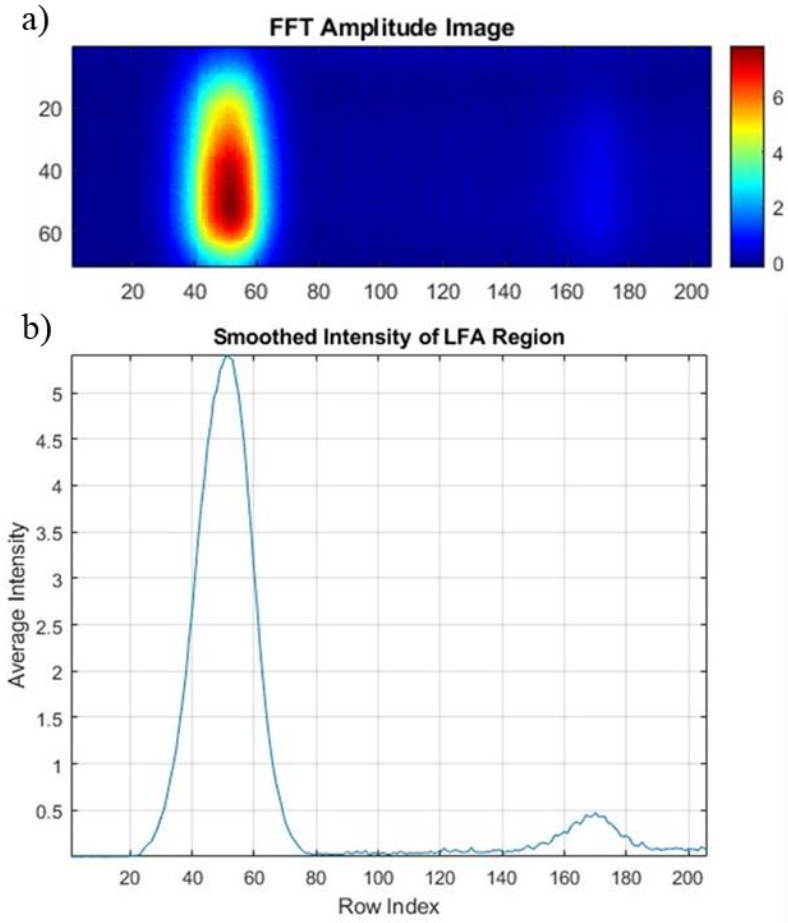

Figure 2-14 a) FFT-demodulated amplitude image and line-profile quantification. Top: representative amplitude image at the laser modulation frequency (size 156 × 206 pixel), cropped to a 156 × 60 pixel region spanning the control and test lines. Bottom: column-averaged, smoothed intensity profile versus row index, showing the control (left) and test (right) peaks. Background is defined as the mean intensity of pixels 110–120 (between the peaks) and subtracted from the entire image. Control and test line signals

are obtained by integrating fixed windows around their respective peaks; b) The T/C ratio of these areas is used as the normalized amplitude for calibration across bacterial concentrations.

2.3 Integration of Microfluidic Enrichment as Sample Prep with PT Detection of LFAs

To realize Objective 3, the microfluidic enrichment stage was directly coupled to the LFA and the photothermal reader to minimize transfer steps and sample loss. The enrichment process involved simultaneously running four parallel microfluidic devices for approximately 120 minutes to process the required sample volume of 100 µL for LFA testing. Following optimized viscoelastic focusing, the bacteria-rich effluent from the central outlet was collected and immediately dispensed onto the LFA sample pad according to the standard assay protocol. The PT readout, including image acquisition, normalization, and line-intensity quantification, was performed exactly as detailed in section 2.2. Each experiment was repeated three times, and the results are presented as the average efficiencies and purities ± the standard deviations (95%confidence).

Chapter 3

3 *E. coli* bacteria enrichment

3.1 Particle Enrichment and Focusing

At the early stages of the project, the flow behavior of real bacteria was still unknown, so 1 μm and 4 μm particles were selected to imitate single and aggregated *E. coli*, respectively and they served as controlled proxies to guide channel design. Rather than conducting a fully parametric study of the confinement ratio (β), it has been focused on designing channels that would meet β thresholds reported in the literature for effective particle focusing. For 4 μm particles, this resulted in channels with $\beta \approx 0.07$ and later $\beta = 0.053$. Fabrication and cost constraints limited β to 0.04 for 1 μm particles; further testing brought it down to about 0.03. All cases were first examined in DI water without PEO; however, as representative cases show in Figure 3-1, the particles exhibited

poor focusing and considerable dispersion under these conditions. To address this, subsequent experiments were carried out in the presence of PEO to identify the optimum concentration. Initial tests in straight channels were performed using 500 ppm and 1000 ppm PEO solutions. Higher concentrations were not pursued, as operation with 2000 ppm solutions proved impractical due to the substantial hydraulic resistance, particularly in smaller channels with dimensions of 25 × 25 μm^2. As demonstrated in Figure 3-1, both 500 ppm and 1000 ppm PEO solutions improved particle confinement and produced almost identical focusing profiles. Nevertheless, 1000 ppm was selected for subsequent studies, as the stronger elastic effects provided more robust and reproducible focusing, particularly for smaller particles such as bacteria, while remaining experimentally manageable.

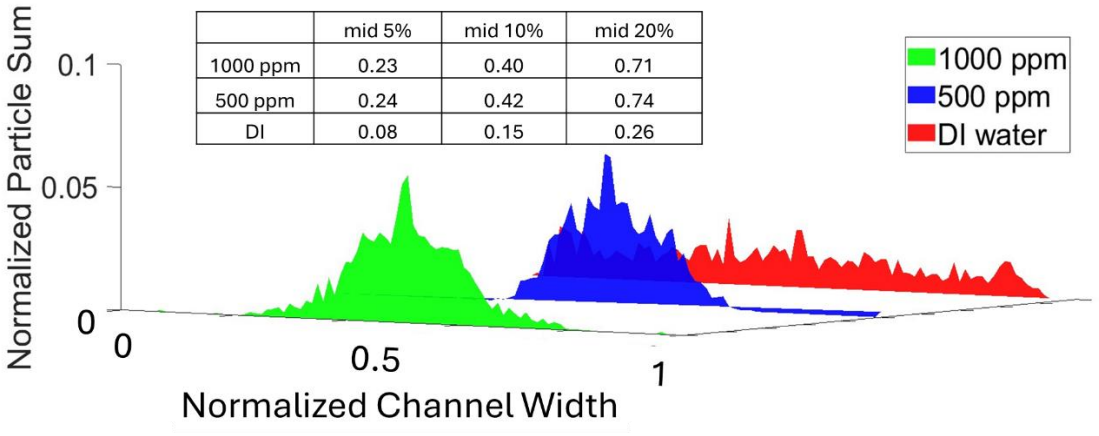

	mid 5%	mid 10%	mid 20%
1000 ppm	0.23	0.40	0.71
500 ppm	0.24	0.42	0.74
DI	0.08	0.15	0.26

Figure 3-1 Normalized particle distribution profiles across the channel width for 4 µm particles under three fluid conditions: 1000 ppm PEO (green), 500 ppm PEO (blue), and DI water (red), at a flow rate of 15 µL/min in a straight microchannel with dimensions of 75 µm × 75 µm. The corresponding enrichment values, defined as the fraction of the total particle signal captured in the central 5%, 10%, and 20% of the channel width, are summarized in the adjacent table. Both PEO cases exhibited significantly enhanced

particle focusing compared to DI water, with up to ~3times higher normalized particle sum in the mid 10% region.

3.1.1 Focusing Behavior Analysis of 1 µm Particles

The focusing behavior of 1 µm fluorescent particles was investigated across a matrix of channel geometries (Zf) like straight, symmetric zigzag, and asymmetric zigzag, and dimensions (AR), with a particular focus on variations with flow rates by Re and El numbers (section 1.2.2). Data are presented as demonstrated in Figure 2-8, Group A ($\geq 90\%$) represents excellent focusing, where nearly all particles are confined to a narrow stream suitable for single-line applications such as flow cytometry. Group B (70–90%) indicates strong focusing, where the majority of particles are recovered in the central outlet, making it acceptable for enrichment and sorting. Group C (50–70%) marks a transitional regime in which more than half the particles are centered, but the focusing stream is still forming. Group D (30–50%) corresponds to weak focusing, with only partial alignment and limited practical utility. Finally, Group E ($< 30\%$) denotes negligible focusing, where the particle distribution remains nearly random. These thresholds were selected based on their statistical significance and functional relevance to downstream microfluidic applications. These experiments reveal that both viscoelasticity and channel design critically influence particle focusing.

3.1.1.1 Effect of Re and El on Focusing Performance

To illustrate the combined influence of channel geometry and aspect ratio on viscoelastic focusing, Figure 3-2 maps the focusing performance of 1 µm particles as a function of Re and El across straight, symmetric zigzag, and asymmetric zigzag microchannels. Each row corresponds to a distinct channel dimension (25 µm × 45 µm, 25 µm × 25 µm, and 45 µm × 25 µm), enabling

direct comparison between geometries under similar conditions. The data points are color-coded according to focusing quality (Z) as in Figure 2-8.

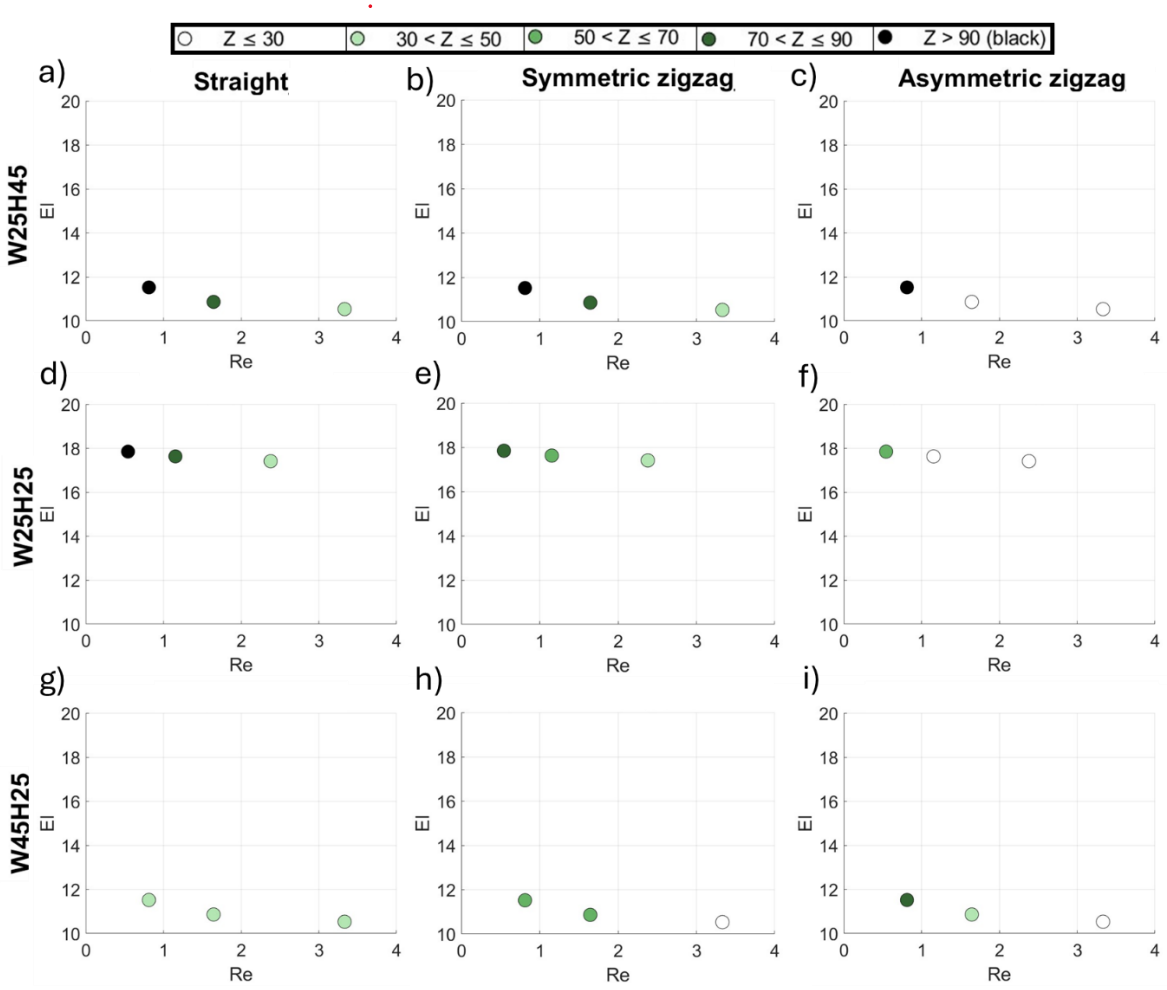

Figure 3-2 Focusing behavior of 1 μm particles as a function of Reynolds number (Re) and Elasticity number (El) across various microchannel designs (columns) and aspect ratios (rows). Each subplot represents a distinct combination of channel geometry (Straight, Zigzag, Asymmetric Zigzag) and dimensions (Width × Height in μm). Data points are categorized into five groups based on focusing quality: Group A (black for $Z > 90$), Group B (dark green for $70 < Z \leq 90$), Group C (medium green for $50 < Z \leq 70$), Group D (light green for $30 < Z \leq 50$), and Group E (white for $Z \leq 30$), with Group A indicating the highest and Group E the lowest focusing performance.

As seen in Figure 3-2, across all tested configurations, a general trend emerges: increasing Re tends to deteriorate focusing, while higher El improves particle alignment. For instance, in straight

channels with dimensions of 25 µm × 25 µm (Figure 3-2 panels d, e, f), the focusing performance transitions from Group A to Group C as Re increases from approximately 0.4 to 2.8 (~600% increase), and El decreases slightly, from 18.9 to 17.4 (~8% drop). A similar degradation is also observed in larger channels of 25 µm × 45 µm (Figure 3-2 panels a-c), and 45 µm × 25 µm (Figure 3-2 panels g-i), where focusing quality declines from Group A to Group D as Re increases from 0.6 to 3.4 and El drops from 13.1 to 11.3. However, these changes in El are relatively small, and the overall El range remains narrow. Compared to literature values that span from ~0.1 to 50 or more, this study probes only a moderate elasticity regime. Worth mentioning, higher flow rates serve us in terms of faster enriched sample collection, but the maximum feasible flowrate was 8 µL/min, leading to the studied El and Re range. These patterns confirm that inertial effects increasingly dominate at higher Re, whereas even moderately stronger elastic effects at higher El support stable focusing.

Although my channel geometry differs from the curved design with periodic contractions used by Lu et al. [132], the confinement ratio ($a/D_h \approx 0.03–0.04$) is comparable. Despite these geometric differences, both studies show a consistent trend Reynolds number increases transits 1 µm particles focusing from single-line (central) to two-line (sidewall). This shift reflects a force balance crossover, altering the equilibrium positions accordingly.

3.1.1.2 Effect of Zigzag Factor (Zf) on Focusing Performance

To further investigate the role of channel geometry in viscoelastic particle focusing, Figure 3-3 presents the relationship between Re and Zf for 1 µm particles across three different channel dimensions: 25 µm × 25 µm, 25 µm × 45 µm, and 45 µm × 25 µm. The Zigzag factor is a dimensionless parameter used to quantify the complexity of channel geometry, with Zf = 0 corresponding to straight channels, Zf =1 to symmetric zigzag channels, and Zf =2 to asymmetric

zigzag channels (one arm is twice as long as the other, although the total unit-cell length equals that of the symmetric design).

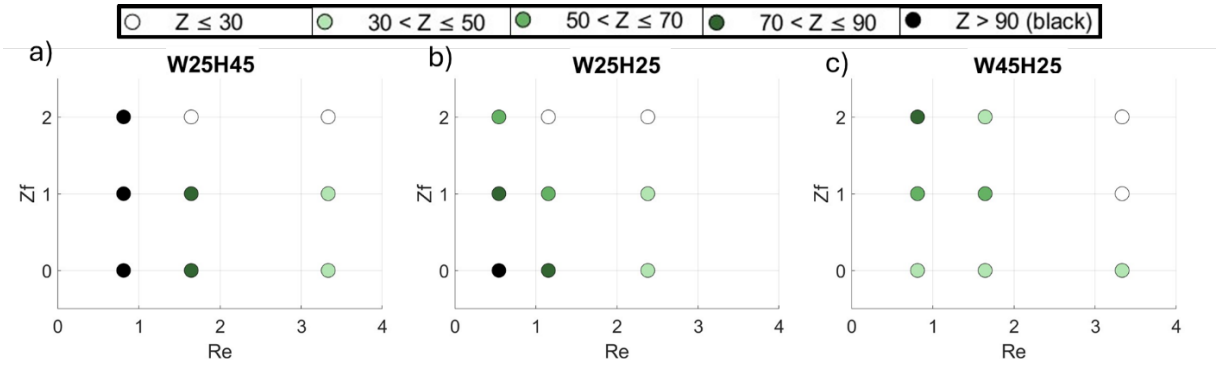

Figure 3-3 Focusing behavior of 1 μm particles across channels with varying geometries and aspect ratios, plotted as a function of Reynolds number (Re) and Zigzag factor (Zf). Zf represents the degree of channel complexity: Zf = 0 for straight channels, Zf = 1 for symmetric zigzag, and Zf = 2 for asymmetric zigzag geometries, defined by the ratio of actual channel length to its projected length. Each subplot corresponds to a unique channel dimension (W × H in μm^2): 25×25, 25×45, and 45×25. Data points are categorized by focusing performance: Group A (black for $Z > 90$), Group B (dark green for $70 < Z \leq 90$), Group C (medium green for $50 < Z \leq 70$), Group D (light green for $30 < Z \leq 50$), and Group E (white for $Z \leq 30$). The plots illustrate the deteriorating effect of increased channel complexity and Reynolds number on particle focusing, especially in higher aspect ratio channels.

For a given Reynolds number, fluid elasticity, and particle size, the instantaneous magnitudes of the three lateral forces of inertial lift (F_L), elastic lift (F_E), are identical in every geometry. In zigzag architectures the Dean drag force (F_D) was applied to the particles in each turn of the zigzag which did not exist in straight channels. Here, the amount of F_D is consistent for both symmetric zigzag and asymmetric zigzag channels; what differs is the duration of applying F_L and F_E after each bend. In Symmetric zigzag, there is identical F_L and F_E exposure time after each add and even bend, but in asymmetric zigzag, there is twice F_L and F_E exposure duration (zigzag arm length) after odd bends in comparison to even bends.

In the tall, narrow 25 µm × 45 µm channel (AR = 0.5), Figure 3-3 panel a, confinement is strong, and elastic lift greatly exceeds inertial lift. A straight channel, therefore, delivers a tightly focused core (Group A) at low Re. When symmetric curvature is introduced, each bend applies a brief Dean drag that pushes the band off centre, but the following straight reach is long enough for the dominant elastic lift to pull most particles back, so focusing falls only to Group B. In the asymmetric layout, the recovery distance after every even bend is shortened, leaving elastic lift insufficient time to complete the correction; a small offset persists from cell to cell and focusing degrades further to Groups C–D. Thus, raising Zf steadily worsens focusing when elastic lift dominates.

Also, in the square 25 µm × 25 µm channel (AR = 1), Figure 3-3 panel b, elastic lift greatly exceeds inertial lift as well but the aspect ratio leads to a slightly broader focusing line in comparison to the tall channels. The straight geometry yields moderate focusing (Groups B–C). Because the incoming stream is neither sharply aligned nor widely dispersed, the Dean drag of the symmetric zigzag perturbs and then largely re-centres the band within the equal straight sections, producing almost no net change. The asymmetric zigzag alters the timing of re-centring, but the balanced pair of lift forces still compensates over the longer opposite reach, keeping the data in Groups B–C. Channel geometry, therefore, has little influence when elastic and inertial lift are already in equilibrium.

In the wide, shallow 45 µm × 25 µm channel (AR = 2), Figure 3-3 panel c, weak confinement ends up with weaker particle focusing, so the straight channel enters the first bend with a dispersed cloud (Groups C–E). Here, even the modest Dean drag of a symmetric zigzag helps by sweeping some off-axis particles toward the centreline, partially offsetting the shortage of elastic lift and improving focusing by roughly one group. In the asymmetric zigzag, the unequal straight reaches

are still too short for weak elastic lift to undo this favourable displacement, allowing the gain to accumulate over successive cells and occasionally elevating performance to Group B. Increasing Zf therefore enhances focusing when elastic lift is weak.

In summary, the strengths of inertial lift, elastic lift, and Dean drag are fixed by the flow conditions; geometry merely changes the duration each force acts within a unit cell. When elastic lift dominates, additional Dean exposure is harmful because it repeatedly disturbs a well-focused core. When elastic and inertial lift are balanced, curvature has little net effect. When the elastic lift is weak, the same Dean exposure becomes beneficial by compensating for insufficient elastic migration. Hence, low aspect ratio devices should remain mostly straight, square channels can tolerate moderate corrugation without penalty, and high aspect ratio devices benefit from asymmetric zigzags that help recover focusing lost to limited elasticity.

3.1.1.3 Effect of Aspect Ratio (AR) on Focusing Performance

To evaluate how channel cross-sectional design impacts particle focusing, Figure 3-4 presents the relation between Re and AR, for 1 μm particles in three distinct geometries: straight, symmetric zigzag, and asymmetric zigzag.

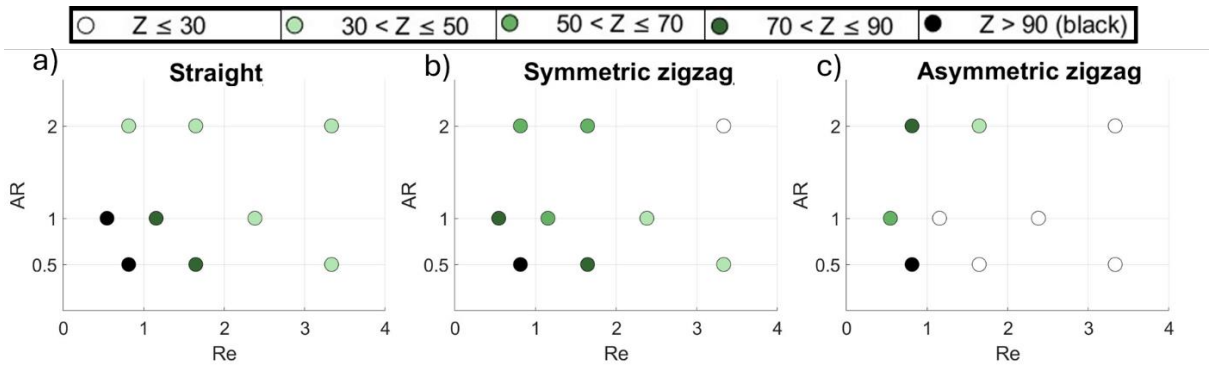

Figure 3-4 Focusing performance of 1 μm particles across channels of varying aspect ratios (AR = width/height) and geometries, plotted as a function of Reynolds number (Re). Each subplot represents a

distinct geometry: straight (left), symmetric zigzag (middle), and asymmetric zigzag (right). Data points are categorized by focusing quality: Group A (black for $Z > 90$), Group B (dark green for $70 < Z \leq 90$), Group C (medium green for $50 < Z \leq 70$), Group D (light green for $30 < Z \leq 50$), and Group E (white for $Z \leq 30$). The figure illustrates how increasing AR generally reduces focusing quality, particularly at higher Re and in geometries with greater complexity. Exceptions exist at moderate ARs ($AR \approx 1$) and Re ~ 1, especially in symmetric zigzag configurations.

Across all geometries, a consistent trend is observed: lower aspect ratios ($AR \approx 0.5$) are strongly associated with improved focusing, with data points falling into Group A or B, especially when Re is close to 1. Conversely, higher aspect ratios ($AR \approx 2$) tend to produce Group D or E results, indicating poor focusing regardless of geometry. This suggests that tall, narrow channels are more conducive to maintaining stable particle trajectories in viscoelastic flow regimes.

In straight channels, Figure 3-4 a, this trend is especially clear. At AR = 0.5 and $Re \approx 0.6–1$, particles fall into Group A, showing strong focusing. As AR increases to 1 and 2, and Re increases beyond ~1.5, focusing performance degrades toward Group E. Notably, no improvement is observed at AR = 1, indicating that any increase from AR = 0.5 significantly reduces alignment efficiency in straight channels.

Symmetric zigzag channels, Figure 3-4 b, however, exhibit a more nuanced pattern. While AR = 2 still corresponds to poor performance (Group D/E), the intermediate aspect ratio (AR = 1) performs better than expected: at $Re \approx 1$, particles fall into Group C, outperforming both lower and higher ARs in some cases. This suggests that symmetric zigzag geometries may introduce beneficial secondary flows or streamline compression that help maintain particle focusing under specific flow conditions.

In asymmetric zigzag channels, Figure 3-4 c, the negative impact of increasing AR is again prominent, with most high-AR points falling into Group E. However, an important exception

occurs at AR = 0.5 and Re ≈ 1, where the data point remains in Group A. This demonstrates that, despite the geometric complexity of asymmetric zigzag channels, maintaining a low aspect ratio can preserve strong focusing when Re is moderate.

Together, these observations reinforce the conclusion that low aspect ratios and Re ~ 1 provide the most favorable conditions for viscoelastic focusing. However, the deviation observed in symmetric zigzag channels at AR = 1 and the preserved performance in asymmetric channels at AR = 0.5 suggest that geometric effects can modulate focusing behavior in non-linear ways. These exception cases highlight that interactions between geometry, aspect ratio, and flow conditions can lead to localized enhancements or losses in alignment, which may be exploited in future channel designs for targeted applications. These observations are further supported by external studies. For instance, Tanriverdi et al. [133] demonstrated that increasing the channel height-to-width ratio (H/W), significantly improved focusing quality. Their experiments showed that decreasing AR restored single-stream focusing even at high throughput conditions (Re ≈ 85), indicating the broad applicability of vertical confinement in promoting elastic alignment.

Overall, minimizing channel aspect ratio (i.e., maximizing vertical confinement) is a reliable and geometry-independent strategy for promoting elastic-dominant, single-line particle focusing. This design principle remains effective across a range of channel geometries and operational Re values. This aligns with the elastic-dominant regime described by Suzuki et al. [88] in rectangular channels, where lateral migration is governed primarily by viscoelastic effects.

3.1.1.4 Conclusion of 1 μm particle focusing

The combined results from Figure 3-2 to Figure 3-4 show that optimal focusing of 1 μm particles occurs at moderate Reynolds numbers (Re ~ 1), high Elasticity numbers, low aspect ratios

(AR ≈ 0.5), and in straight channels (low zigzag factor). Increasing Re, AR, or channel complexity generally leads to poorer focusing performance. However, some exception cases were observed, such as strong focusing at Zf = 2 and Re ≈ 0.5, or at AR = 1 in symmetric zigzag channels, where elastic forces appeared to overcome the adverse effects of geometry or inertia. These findings highlight the importance of carefully balancing flow conditions and channel design to achieve efficient and robust viscoelastic focusing.

3.1.2 Focusing Behavior Analysis of 4 µm Particles

3.1.2.1 Effect of Re and El on Focusing Performance

The focusing performance of 4 µm particles under varying Re and Elasticity El numbers is shown in Figure 3-5 across three microchannel geometries (straight, symmetric zigzag, and asymmetric zigzag) and three channel dimensions. Compared to the 1 µm results, the range of El is lower (typically ~2.0 to 4.5), and particles operate at a relatively lower confinement ratio (β ~ 0.053 to 0.07), consistent with the inverse quadratic relationship between elasticity number and hydraulic diameter ($El \propto {D_h}^{-2}$).

The focusing behavior of 4 µm particles was examined across a variety of microchannel geometries and dimensions (75 µm ×75 µm, 75 µm × 45 µm, and 45 µm × 75 µm) under different flow rates of 5 ,10 ,25 µL/min characterized by Re and El numbers. Observations revealed that the 75 µm × 75 µm channel consistently exhibited poor particle focusing across all tested conditions. Despite having similar ratios of inertial lift and elastic forces corresponding to given Re and El numbers, absolute magnitudes of both inertial lift and elastic forces were found to be significantly lower in the 75 µm × 75 µm channel compared to the narrower channel configurations. Specifically, the elastic forces in the 75 µm × 75 µm channel were approximately one to two orders of magnitude lower compared to the 75 µm × 45 µm and 45 µm × 75 µm channels. Even though

inertial lift was also reduced, the combined effect of both forces was insufficient to achieve adequate focusing, as was evident from control experiments conducted in pure water where elastic forces were negligible, resulting in minimal particle focusing.

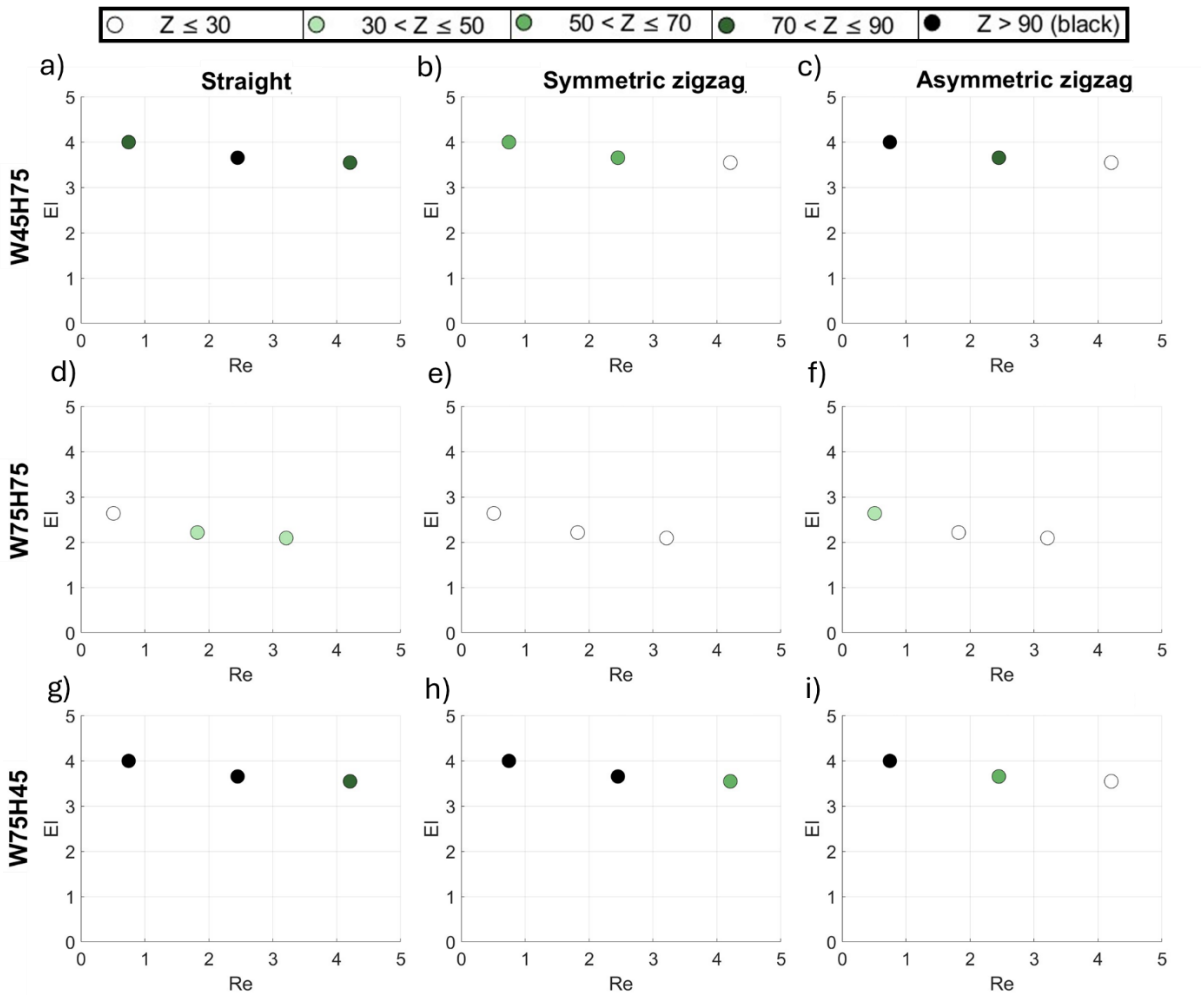

Figure 3-5 Focusing performance of 4 μm particles across varying Reynolds numbers (Re) and Elasticity numbers (El), plotted for different channel geometries and aspect ratios. Each subplot corresponds to a specific channel geometry (Straight, Zigzag, Asymmetric Zigzag) and dimension (Width × Height in μm^2). Data points are categorized into five groups based on observed focusing quality: Group A (black for $Z > 90$), Group B (dark green for $70 < Z \leq 90$), Group C (medium green for $50 < Z \leq 70$), Group D (light green for $30 < Z \leq 50$), and Group E (white for $Z \leq 30$). The plots show that moderate El and Re values generally result in better focusing, especially in straight channels and low aspect ratio geometries.

However, several exceptions are observed where good focusing occurs in more complex geometries under favorable flow conditions.

Increasing the Reynolds number generally resulted in a noticeable deterioration of focusing quality across all geometries. For example, as Re increases from ~1.0 to 3.5 (over 200% increase) and El decreases by 15–25%, the focusing classification shifts from Group A to Group D or E. This indicates that higher inertial forces suppress the elastic effects required for effective particle migration and alignment. Conversely, under conditions where El is relatively high (above ~4.0) and Re remains low (below ~1.5), particles consistently exhibit strong focusing, falling into Group A or B. These observations confirm that elasticity-dominated regimes are more favorable for achieving sharp focusing.

In summary, while the El–Re balance governs focusing performance in most cases, absolute channel size, and therefore β, must be considered alongside aspect ratio when comparing different particle sizes. These findings underscore the importance of jointly optimizing fluid properties and microchannel geometry. In particular, certain channel dimensions may limit the effective use of elastic forces, either by restricting transverse migration or by introducing geometric constraints that suppress elastic stress gradients, thereby compromising focusing efficiency.

The experiments with 4 μm particles in channels with blockage ratios of ≈0.053 and ≈0.071 fall within the same range as Liu et al. [134] for 5 μm particles. Although both systems operated at similar Reynolds numbers (Re ≈ 0.4–1.2), my setup exhibited lower elasticity and Wi numbers due to differences in polymer concentration and relaxation time, yet showed comparable focusing trends. Consistent with Lu et al. [132], larger particles maintained centerline focusing over a broader Re range, whereas smaller ones transitioned to sidewalls at lower Re. Furthermore, the AR = 1 configuration matched Charjoui et al. [81], confirming expected focusing behavior, while results

across other aspect ratios demonstrated enhanced performance not covered in their study, underscoring the novelty and broader scope of my experiments.

3.1.2.2 Effect of Zigzag Factor (Zf) on Focusing Performance

Figure 3-6 explores the impact of zigzag factor (Zf) and Reynolds number (Re) on the focusing behaviour of 4 µm particles across three different channel dimensions. The results indicate a clear overall trend: focusing quality degrades with increasing Zf and Re, particularly when both are high. Nonetheless, several low-Re exception cases show that good focusing is still achievable in complex geometries under appropriate flow conditions.

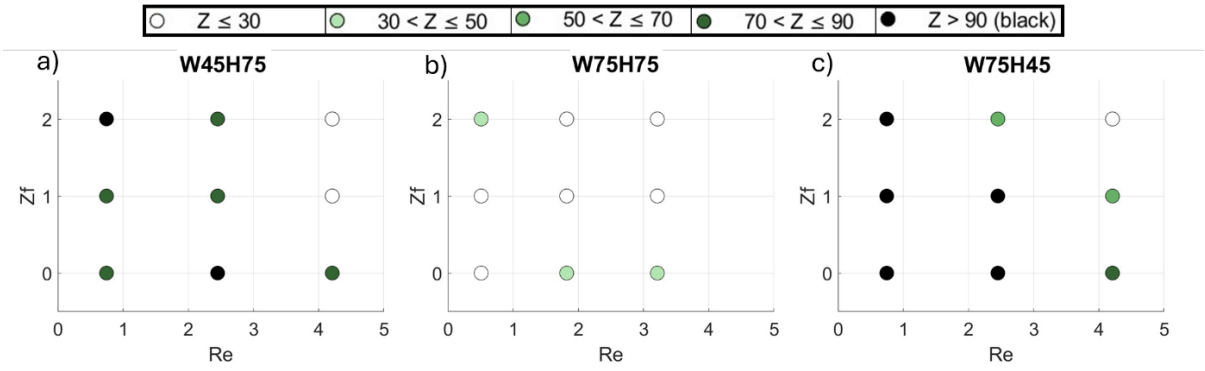

Figure 3-6 Focusing performance of 4 µm particles plotted as a function of Reynolds number (Re) and zigzag factor (Zf), where Zf = 0 represents straight channels, Zf = 1 symmetric zigzag channels, and Zf = 2 asymmetric zigzag channels, defined by the ratio of actual to projected channel length. Each subplot corresponds to a different channel geometry: 75 µm × 75 µm (left), 45 µm × 75 µm (middle), and 75 µm × 45 µm (right). Marker shapes represent focusing quality groups: Group A (black for $Z > 90$), Group B (dark green for $70 < Z \leq 90$), Group C (medium green for $50 < Z \leq 70$), Group D (light green for $30 < Z \leq 50$), and Group E (white for $Z \leq 30$). Overall, focusing degrades with increasing Re and Zf, although several low-Re data points show good focusing even in asymmetric channels, demonstrating the potential dominance of elastic effects in low-inertia regimes.

In the 45 µm × 75 µm channel, Figure 3-6 a, focusing performance is strongly dependent on Re. At Zf = 0 and Re ≈ 1, particles fall into Group B, indicating good alignment with an average

focusing efficiency of ~85 % (n = 3, SD ≈ 2 %), i.e., near the upper boundary of the 70–90 % "Group B" window. Introducing asymmetry (Zf = 2) at the same Re raises the mean focusing to ~93 % (SD ≈ 1 %), thereby crossing the 90 % threshold that defines Group A. The ~8 % absolute gain confirms that the shift from B to A is not a statistical artefact but a real, incremental improvement in confinement that exceeds the grouping criteria. As Re increases above 3, focusing drops to Group E, reinforcing that inertial effects dominate when elastic forces are not strong enough to maintain alignment.

The 75 µm × 45 µm, Figure 3-6 c, channel exhibits a more consistent pattern. At Zf = 0 and moderate Re (~1–2), focusing remains strong (Group A). However, with increasing Zf, especially at Re > 3, particles transition to Group D or E, confirming that both higher flow rates and greater geometric complexity negatively impact particle alignment.

In the 75 µm × 75 µm configuration (Figure 3-6 b), focusing outcomes are distributed primarily among Groups D and E across the full range of Reynolds numbers and geometries. Although Re increases from low to moderate values, no clear improvement in focusing is observed. The presence of zigzag features in this configuration does not significantly alter the group classification, suggesting that focusing is limited under these dimensional and flow conditions.

Overall, the results from Figure 3-6 highlight that while simpler geometries (low Zf) and moderate Reynolds numbers (Re ~ 1) are generally optimal for focusing 4 µm particles, the effect of channel design is not absolute. Under specific conditions, particularly at low Re and with adequate elasticity, even highly curved and asymmetric channels can still yield strong focusing. These findings reinforce the importance of tuning flow parameters in conjunction with geometry to achieve robust and efficient particle alignment in viscoelastic microfluidic systems.

Although my zigzag geometry is identical to that used in the rigid Z-RISE study [78], the flow physics are fundamentally different. In Newtonian water, the compliant PDMS walls suppress wall-induced lift, preventing inertial focusing below a confinement ratio of $\beta \approx 0.07$, consistent with the two-band sidewall focusing observed in Z-RISE. However, when a dilute PEO solution is introduced, the resulting elastic lift reinstates the net focusing force and redirects it inward. This yields a single-line stream along the channel centreline, consistent with the elasto-inertial focusing regime previously described by Yang et al. [135], particularly their Figure 1, where similar centerline focusing was achieved in straight PDMS channels under viscoelastic conditions.

3.1.2.3 Effect of Aspect Ratio (AR) on Focusing Performance

Figure 3-7 illustrates the combined influence of Reynolds number (Re) and channel aspect ratio (AR) on the focusing performance of 4 µm particles for three channel geometries: straight, symmetric zigzag, and asymmetric zigzag.

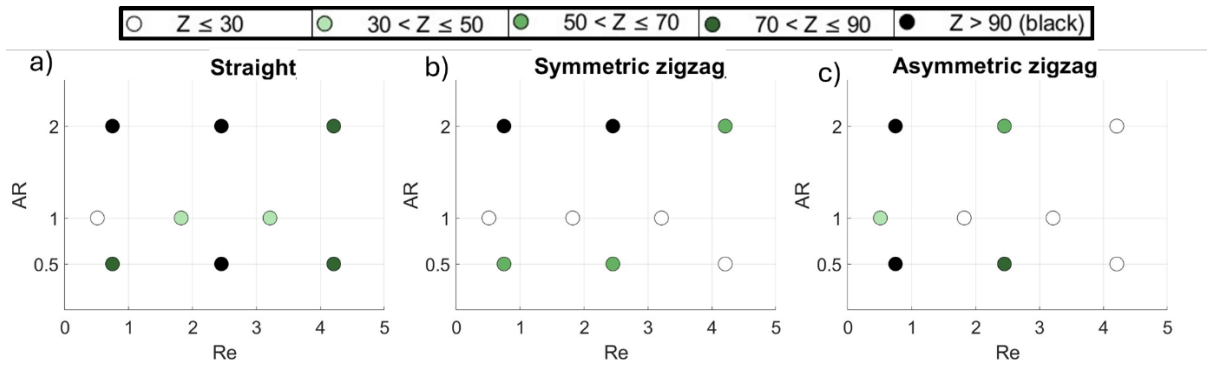

Figure 3-7 Focusing performance of 4 µm particles as a function of Reynolds number (Re) and aspect ratio (AR = width/height). The three subplots correspond to different channel geometries: straight (left), symmetric zigzag (middle), and asymmetric zigzag (right). Marker shapes represent focusing performance groups: Group A (black for $Z > 90$), Group B (dark green for $70 < Z \leq 90$), Group C (medium green for $50 < Z \leq 70$), Group D (light green for $30 < Z \leq 50$), and Group E (white for $Z \leq 30$). In general, lower AR (≈ 0.5) and moderate Re (≈ 1–2) are associated with better focusing performance,

while higher AR and Re lead to poorer focusing. A few exceptions suggest the existence of geometry-dependent optimal zones for elastic focusing.

A consistent pattern emerges across all geometries. Extreme aspect ratios (AR ≈ 0.5 or AR ≈ 2.0) generally support better focusing than intermediate values, particularly at moderate flow rates (Re ≤ 2.5). In contrast, square channels (AR ≈ 1.0) consistently underperform, regardless of flow conditions. This outcome likely reflects the distribution of shear gradients: at AR ≈ 0.5 or 2.0, shear is concentrated along one axis (vertical or horizontal), allowing elastic lift forces to act more effectively. In square channels, shear is more evenly divided between directions, weakening the net elastic migration and limiting focusing performance.

In straight channels, the most robust focusing is observed at AR = 2.0 and Re ≈ 2.4, where particles fall into Group A, indicating high alignment. Similarly, AR = 0.5 also produces strong focusing at low to moderate Re, while AR = 1.0 never achieves higher than Group C. As Re increases beyond ~3.5, performance deteriorates across all aspect ratios, although straight channels retain moderate focusing longer than curved geometries.

In symmetric zigzag channels, the impact of curvature becomes more pronounced. At AR = 2.0 and Re ≈ 0.9, Group A focusing is achieved, suggesting that curvature may assist in guiding particles toward the centerline under low flow rates. However, at higher Re or with AR ≈ 1.0, performance quickly declines to Groups D or E, highlighting that Dean-induced secondary flows can disrupt focusing if inertial effects dominate.

In asymmetric zigzag channels, the negative impact of curvature is more severe. At AR = 1.0, even at Re ≈ 1.5, particles exhibit poor alignment (Group D or E), and nearly all high-AR points fall into Group E at moderate to high flow rates. Only under gentle conditions, such as AR = 0.5

and Re ≈ 0.8, does strong focusing re-emerge (Group A). This underscores that both confinement and flow symmetry must be finely tuned for effective alignment in asymmetric channels.

In summary, the results from Figure 6 highlight the importance of cross-sectional confinement and flow regime in determining focusing performance. Low and high aspect ratios (AR ≈ 0.5 or 2.0) consistently support elastic focusing by creating dominant shear axes. Meanwhile, intermediate ARs (≈ 1.0) produce weaker gradients and diminished alignment. Curved geometries such as symmetric and asymmetric zigzags amplify these effects, often requiring stricter control over Re to preserve alignment. These findings confirm that optimal performance in viscoelastic microfluidic devices depends on the synergistic tuning of channel geometry and flow conditions, with straight channels offering the broadest operating window and asymmetric designs demanding the most careful balance. This behavior aligns with the elastic-dominant regime reported by Suzuki et al. [88] in rectangular microchannels, where lateral particle migration is primarily driven by viscoelastic forces.

3.2 Bacteria Enrichment based on Particle Experiment Outcomes

3.2.1 PEO Effect on *E. coli* Viability

An initial solution of LB containing *E.coli* was serially diluted with sterilized LB solutions containing 0, 1000, 4000 ppm of PEO. The *E. coli* dilutions for different PEO amounts were incubated for 2 hours. The effect of PEO on bacterial growth and viability was tested by plating matched dilutions on LB agar. Bacterial culture plates were incubated for 24 hours to enumerate CFUs. The triplicate counts were 42, 54, and 58 colonies for LB, 45, 52, and 42 colonies for 1000 ppm, and 50, 32, and 43 colonies for 4000 ppm. As in Figure 3-8, the corresponding means with

standard deviations were 51.3 ± 8.3 for LB, 46.3 ± 5.1 for 1000 ppm PEO, and 41.7 ± 9.1 for 4000 ppm PEO. A one-way analysis of variance across groups gave F with 2 and 6 degrees of freedom equal to 1.182 and a P value of 0.369. Pairwise comparisons relative to LB were not significant for 1000 ppm with P=0.426 and for 4000 ppm with P=0.246. These results show no statistically detectable effect of PEO at 1000 to 4000 ppm on *E. coli* viability under these conditions.

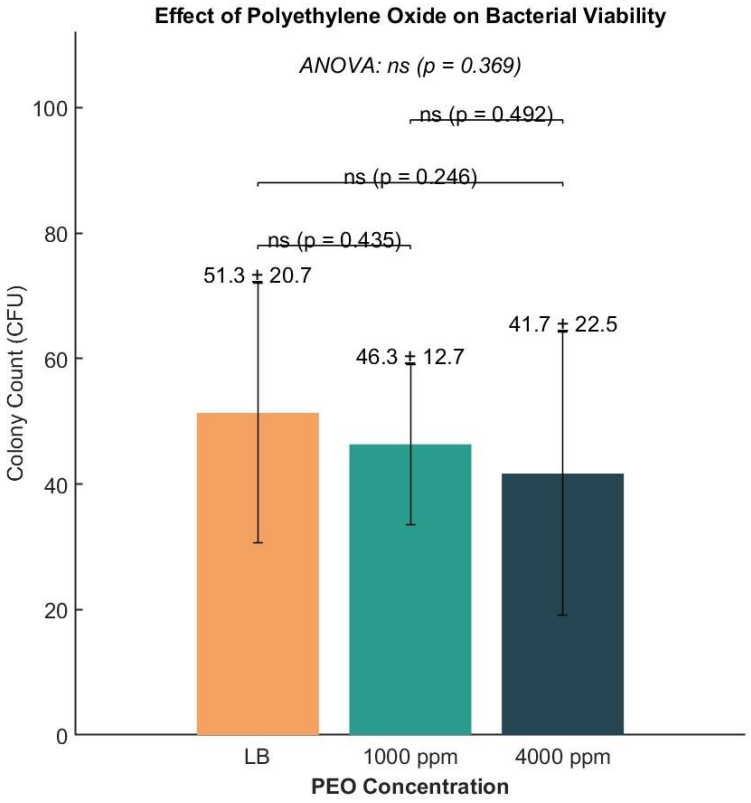

Figure 3-8 Colony-forming unit (CFU) counts for *E. coli* cultures exposed to 0, 1000, and 4000 ppm PEO. *E. coli* in LB was diluted into LB solutions containing 0 (control), 1000, or 4000 ppm PEO and incubated for 2 h. After plating and 24 h incubation on LB agar, CFUs were counted from triplicate plates: 51.3 ± 8.3 (LB), 46.3 ± 5.1 (1000 ppm), and 41.7 ± 9.1 (4000 ppm). One-way ANOVA showed no significant differences (p = 0.369); all pairwise comparisons were also non-significant (e.g., LB vs 4000 ppm: p = 0.246), indicating no measurable effect of PEO on bacterial viability.

3.2.2 Particle Size Comparison with *E. coli*

To identify a suitable surrogate particle for modeling bacterial migrations, optimal focusing conditions were first established for both 1 μm and 4 μm fluorescent particles in viscoelastic microchannels. For 1 μm beads, the highest focusing efficiency was achieved in straight microchannels with dimensions of 25 μm × 45 μm, operated at 2 μL/min. Under these conditions ($Re \approx 0.6$, $El \approx 13$), the mean capture efficiency reached 96.24 ± 1.16 %, indicating stable and tight focusing. For 4 μm particles, near-perfect focusing was observed in an asymmetric zigzag channel with 45 μm × 75 μm cross-section at 5 μL/min ($Re \approx 1$, $El \approx 4$), with focusing efficiency of 99.93 ± 0.06%.

To assess whether either particle size appropriately represented *E. coli* migration, GFP-expressing *E. coli* OP50 was introduced into the same microchannel configurations under matched flow conditions. Figure 3-9 compares 4 μm particles (panel a) and *E. coli* (panel b) in a 75 μm × 45 μm straight channel operated at 5 μL/min.

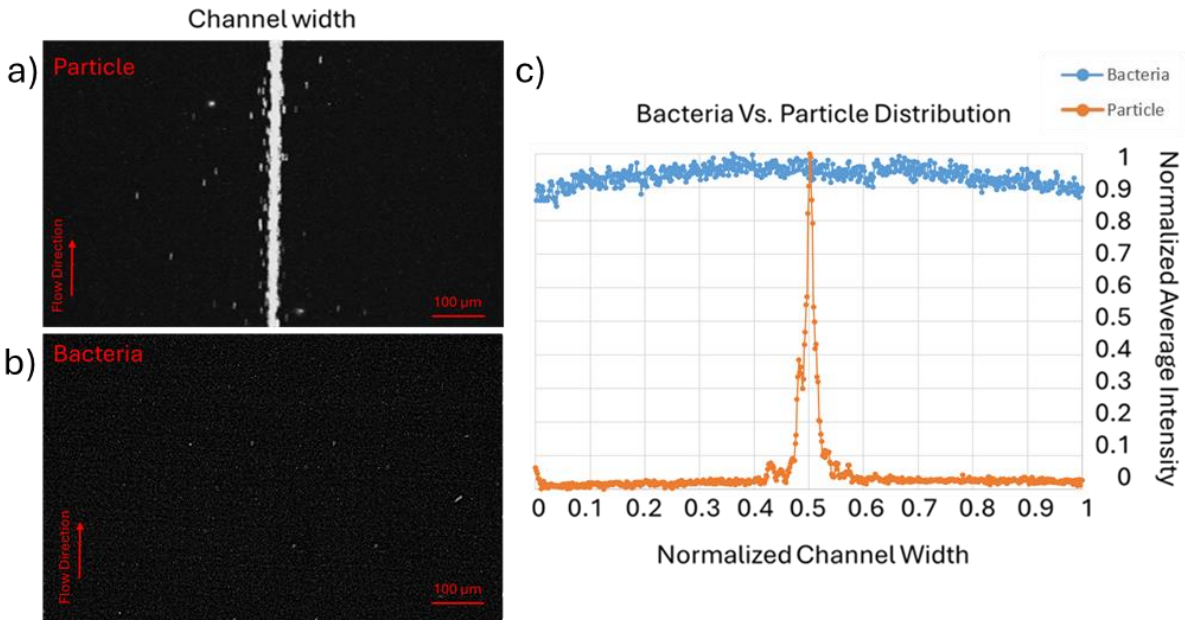

Figure 3-9 Comparison of focusing behavior between a) 4 µm fluorescent particles in 75 × 45 µm² straight channels under identical flow conditions (5 µL/min) and b) GFP-expressing *E. coli* OP50. c) The normalized intensity profiles reveal non-matching focusing patterns, suggesting 4 µm particles not to be a good representitive of *E. coli* bacteria.

The 4 µm particles formed a sharp central band, whereas the bacteria exhibited a broader, more dispersed distribution. This discrepancy is highlighted in panel (c), where normalized lateral intensity profiles reveal clearly non-overlapping patterns, suggesting that 4 µm particles fail to mimic bacterial transport behavior in these conditions. In contrast, Figure 3-10 shows the comparison between 1 µm particles and *E. coli* in 25 µm × 25 µm straight channels, both at 2 µL/min.

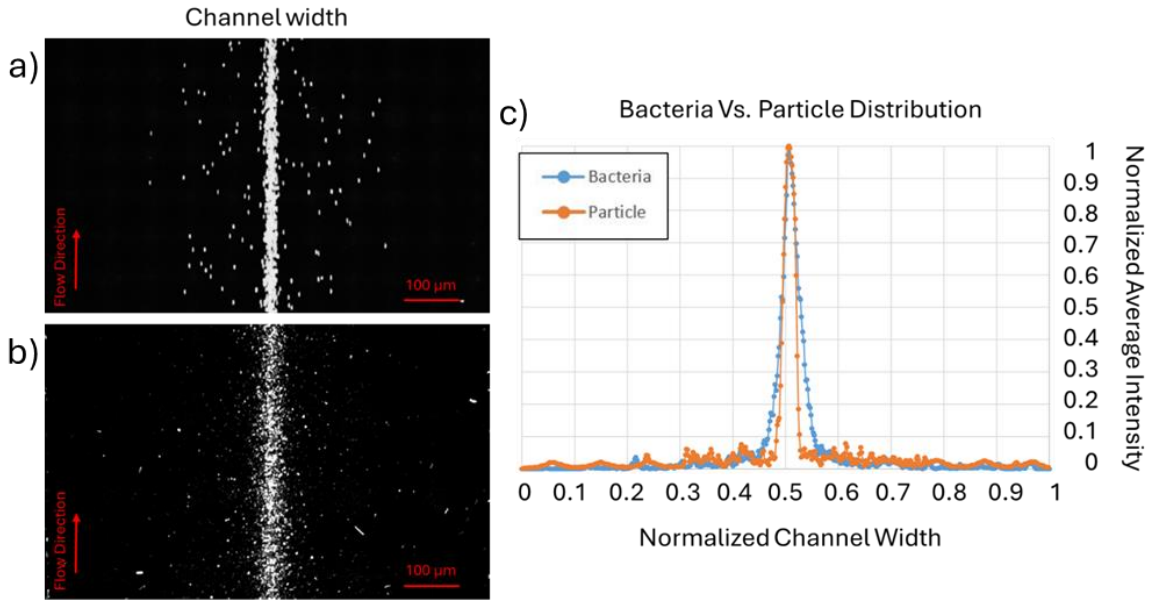

Figure 3-10 Comparison of focusing behavior between a) 1 µm fluorescent particles in 25 × 25 µm² straight channels under identical flow conditions (2 µL/min) and b) GFP-expressing *E. coli* OP50. c) The normalized intensity profiles reveal nearly identical lateral focusing patterns, justifying the use of 1 µm partoicles as a representitive for *E. coli* in enrichment experiments.

The fluorescence images (panels a and b) and corresponding normalized intensity profiles (panel c) demonstrate nearly identical focusing patterns between the particles and bacteria, with both exhibiting sharp central confinement and similar distribution widths. As observed, the 1 µm particles resembled more matching behaviour to the *E. coli* bacteria, therefore, the study proceeds with enrichment conditions optimized for 1 µm particle behavior.

Liu et al. [134] demonstrated centreline focusing of *E. coli* at Reynolds numbers between approximately 0.3 and 1. My experiments operated within a similar Re range (0.4–1.2) and under comparable AR conditions. The key difference lies in the elasticity of the working fluid, a denatured PEO solution with an elasticity number on the order of 100 was employed in that study, whereas my solution produced El values around 10. Despite this difference, both systems achieved

single-line focusing of 1 µm-scale particles. Notably, their study had also used 1 µm beads to mimic *E. coli* and observed similar focusing behaviour. This further supports that the 1 µm fluorescent beads used in my study serve as a reliable model for *E. coli* under comparable flow and confinement conditions.

3.2.3 Enrichment Channel Selection

The selection of microchannel geometries for *E.coli* enrichment followed a structured, stepwise approach based on preliminary particle-focusing results. The channels in which the highest enrichment percentages were observed, were selected for testing bacteria samples. Here, more details on the most optimized particle focusing conditions are presented. Each condition was replicated three times, yielding low standard errors of the mean (SEM = 0.47–1.16%), and statistical significance among the tested conditions was established using one-way ANOVA ($p = 0.0003$), with subsequent comparisons guided by Tukey's post-hoc analysis.

3.2.3.1 Straight channel, 25 µm × 25 µm at 2 µL/min

The initial geometry selected featured a square cross-section, chosen for its ease of fabrication and reliable particle confinement. This channel achieved a mean particle focusing efficiency of 90.24% (SEM = 1.09%), serving as the baseline reference for subsequent comparisons.

3.2.3.2 Straight channel, 25 µm × 45 µm at 2 µL/min

To investigate the effect of vertical confinement, the channel height was doubled while maintaining all other parameters constant. Particle focusing efficiency significantly improved to 96.24% (SEM = 1.16%), with Tukey's test confirming that this improvement was statistically significant compared to the baseline ($p = 0.0079$). Retaining this geometry thus provided a clear measure of the sensitivity enhancement achievable through relaxed confinement.

3.2.3.3 Zigzag channel, 25 µm × 45 µm at 4 µL/min

In this geometry, curvature was introduced along with a doubled flow rate, effectively reducing the residence time by half. Despite the increased throughput, particle focusing efficiency decreased slightly to 88.40% (SEM = 0.91%), although not significantly different from the baseline condition ($p = 0.6536$). This geometry was essential for assessing whether reduced processing times could justify the slight reduction in particle capture efficiency.

Two additional configurations were tested but ultimately excluded due to their limited value for comparative insights. The zigzag channel (25 µm × 45 µm at 2 µL/min) provided no measurable focusing advantage over its straight counterpart ($p = 0.9984$). Similarly, the asymmetric zigzag geometry resulted in significantly lower focusing performance without offering compensatory improvements in throughput, making it unsuitable for further consideration.

By strategically selecting geometries encompassing maximal particle focusing, baseline confinement conditions, and the highest practical throughput, the study effectively addresses critical trade-offs between particle capture efficiency, assay sensitivity, and processing time. This systematic approach ensures that incremental enhancements in particle enrichment directly translate to improved limits of detection and reduced total assay duration.

3.2.4 Enhanced Visual Detection of *E. coli* O157 in Lateral Flow Assays through Microfluidic Enrichment

Because the target *E. coli* strain O157:H7 was restricted from use in biosafety level-2 laboratories, a heat-killed stock sample with a known concentration of 4×10^9 CFU/mL was serially diluted to different concentrations and employed instead. The inactivated nature of the bacteria precluded culturing to experimentally verify enrichment performance. Furthermore, due to the low concentrations studied, hemocytometry was not considered a reliable method for

quantifying enrichment. Consequently, the visual LOD of the LFA was assessed as an indirect measure to determine whether microfluidic enrichment could enhance assay sensitivity by increasing the effective bacterial concentration prior to testing.

The visual LOD for LFAs was assessed before and after bacterial enrichment using microfluidics. As displayed in Figure 3-11, samples are spiked to the LFAs with and without enrichment. This is the representative data which shows the case of enrichment using 25 μm × 25 μm straight channels with 1000 ppm PEO and 2 μL/min flow rate.

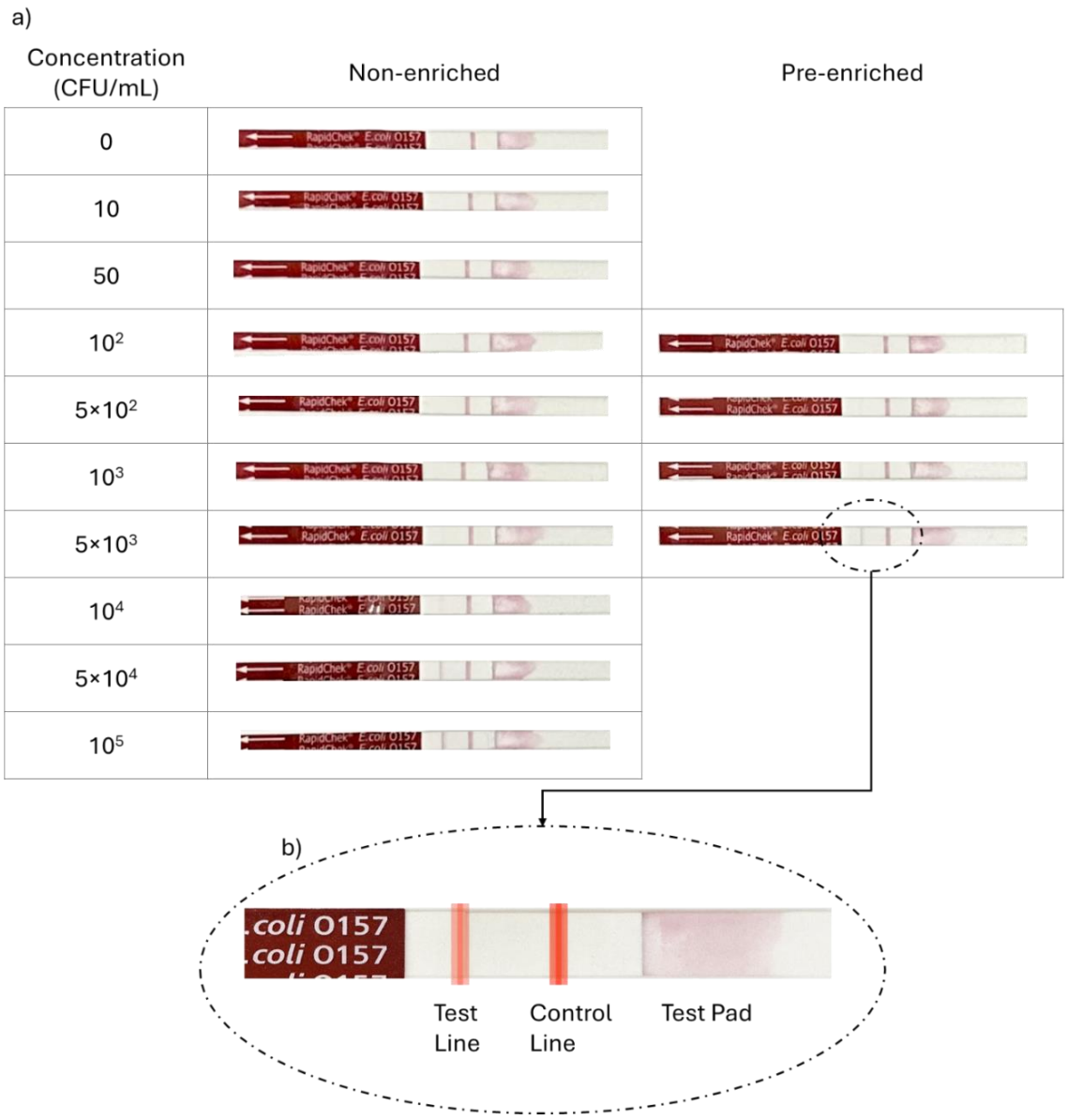

Figure 3-11 Comparison of visual detection sensitivity for *E. coli* O157 using standard (non-enriched) and microfluidically enriched samples. a) Non-enriched lateral flow assays (LFAs) (left column) exhibited a visual detection limit of approximately 50,000 CFU/mL (green arrow). In contrast, LFAs processed using microfluidic enrichment (25 µm × 25 µm straight channels, 1000 ppm PEO, 2 µL/min) demonstrated improved sensitivity, clearly detecting bacterial concentrations as low as 5,000 CFU/mL (green arrow, right column). Enrichment of 100 µL sample volumes was completed within 120 min using four parallel microfluidic devices. And b) A zoomed Image indicating the exact place of control and test lines in every LFA.

The non-enriched samples displayed no visible test lines for concentrations ranging from 0 to 10,000 CFU/mL. A clearly discernible pink test line appeared only at 50,000 CFU/mL, establishing the baseline visual LOD at 50,000 CFU/mL. As seen, enrichment has significantly improved the visual LOD. The enriched samples exhibited a clearly discernible test line at a lower concentration of 5,000 CFU/mL, whereas the test line at 1,000 CFU/mL remained undetectable.

Overall, microfluidic enrichment improved the visual detection sensitivity of the LFA by lowering the visual LOD from 50,000 to 5,000 CFU/mL. This represents a substantial improvement in assay sensitivity, aligning well with the measured enrichment performance.

Chapter 4

4 Design and Adjustment of Photothermal Reader for *E. coli* specific LFAs

LIPT was employed to quantify the thermal response of LFAs spiked with *E. coli* O157:H7 over a dynamic range spanning five orders of magnitude in bacterial concentration, both before and after viscoelastic microfluidic enrichment. Figure 4-1 presents representative amplitude maps acquired using a 532 nm laser modulated at 1 Hz, with a total acquisition time of approximately 60 seconds per strip. The colour scale (blue → yellow → red) represents increasing photothermal signal intensity corresponding to localized heat generation by the gold nanoparticle (AuNP)-labelled immunocomplexes formed along the test and control lines.

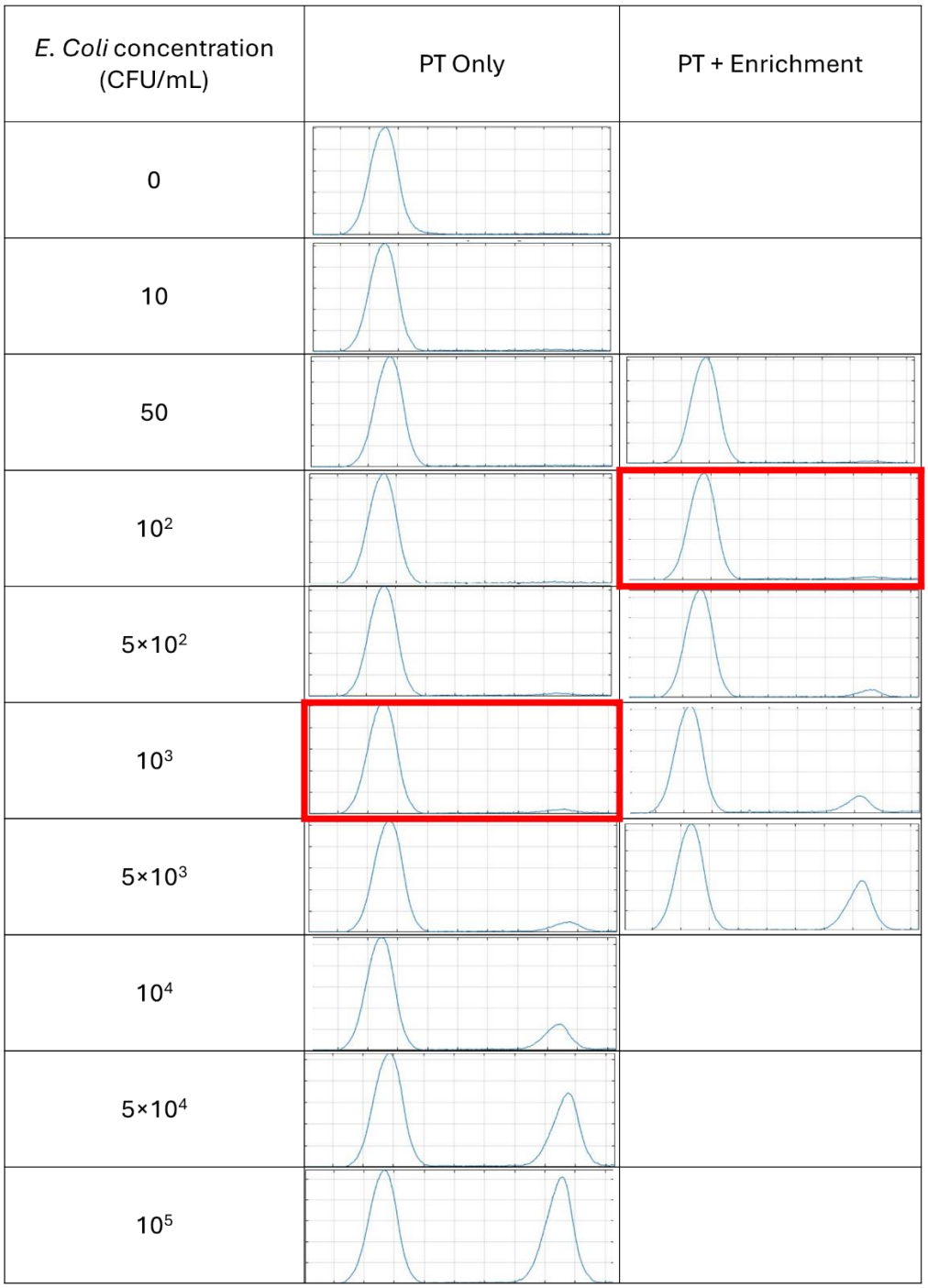

Figure 4-1 Photothermal amplitude maps of lateral flow test strips exposed to *E. coli* O157: H7 across five orders of magnitude, before and after viscoelastic microfluidic enrichment with straight 25 µm × 25 µm microchannel operated at 2 µL/min. Lock-in thermography amplitude images (colour

scale: blue→ yellow → red with increasing signal intensity) are shown for Photothermal study of LFAs with a 532 nm laser modulated at 1 Hz, with an acquisition time of ~60 seconds per strip.

As illustrated in Figure 4-1, PT imaging enabled the detection of *E. coli* concentrations as low as 10^3 CFU/mL in LFAs directly spiked with bacterial samples, without any prior microfluidic enrichment. This result highlights the superior sensitivity of PT-based readout compared to conventional visual inspection, as even faint test lines corresponding to low bacterial concentrations produced discernible thermal signals under modulated laser excitation.

Similar to section 3.2.4, the enrichment condition used for this representative case is also 25 μm × 25 μm straight channels with 1000 ppm PEO and 2 μL/min flow rate. The enriched samples exhibited a notably stronger photothermal response compared to non-enriched ones, reflecting the elevated concentration of captured AuNPs and, consequently, higher bacterial load. Under these conditions, the photothermal LOD for the enriched case was determined to be 100 CFU/mL. These findings confirm that coupling viscoelastic microfluidic enrichment with photothermal detection significantly enhances both the sensitivity and quantitative resolution of LFAs for *E. coli* O157:H7 detection, resulting in improved analytical performance.

It should be noted that this figure represents a single illustrative example demonstrating the potential of this PT method for low-level bacterial detection. In the subsequent section, a detailed statistical analysis is presented to systematically determine the LOD and limit of quantification (LOQ) across multiple replicate measurements, providing a quantitative assessment of the assay's performance and reproducibility.

4.1 Statistical Studies for LOD and LOQ

In this study, LOD was defined as the lowest bacterial concentration whose 95 % confidence interval (CI) no longer overlapped with those of any lower-concentration points on the same curve. Where the next concentration continued the upward trend with a similarly narrow CI, that second point was taken as the limit of quantification (LOQ).

Figure 4-2 compares the normalized test-to-control (T/C) line intensity ratios of LFAs for samples processed through the microfluidic enrichment system and those tested directly without enrichment. All enrichment experiments were conducted using a 1000 ppm PEO solution in a straight microchannel with dimensions of 25 μm × 25 μm, operated at a flow rate of 2 μL/min. Each data point represents the mean of nine measurements, derived from three independent enrichment experiments, each tested three times photothermally. Error bars denote the standard error of the mean across all measurements.

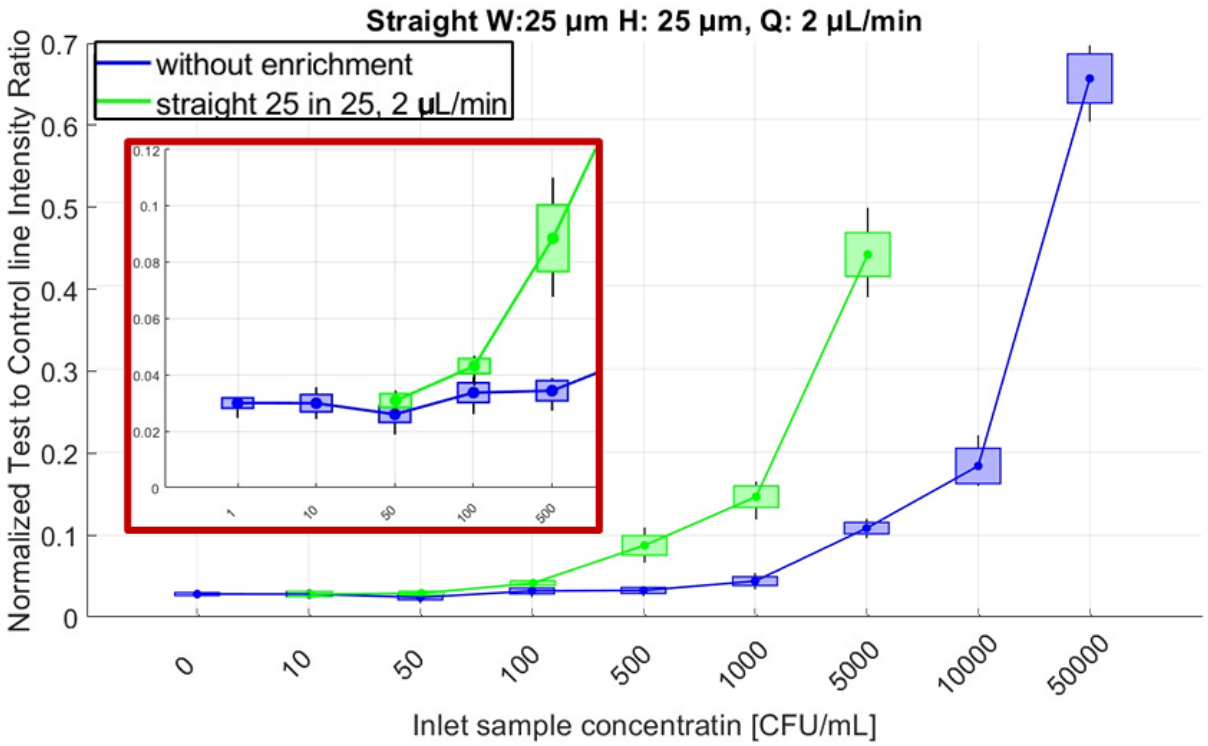

Figure 4-2 Normalized test-to-control line intensity ratios are plotted as a function of inlet sample concentration (CFU/mL), comparing enriched samples (green curve) against assays without enrichment (blue curve). All enrichment conditions were tested using 1000 ppm PEO, and error bars represent the standard error of the mean (n = 5). Straight channel, 25 µm × 25 µm, flow rate = 2 µL/min (green). This baseline geometry, characterized by strong confinement, showed improved detection at concentrations above 500 CFU/mL, confirming effective particle focusing.

The first non-overlapping confidence interval appears at 100 CFU/mL, establishing the limit of detection (LOD = 1×10^2 CFU/mL), while 5×10^2 CFU/mL marks the limit of quantification (LOQ). Amplitude images corresponding to these conditions are shown in Figure 4-1. Also, pairwise comparisons of the mean normalized amplitude values for *E. coli* O157:H7 LFAs of non-enriched samples is presented in Table 4-1. The table reports two-tailed *p*-values with significance levels (*ns* = not significant; *** = $p < 0.001$*).

Table 4-1 Welch's unequal-variance t-test results for photothermal signal amplitudes across bacterial concentrations for non-enriched samples

	1	**10**	**50**	**100**	**500**	**1000**	**5000**
1	-	0.9636 (ns)	0.01727 (*)	0.05138 (ns)	0.0284 (*)	7.672e-05 (***)	7.978e-10 (***)
10	0.9636 (ns)	-	0.04715 (*)	0.08142 (ns)	0.04701 (*)	5.215e-05 (***)	5.535e-11 (***)
50	0.01727 (*)	0.04715 (*)	-	0.001284 (**)	0.000761 (***)	5.556e-06 (***)	5.186e-11 (***)
100	0.05138 (ns)	0.08142 (ns)	0.001284 (**)	-	0.7612 (ns)	0.000699 7 (***)	3.967e-11 (***)
500	0.0284 (*)	0.04701 (*)	0.0007614 (***)	0.7612 (ns)	-	0.001178 (**)	3.51e-11 (***)
1000	7.672e-05 (***)	5.215e-05 (***)	5.556e-06 (***)	0.000699 7 (***)	0.001178 (**)	-	3.366e-11 (***)
5000	7.978e-10 (***)	5.535e-11 (***)	5.186e-11 (***)	3.967e-11 (***)	3.51e-11 (***)	3.366e-11 (***)	-

For the baseline without enrichment (blue curve), overlap persists through 500 CFU/mL; the CI at 1000 CFU/mL is the first to separate, as could be seen, giving an LOD of 10^3 CFU/mL. The signal then rises again at 5×10^3 CFU/mL, which therefore defines the LOQ for the control.

In the straight 25 µm × 25 µm microchannel operated at 2 µL/min with 1000 ppm PEO (green curve in Figure 4-2), with statistical data as in Table 4-2, the first non-overlapping CI already

appears at 100 CFU/mL, establishing an LOD of 1×10^2 CFU/mL. The point at 5×10^2 CFU/mL continues the monotonic rise with a tight CI, so 5×10^2 CFU/mL is taken as the LOQ for this configuration. Also, amplitude images related to the photothermal detection of non-enriched and pre-enriched samples with a straight 25 µm × 25 µm microchannel operated at 2 µL/min were presented in Figure 4-1 as well.

Table 4-2 Welch's unequal-variance t-test results for photothermal signal amplitudes across bacterial concentrations for samples enriched in the straight 25 µm × 25 µm microchannel operated at 2 µL/min

	1	**10**	**50**	**100**	**500**
1	-	0.9808 (ns)	0.5085 (ns)	2.042e-07 (***)	2.358e-06 (***)
10	0.9808 (ns)	-	0.5979 (ns)	1.918e-06 (***)	1.39e-06 (***)
50	0.5085 (ns)	0.5979 (ns)	-	7.98e-07 (***)	2.168e-06 (***)
100	2.042e-07 (***)	1.918e-06 (***)	7.98e-07 (***)	-	1.361e-05 (***)
500	2.358e-06 (***)	1.39e-06 (***)	2.168e-06 (***)	1.361e-05 (***)	-

Similarly, Figure 4-3 compares the normalized T/C lines intensity ratios of LFAs for samples processed through the straight 25 µm × 45 µm microchannels operated at a flow rate of 2 µL/min with 1000 ppm PEO. Each data point represents the mean of nine measurements obtained from three independent enrichment experiments, each analyzed photothermally in triplicate as in the

previous case. Error bars indicate the standard error of the mean across all measurements. And Figure 4-3 summarizes the results of Welch's unequal-variance *t*-tests comparing the mean normalized amplitude values for *E. coli* O157:H7 LFAs under this enriched condition.

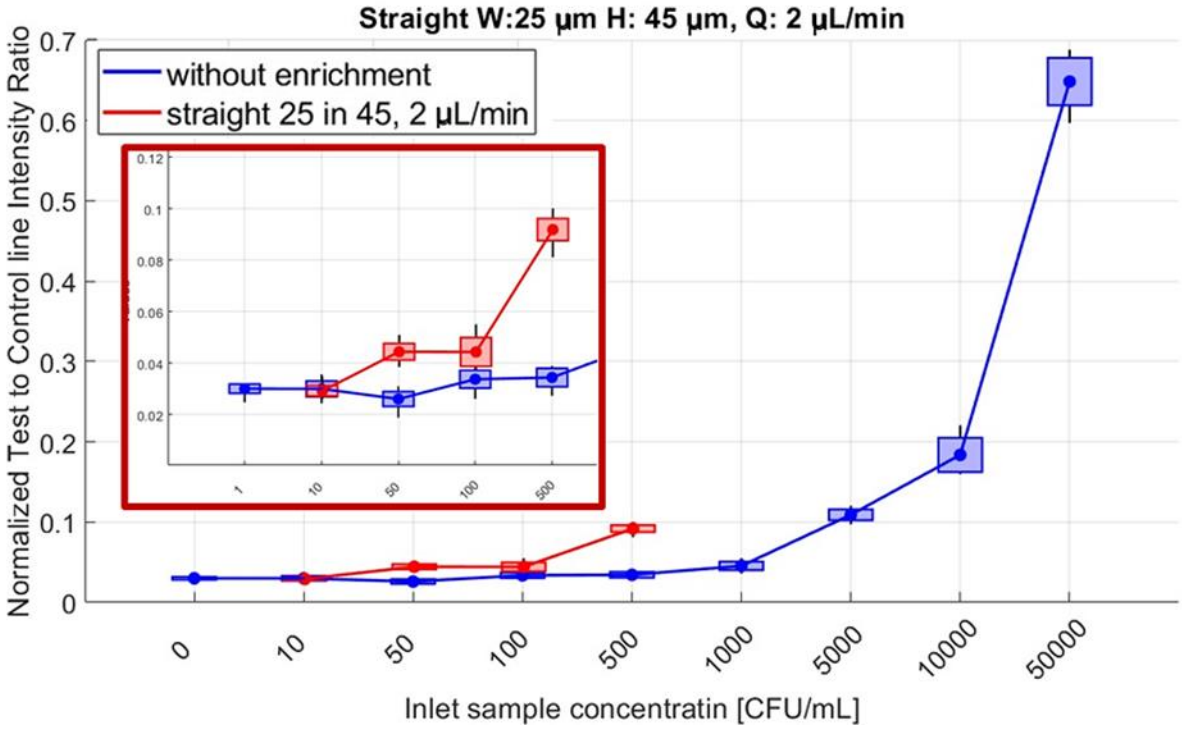

Figure 4-3 Normalized test-to-control line intensity ratios are plotted as a function of inlet sample concentration (CFU/mL), comparing enriched samples (red curve) against assays without enrichment (blue curve). All enrichment conditions were tested using 1000 ppm PEO, and error bars represent the standard error of the mean (n = 5). Straight channel, width = 25 µm, height = 45 µm, flow rate = 2 µL/min. Increasing channel height (relaxed confinement) led to further improvement in signal intensity, especially at intermediate concentrations, highlighting the role of vertical geometry in enhancing enrichment.

Table 4-3 Welch's unequal-variance t-test results for photothermal signal amplitudes across bacterial concentrations for samples enriched in the straight 25 µm × 45 µm microchannel operated at 2 µL/min

	1	**10**	**50**	**100**	**500**
1	-	0.4844 (ns)	8.517e-07 (***)	0.0002584 (***)	8.74e-12 (***)
10	0.4844 (ns)	-	3.748e-07 (***)	0.0001562 (***)	3.253e-12 (***)
50	8.517e-07 (***)	3.748e-07 (***)	-	0.978 (ns)	3.022e-12 (***)
100	0.0002584 (***)	0.0001562 (***)	0.978 (ns)	-	1.153e-10 (***)
500	8.74e-12 (***)	3.253e-12 (***)	3.022e-12 (***)	1.153e-10 (***)	-

For the straight 25 µm × 45 µm channel at the same flow rate (red curve), overlap remains up to 100 CFU/mL, but the CI at 500 CFU/mL is clearly distinct, yielding an LOD of 5×10^2 CFU/mL. No higher-concentration point is available, so the LOQ cannot be assigned.

And finally, Figure 4-4 compares the normalized T/C line intensity ratios of LFAs for samples processed through symmetric zigzag microchannels with dimensions of 25 µm × 45 µm, operated at a flow rate of 4 µL/min using a 1000 ppm PEO solution. Each data point represents the mean of nine measurements obtained from three independent enrichment experiments, each analyzed photothermally in triplicate, consistent with the previous case. Error bars denote the standard error of the mean across all measurements. Table 4-4 presents the results of Welch's unequal-variance

t-tests comparing the mean normalized amplitude values for *E. coli* O157:H7 LFAs under this enriched condition.

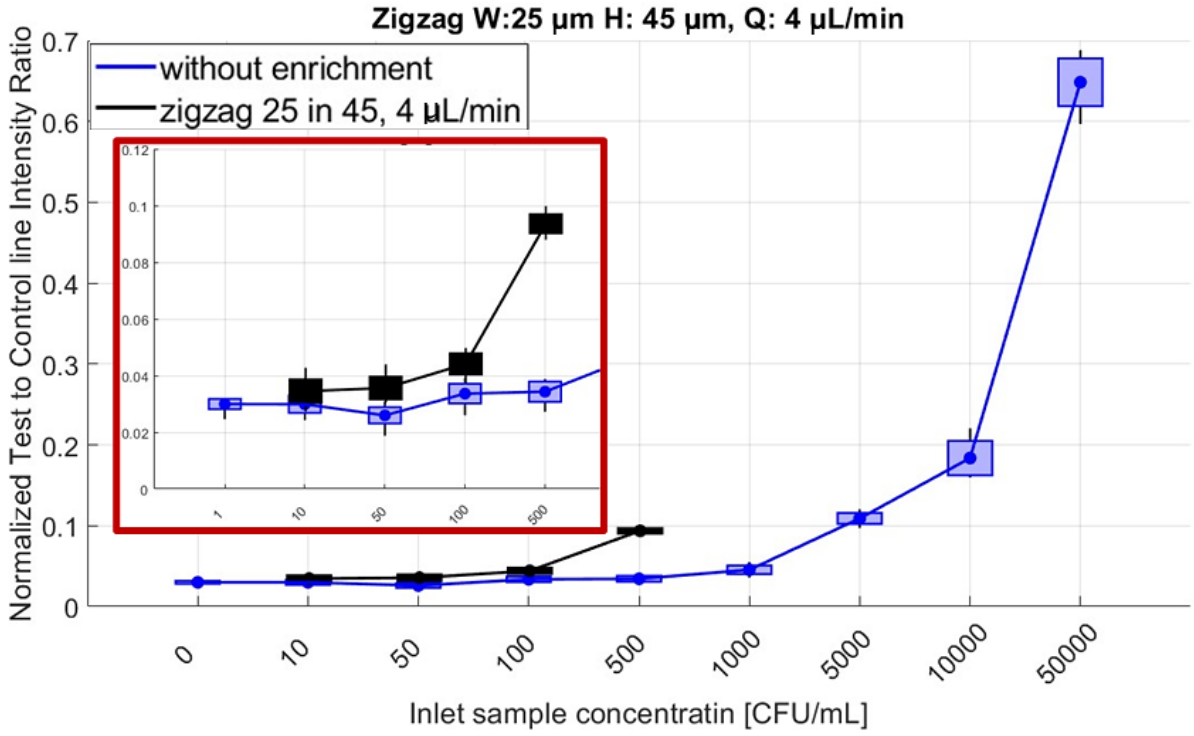

Figure 4-4 Normalized test-to-control line intensity ratios are plotted as a function of inlet sample concentration (CFU/mL), comparing enriched samples (black curve) against assays without enrichment (blue curve). All enrichment conditions were tested using 1000 ppm PEO, and error bars represent the standard error of the mean (n = 5). Zigzag channel, width = 25 µm, height = 45 µm, flow rate = 4 µL/min. Introducing curvature and doubling the flow rate (reduced residence time) resulted in only modest gains at lower concentrations, emphasizing the trade-off between throughput and focusing efficiency.

Table 4-4 Welch's unequal-variance t-test results for photothermal signal amplitudes across bacterial concentrations for samples enriched in the symmetric zigzag 25 µm × 45 µm microchannel operated at 4 µL/min

	1	**10**	**50**	**100**	**500**
1	-	0.04161 (*)	0.01321 (*)	5.546e-06 (***)	3.542e-14 (***)
10	0.04161 (*)	-	0.6659 (ns)	0.001125 (**)	5.994e-14 (***)
50	0.01321 (*)	0.6659 (ns)	-	0.002561 (**)	4.698e-14 (***)
100	5.546e-06 (***)	0.001125 (**)	0.002561 (**)	-	1.7e-13 (***)
500	3.542e-14 (***)	5.994e-14 (***)	4.698e-14 (***)	1.7e-13 (***)	-

In the symmetric zigzag 25 µm × 45 µm channel operated at 4 µL/min (black curve in Figure 4-4), the first separated CI is likewise at 100 CFU/mL, giving an LOD of 10^2 CFU/mL, while the LOQ becomes 500 CFU/mL.

These results imply that using zigzag microchannels, though might not be helpful in lower flow rates, but in higher flow rates they outperform straight channels while reducing the testing time.

Compared to standard naked-eye colorimetric read-outs, all thermo-photonic methods achieve substantial gains in detection sensitivity. Samadi et al. [136] reduced the visual detection limit for THC from approximately 10 ng/m to 2 ng/mL (a 5-fold improvement) using a low-cost lock-in

thermography attachment. Thapa et al. [122] applied a similar approach to SARS-CoV-2 antibody LFAs, enabling detection at IgG concentrations roughly 3–4 times lower than the visual threshold, while maintaining a handheld, sub-$1,000 design. In contrast, my thermo-photonic platform reduces the *E. coli* detection limit from ~50,000 CFU/mL (visually) to 1,000 CFU/mL representing a 50-fold improvement without enrichment, and up to 500-fold with upstream microfluidic enrichment. These results extend thermo-photonic LFA applications from small molecules and antibodies to whole-cell bacterial targets, without compromising portability or cost-effectiveness.

Chapter 5

5 Thesis Summary and Future Work

5.1 Thesis Summary

This thesis develops and evaluates an integrated workflow that enhances the analytical performance of lateral flow assays (LFAs) by coupling viscoelastic microfluidic enrichment with thermo-photonic (lock-in thermography) readout. The microfluidic module concentrates bacteria into a narrow centreline stream using polymer-induced elastic forces, after which the enriched sample is dispensed onto a commercial LFA and quantitatively interrogated with an intensity-modulated laser and infrared camera to produce amplitude maps of the test and control lines.

On the methods side, viscoelastic working fluids were prepared by dissolving high-molecular-weight polyethylene oxide (PEO, Mw ≈ 2×10^6 Da) to 0–1000 ppm, and fluorescent polystyrene beads of 1.12 µm and 3.93 µm diameter were used as size surrogates during device design and optimization. Bacterial stocks were cultured, enumerated by serial dilution and spread plating, and applied to LFAs; microchannels were fabricated via SU-8 photolithography and PDMS soft lithography, and particle trajectories were acquired on an inverted microscope for subsequent ImageJ/MATLAB analysis. The thermo-photonic reader demodulated image sequences at the drive frequency to yield amplitude/phase images, from which normalized test-to-control intensities were extracted for calibration and limit-of-detection analysis.

A systematic parametric study established how Reynolds number (Re), elasticity number (El), aspect ratio (AR), and geometry (straight versus zigzag) govern viscoelastic focusing. For 1 µm surrogates, focusing quality, quantified as the fraction recovered in the central 10 % of the outlet, degraded with increasing Re and improved with El; the best performance was obtained at moderate Re (~1), high El, low AR (≈0.5), and in straight channels with minimal curvature. Exceptions at specific AR/Re windows were noted but did not alter the global trend.

For 4 µm particles, the same Re–El balance applied, but absolute channel size and confinement ratio (β) became more limiting: square 75×75 µm channels consistently under-performed because both inertial-lift and elastic forces were too weak to achieve sharp focusing, whereas narrower/taller sections recovered focusing provided Re was controlled. Increasing curvature (zigzag factor) or AR generally worsened focusing at moderate–high Re, again underscoring the advantage of straight, more confined paths.

Guided by these trends, enrichment experiments transitioned from beads to bacteria. GFP-expressing *E. coli* OP50 exhibited lateral migration most similar to 1 µm particles, validating the

use of bead-optimized, low-AR straight channels and 1000 ppm PEO for bacterial enrichment. In the straight 25×25 μm channel at 2 μL min^{-1}, mean capture efficiency was 90.24 % (SEM = 1.09 %); relaxing vertical confinement to 25×45 μm at the same flow increased efficiency to 96.24 % (SEM = 1.16 %; Tukey p = 0.0079), while a zigzag 25×45 μm configuration tested at higher flow offered no advantage and was excluded from further comparisons (ANOVA across conditions p = 0.0003).

The integrated workflow delivered two principal gains at the LFA stage. First, viscoelastic enrichment alone improved the naked-eye (colorimetric) visual LOD from ~50,000 to ~5,000 CFU/mL when using a straight 25×25 μm channel at 2 μL/min with 1000 ppm PEO; four devices in parallel processed 100 μL in ~120 min for each strip. Second, thermo-photonic interrogation of non-enriched LFAs established a baseline LOD of 10^3 CFU/mL (LOQ 5×10^3 CFU/mL), demonstrating a 50-fold improvement over visual reads. With upstream enrichment, the reader achieved LODs down to 10^2–5×10^2 CFU/mL depending on channel geometry, with matched-dimension straight channels performing best and being the only condition with a clearly assignable LOQ one step above its LOD. Table *5-1* highlights the key performance advantages of the integrated enrichment–photothermal LFA platform compared with conventional colorimetric LFAs.

Table 5-1 Detection characteristics and performance comparisonI

Metric	**Conventional colorimetric LFA**	**This work: Enrichment+ LFA + PT**

Detection principle	Visual color change from accumulated GNPs	Active photothermal transduction of GNPs with lock-in detection
Sensitivity mechanism	Passive signal formation; limited by eye/optical contrast	Dual amplification: target pre-concentration + thermal signal extraction
Limit of detection (LOD)	~5×10^4 CFU/mL	~10^2 CFU/mL
Signal-to-noise ratio	Low at weak test lines	High SNR via modulated excitation and FFT-based lock-in filtering
Quantification capability	Qualitative, observer-dependent	Fully quantitative (pixel-wise PT amplitude, T/C ratio)
Early-stage infection detection	Often unreliable	Enabled through low-burden detection
Clinical value	Rapid screening	Enhanced sensitivity without changing LFA chemistry

Traditional LFAs are inherently limited by passive signal generation and subjective optical readout, which restrict sensitivity and quantitative reliability at low bacterial concentrations. In contrast, the approach presented in this work leverages upstream microfluidic enrichment to increase target availability at the test line, coupled with photothermal lock-in detection to actively extract gold-nanoparticle signals with high signal-to-noise ratio. This combination enables reliable

quantification and substantially lowers the detection limit to ~10^2 CFU/mL, extending the effective dynamic range beyond that achievable by visual inspection. Importantly, these gains are achieved without altering LFA chemistry, positioning the proposed platform as a scalable and broadly compatible strategy for enhancing LFA performance in low-burden diagnostic applications.

Overall, this work (i) clarifies design rules for elasto-inertial focusing of ~1 μm-scale targets in short, low-AR rectangular channels; (ii) quantifies how those rules translate into capture efficiency with real bacteria; and (iii) shows that combining microfluidic pre-concentration with lock-in thermography materially extends LFA sensitivity without sacrificing portability or workflow simplicity. The methodology, ranging from polymer preparation and culture/enumeration to SU-8/PDMS microfabrication, imaging/analysis pipelines, and thermo-photonic demodulation, provides a reproducible route to translate basic focusing physics into practical diagnostic gains.

5.2 Thesis Limitations and Proposed Future Work

Several avenues can further mature this platform into a robust, clinically deployable diagnostic.

First, channel mechanics and materials merit attention. The present devices leverage PDMS for rapid iteration; however, PDMS compliance can attenuate inertial/elastic stress fields and introduce subtle curvature under pressure. The Z RISE study [78] demonstrated that a rigid, 3D-printed symmetric zigzag channel could achieve inertial focusing of particles as small as 3 μm in a Newtonian fluid (water or MACS buffer), with effective focusing observed down to a confinement ratio of $a/D_h \approx 0.04$. Inspired by their channel layout, similar geometries were fabricated using soft PDMS, which is more compatible with downstream integration but introduces wall compliance. This study expands on Z RISE by exploring smaller particles (1 μm), asymmetric

zigzag geometries, and viscoelastic fluids (PEO solutions) to investigate how these factors influence particle focusing under visco inertial conditions. Notably, in water, the 1 μm particles did not focus in a 25 μm × 25 μm PDMS channel, which corresponds to the same confinement ratio ($a/D_h \approx 0.04$) where Z RISE reported clear focusing. This contrast highlights the critical role of channel rigidity and suggests that PDMS compliance may reduce the lift forces necessary for inertial focusing on this scale. Replicating the optimized geometries in glass or silicon, or in stiffer polymers via injection molding, should sharpen focusing at a given Re and enable higher-throughput operation before focusing degrades.

Furthermore, by introducing asymmetric zigzag paths and tuning the aspect ratio, geometric asymmetry and viscoelastic stress gradients effect on modulating the focusing behavior in non-Newtonian systems was systematically investigated. Complementary CFD with viscoelastic constitutive models can be used to map sensitivity to wall compliance and to deconvolve the contributions of inertial lift, elastic lift, and secondary flows across AR and β.

Second, fluid rheology can be broadened beyond a single PEO concentration. Exploring higher-El regimes (e.g., 1500–3000 ppm PEO for the same Mw) and alternative polymers with different relaxation spectra (PVP, PAM, Xanthan) would test whether the current design rules hold when El is varied independently of channel size. Temperature-dependent measurements could further tune relaxation time (λ) in situ to maintain El in the favorable window as volumetric flow is increased.

Third, geometry and layout can be optimized for both focusing and sample-to-answer time. The enrichment step currently uses four parallel devices to prepare ~100 μL in ~120 min per test; increasing parallelization with fluidic manifolds, shortening focusing lengths by introducing gentle contractions before the expansion zone, and multiplexing center outlets could reduce preparation

to tens of minutes without compromising capture. Integrating capillary-driven collection from the center outlet directly onto the LFA pad would remove manual transfer and standardize applied volume.

Fourth, reader performance can be advanced along three axes: excitation, demodulation, and analytics. Hardware-wise, maintaining uniform line illumination while minimizing off-band heating will benefit from beam-shaping optics and careful wavelength selection matched to label absorption. On the signal side, multifrequency or chirped excitation combined with pixel-wise lock-in can improve background rejection against membrane heterogeneity; phase metrics and amplitude–phase composites should be explored alongside amplitude alone as calibration readouts. The existing demodulation and histogram-based normalization pipeline provides a solid baseline; converting it into a fully automated ROI-selection and ratiometric analysis suite with cross-strip self-calibration will facilitate reproducibility across strips, lots, and operators.

Fifth, analytical and clinical validation should proceed in progressively more realistic matrices. Experiments with the target O157:H7 strain prepared at known concentrations can be extended to spiked human urine and then to de-identified clinical remnants to quantify matrix effects, specificity against non-target strains, and lot-to-lot variability of strips. Parallel testing with culture/qPCR readouts will establish accuracy, while repeated-measures designs will refine precision, LOD, and LOQ in accordance with CLSI guidelines.

Finally, the application scope can broaden beyond bacteria. The same enrichment–reader architecture is well-suited to other micrometre-scale targets such as yeast or certain blood cells, and with appropriate labels to nanoparticles for antigen or nucleic-acid LFAs. A compact cartridge integrating the optimized straight, low-AR focusing stage upstream of a standard LFA and a handheld thermo-photonic head would deliver a turnkey point-of-need system with improved

sensitivity, short time-to-result, and minimal user steps, building directly on the reproducible methods and performance gains established here.

References

1. Ieiri, N., Hotta, O. & Taguma, Y. Impact of Annual Urine Health Check-Up System to Obtain Clinical Remission in Patients with IgA Nephropathy. in *IgA Nephropathy Today* 104–108 (KARGER, Basel, 2007). doi:10.1159/000102312.

2. Foxman, B. The epidemiology of urinary tract infection. *Nat Rev Urol* 7, 653–660 (2010).

3. Stamm, W. E. & Norrby, S. R. Urinary Tract Infections: Disease Panorama and Challenges. *J Infect Dis* 183, S1–S4 (2001).

4. Flores-Mireles, A. L., Walker, J. N., Caparon, M. & Hultgren, S. J. Urinary tract infections: epidemiology, mechanisms of infection and treatment options. *Nat Rev Microbiol* 13, 269–284 (2015).

5. Mobley, H. L. T. . & Warren, J. W. . *Urinary Tract Infections : Molecular Pathogenesis and Clinical Management*. (ASM Press, 1996).

6. Foxman, B. Epidemiology of urinary tract infections: incidence, morbidity, and economic costs. *Am J Med* 113, 5–13 (2002).

7. Hooton, T. M. & Stamm, W. E. DIAGNOSIS AND TREATMENT OF UNCOMPLICATED URINARY TRACT INFECTION. *Infect Dis Clin North Am* 11, 551–581 (1997).

8. Huang, E. S. & Stafford, R. S. National Patterns in the Treatment of Urinary Tract Infections in Women by Ambulatory Care Physicians. *Arch Intern Med* 162, 41–47 (2002).

9. Wigton, R. S. *et al.* Variation by specialty in the treatment of urinary tract infection in women. *J Gen Intern Med* 14, 491–494 (1999).

10. Olesen, F. & Oestergaard, I. Patients with urinary tract infection: proposed management strategies of general practitioners, microbiologists and urologists. *Br J Gen Pract* 45, 611–3 (1995).

11. Schmiemann, G., Kniehl, E., Gebhardt, K., Matejczyk, M. M. & Hummers-Pradier, E. The Diagnosis of Urinary Tract Infection. *Dtsch Arztebl Int* https://doi.org/10.3238/arztebl.2010.0361 (2010) doi:10.3238/arztebl.2010.0361.

12. Drysdale, D. R. Escherichia coli (E coli) Infections. Preprint at https://emedicine.medscape.com/article/217485-overview (2024).

13. Kunin, C. M. . *Detection, Prevention, and Management of Urinary Tract Infections*. (Lea & Febiger, 1987).

14. Arredondo, A. R., Dorval, B. L., Klibanov, A. M. & Lewis, K. Rapid immunodetection of Escherichia coli. *Biotechnol Lett* 22, 547–550 (2000).

15. Hooton, T. M. & Stamm, W. E. DIAGNOSIS AND TREATMENT OF UNCOMPLICATED URINARY TRACT INFECTION. *Infect Dis Clin North Am* 11, 551–581 (1997).

16. Barber, A. E., Norton, J. P., Spivak, A. M. & Mulvey, M. A. Urinary Tract Infections: Current and Emerging Management Strategies. *Clinical Infectious Diseases* 57, 719–724 (2013).

17. ANDERSON, G., DODSON, K., HOOTON, T. & HULTGREN, S. Intracellular bacterial communities of uropathogenic in urinary tract pathogenesis. *Trends Microbiol* 12, 424–430 (2004).

18. Smelov, V., Naber, K. & Bjerklund Johansen, T. E. Improved Classification of Urinary Tract Infection: Future Considerations. *European Urology Supplements* 15, 71–80 (2016).

19. Lam, C.-W. *et al.* NMR-based metabolomic urinalysis: A rapid screening test for urinary tract infection. *Clinica Chimica Acta* 436, 217–223 (2014).

20. McIsaac, W. J. Validation of a Decision Aid to Assist Physicians in Reducing Unnecessary Antibiotic Drug Use for Acute Cystitis. *Arch Intern Med* 167, 2201 (2007).

21. Tarr, P. I. Escherichia coli 0157:H7: Clinical, Diagnostic, and Epidemiological Aspects of Human Infection. *Clinical Infectious Diseases* 20, 1–10 (1995).

22. Selim, S. A. *et al.* Prevalence and Characterization of Shiga-Toxin O157:H7 and Non-O157:H7 Enterohemorrhagic *Escherichia Coli* Isolated from Different Sources. *Biotechnology & Biotechnological Equipment* 27, 3834–3842 (2013).

23. Lepelletier, D., Caroff, N., Reynaud, A. & Richet, H. Escherichia coli: Epidemiology and Analysis of Risk Factors for Infections Caused by Resistant Strains. *Clinical Infectious Diseases* 29, 548–552 (1999).

24. Aminov, R. History of antimicrobial drug discovery: Major classes and health impact. *Biochem Pharmacol* 133, 4–19 (2017).

25. Shallcross, L. *et al.* Antibiotic prescribing for lower UTI in elderly patients in primary care and risk of bloodstream infection: A cohort study using electronic health records in England. *PLoS Med* 17, e1003336 (2020).

26. The 10 × ‘20 Initiative: Pursuing a Global Commitment to Develop 10 New Antibacterial Drugs by 2020. *Clinical Infectious Diseases* 50, 1081–1083 (2010).

27. Nace, D. A., Drinka, P. J. & Crnich, C. J. Clinical Uncertainties in the Approach to Long Term Care Residents With Possible Urinary Tract Infection. *J Am Med Dir Assoc* 15, 133–139 (2014).

28. O’Neill, J. *Rapid Diagnostics: Stopping Unnecessary Use of Antibiotics*. https://amr-review.org/sites/default/files/Rapid%20Diagnostics%20-%20Stopping%20Unnecessary%20use%20of%20Antibiotics.pdf (2015).

29. Wilson, M. L. & Gaido, L. Laboratory Diagnosis of Urinary Tract Infections in Adult Patients. *Clinical Infectious Diseases* 38, 1150–1158 (2004).

30. Schmiemann, G., Kniehl, E., Gebhardt, K., Matejczyk, M. M. & Hummers-Pradier, E. The Diagnosis of Urinary Tract Infection. *Dtsch Arztebl Int*

https://doi.org/10.3238/arztebl.2010.0361 (2010) doi:10.3238/arztebl.2010.0361.

31. Wagenlehner, F. *et al.* A global perspective on improving patient care in uncomplicated urinary tract infection: expert consensus and practical guidance. *J Glob Antimicrob Resist* 28, 18–29 (2022).

32. Nicolle, L. E. Urinary Tract Infections in Long-Term–Care Facilities. *Infect Control Hosp Epidemiol* 22, 167–175 (2001).

33. Schmiemann, G., Gágyor, I., Hummers-Pradier, E. & Bleidorn, J. Resistance profiles of urinary tract infections in general practice - an observational study. *BMC Urol* 12, 33 (2012).

34. Psotta, C., Chaturvedi, V., Gonzalez-Martinez, J. F., Sotres, J. & Falk, M. Portable Prussian Blue-Based Sensor for Bacterial Detection in Urine. *Sensors* 23, (2023).

35. Yao, Y. *et al.* Fast detection of E. coli with a novel fluorescent biosensor based on a FRET system between UCNPs and GO@Fe3O4in urine specimens. *Analytical Methods* 13, 2209–2214 (2021).

36. Yang, X., Wisuthiphaet, N., Young, G. M. & Nitin, N. Rapid detection of Escherichia coli using bacteriophage-induced lysis and image analysis. *PLoS One* 15, (2020).

37. Vendeville, J. B. *et al.* Fast Identification and Quantification of Uropathogenic E. coli through Cluster Analysis. *ACS Biomater Sci Eng* 8, 242–252 (2022).

38. Demirci, U. *et al.* Portable microfluidic chip for detection of Escherichia coli in produce and blood. *Int J Nanomedicine* 2591 (2012) doi:10.2147/IJN.S29629.

39. Li, Y. *et al.* Deep Learning-Enabled Detection and Classification of Bacterial Colonies Using a Thin-Film Transistor (TFT) Image Sensor. *ACS Photonics* 9, 2455–2466 (2022).

40. Yang, Y., Kim, S. & Chae, J. Separating and detecting escherichia coli in a microfluidic channel for urinary tract infection applications. *Journal of Microelectromechanical Systems* 20, 819–827 (2011).

41. Gür, S. D., Bakhshpour, M. & Denizli, A. Selective detection of Escherichia coli caused UTIs with surface imprinted plasmonic nanoscale sensor. *Materials Science and Engineering C* 104, (2019).

42. Koczula, K. M. & Gallotta, A. Lateral flow assays. *Essays Biochem* 60, 111–120 (2016).

43. Sajid, M., Kawde, A.-N. & Daud, M. Designs, formats and applications of lateral flow assay: A literature review. *Journal of Saudi Chemical Society* 19, 689–705 (2015).

44. Quesada-González, D. & Merkoçi, A. Nanoparticle-based lateral flow biosensors. *Biosensors and Bioelectronics* vol. 73 47–63 Preprint at https://doi.org/10.1016/j.bios.2015.05.050 (2015).

45. Li, G. *et al.* Lateral flow immunoassays for antigens, antibodies and haptens detection. *Int J Biol Macromol* 242, 125186 (2023).

46. Ross, G. M. S., Filippini, D., Nielen, M. W. F. & Salentijn, G. IJ. Unraveling the Hook Effect: A Comprehensive Study of High Antigen Concentration Effects in Sandwich Lateral Flow Immunoassays. *Anal Chem* 92, 15587–15595 (2020).

47. Pedreira-Rincón, J. *et al.* A comprehensive review of competitive lateral flow assays over the past decade. *Lab Chip* 25, 2578–2608 (2025).

48. Anfossi, L., Di Nardo, F., Cavalera, S., Giovannoli, C. & Baggiani, C. Multiplex Lateral Flow Immunoassay: An Overview of Strategies towards High-throughput Point-of-Need Testing. *Biosensors (Basel)* 9, 2 (2018).

49. Huang, Y., Su, Z., Li, W. & Ren, J. Recent Progresses on Biosensors for Escherichia coli Detection. *Food Anal Methods* 15, 338–366 (2022).

50. Cho, S., Park, T. S., Nahapetian, T. G. & Yoon, J.-Y. Smartphone-based, sensitive µPAD detection of urinary tract infection and gonorrhea. *Biosens Bioelectron* 74, 601–611 (2015).

51. Lehnert, T. & Gijs, M. A. M. Microfluidic systems for infectious disease diagnostics. *Lab Chip* 24, 1441–1493 (2024).

52. Wang, Y. C. *et al.* Turntable paper-based device to detect Escherichia coli. *Micromachines (Basel)* 12, (2021).

53. Wu, W. *et al.* A sensitive lateral flow biosensor for Escherichia coli O157:H7 detection based on aptamer mediated strand displacement amplification. *Anal Chim Acta* 861, 62–68 (2015).

54. Xiang, N. & Ni, Z. Hand-Powered Inertial Microfluidic Syringe-Tip Centrifuge. *Biosensors (Basel)* 12, 14 (2022).

55. Xiang, N., Li, Q. & Ni, Z. Combining Inertial Microfluidics with Cross-Flow Filtration for High-Fold and High-Throughput Passive Volume Reduction. *Anal Chem* 92, 6770–6776 (2020).

56. Labuz, J. M. & Takayama, S. Elevating sampling. *Lab Chip* 14, 3165–3171 (2014).

57. Rathore, A. S. & Shirke, A. RECENT DEVELOPMENTS IN MEMBRANE-BASED SEPARATIONS IN BIOTECHNOLOGY PROCESSES: REVIEW. *Prep Biochem Biotechnol* 41, 398–421 (2011).

58. Zhang, J. *et al.* Fundamentals and applications of inertial microfluidics: a review. *Lab Chip* 16, 10–34 (2015).

59. Martel, J. M. & Toner, M. Inertial Focusing in Microfluidics. *https://doi.org/10.1146/annurev-bioeng-121813-120704* 16, 371–396 (2014).

60. Amini, H., Lee, W. & Di Carlo, D. Inertial microfluidic physics. *Lab Chip* 14, 2739–2761 (2014).

61. Xuan, X. Recent advances in direct current electrokinetic manipulation of particles for microfluidic applications. *Electrophoresis* 40, 2484–2513 (2019).

62. Zhang, K. *et al.* Efficient Micro/Nanoparticle Concentration using Direct Current-Induced Thermal Buoyancy Convection for Multiple Liquid Media. *Anal Chem* 91, 4457–4465 (2019).

63. Du, K., Song, J., Liu, W., Tao, Y. & Ren, Y. Multifrequency Induced-Charge Electroosmosis. *Micromachines 2019, Vol. 10, Page 447* 10, 447 (2019).

64. Chen, Y. *et al.* Continuous enrichment of low-abundance cell samples using standing surface acoustic waves (SSAW). *Lab Chip* 14, 924–930 (2014).

65. Friend, J. & Yeo, L. Y. Microscale acoustofluidics: Microfluidics driven via acoustics and ultrasonics. *Rev Mod Phys* 83, 647–704 (2011).

66. Wang, J. *et al.* Ultrasensitive microfluidic immunosensor with stir bar enrichment for point-of-care test of Staphylococcus aureus in foods triggered by DNAzyme-assisted click reaction. *Food Chem* 378, 132093 (2022).

67. Yuan, D. *et al.* Recent progress of particle migration in viscoelastic fluids. *Lab Chip* 18, 551–567 (2018).

68. Yuan, D. *et al.* Continuous plasma extraction under viscoelastic fluid in a straight channel with asymmetrical expansion–contraction cavity arrays. *Lab Chip* 16, 3919–3928 (2016).

69. Zhang, P. *et al.* Facile syringe filter-enabled bacteria separation, enrichment, and buffer exchange for clinical isolation-free digital detection and characterization of bacterial pathogens in urine. *Analyst* 146, 2475–2483 (2021).

70. Kim, S. *et al.* Floating Magnetic Membrane for Rapid Enrichment of Pathogenic Bacteria. *Biochip J* 15, 61–68 (2021).

71. Kwon, K., Gwak, H., Hyun, K. A., Kwak, B. S. & Jung, H. Il. High-throughput microfluidic chip for magnetic enrichment and photothermal DNA extraction of foodborne bacteria. *Sens Actuators B Chem* 294, 62–68 (2019).

72. Du, X. *et al.* A nanowire-integrated thermoresponsive microfluidic platform for on-demand enrichment and colorimetric detection of pathogenic bacteria. *J Mater Chem B* 7, 7301–7305 (2019).

73. Peng, T., Qiang, J. & Yuan, S. Sheathless inertial particle focusing methods within microfluidic devices: a review. *Frontiers in Bioengineering and Biotechnology* vol. 11 Preprint at https://doi.org/10.3389/fbioe.2023.1331968 (2023).

74. Xiang, N. *et al.* Fundamentals of elasto-inertial particle focusing in curved microfluidic channels. *Lab Chip* 16, (2016).

75. Di Carlo, D., Irimia, D., Tompkins, R. G. & Toner, M. Continuous inertial focusing, ordering, and separation of particles in microchannels. *Proceedings of the National Academy of Sciences* 104, 18892–18897 (2007).

76. SEGRÉ, G. & SILBERBERG, A. Radial Particle Displacements in Poiseuille Flow of Suspensions. *Nature* 189, 209–210 (1961).

77. Di Carlo, D. Inertial microfluidics. *Lab Chip* 9, 3038–3046 (2009).

78. Razavi Bazaz, S. *et al.* Zigzag microchannel for rigid inertial separation and enrichment (Z-RISE) of cells and particles. *Lab Chip* 22, 4093–4109 (2022).

79. Liu, C. *et al.* Field-Free Isolation of Exosomes from Extracellular Vesicles by Microfluidic Viscoelastic Flows. *ACS Nano* 11, 6968–6976 (2017).

80. Zhou, Y., Ma, Z., Tayebi, M. & Ai, Y. Submicron Particle Focusing and Exosome Sorting by Wavy Microchannel Structures within Viscoelastic Fluids. *Anal Chem* 91, 4577–4584 (2019).

81. Charjouei Moghadam, M., Eilaghi, A. & Rezai, P. Elasto-inertial microparticle focusing in straight microchannels: A numerical parametric investigation. *Physics of Fluids* 33, (2021).

82. Zhang, T. *et al.* Bacteria separation and enrichment using viscoelastic flows in a straight microchannel. *Sens Actuators B Chem* 390, (2023).

83. Lim, H. *et al.* Separation and Washing of Candida Cells from White Blood Cells Using Viscoelastic Microfluidics. *Micromachines (Basel)* 14, 712 (2023).

84. Kumar, T. *et al.* High throughput viscoelastic particle focusing and separation in spiral microchannels. *Scientific Reports 2021 11:1* 11, 1–13 (2021).

85. Raoufi, M. A. *et al.* Effects of sample rheology on the equilibrium position of particles and cells within a spiral microfluidic channel. *Microfluid Nanofluidics* 25, 1–13 (2021).

86. Zhou, Y., Ma, Z. & Ai, Y. Sheathless inertial cell focusing and sorting with serial reverse wavy channel structures. *Microsyst Nanoeng* 4, 5 (2018).

87. Bilican, I. Cascaded contraction-expansion channels for bacteria separation from RBCs using viscoelastic microfluidics. *J Chromatogr A* 1652, (2021).

88. Suzuki, T. *et al.* Deciphering viscoelastic cell manipulation in rectangular microchannels. *Physics of Fluids* 35, (2023).

89. Raoufi, M. A. *et al.* Experimental and numerical study of elasto-inertial focusing in straight channels. *Biomicrofluidics* 13, (2019).

90. Liu, C. *et al.* Size-Based Separation of Particles and Cells Utilizing Viscoelastic Effects in Straight Microchannels. *Anal Chem* 87, 6041–6048 (2015).

91. Ramachandraiah, H., Svahn, H. A. & Russom, A. Inertial microfluidics combined with selective cell lysis for high throughput separation of nucleated cells from whole blood. *RSC Adv* 7, 29505–29514 (2017).

92. Zhu, S. *et al.* Inertial microfluidic cube for automatic and fast extraction of white blood cells from whole blood. *Lab Chip* 20, 244–252 (2020).

93. Park, J. Lateral Flow Immunoassay Reader Technologies for Quantitative Point-of-Care Testing. *Sensors* 22, 7398 (2022).

94. Guo, Z., Kang, Y., Liang, S. & Zhang, J. Detection of Hg(II) in adsorption experiment by a lateral flow biosensor based on streptavidin-biotinylated DNA probes modified gold nanoparticles and smartphone reader. *Environmental Pollution* 266, 115389 (2020).

95. Zhang, T. *et al.* A smartphone-based rapid quantitative detection platform for lateral flow strip of human chorionic gonadotropin with optimized image algorithm. *Microchemical Journal* 157, 105038 (2020).

96. Tiplady, S. Consumer Diagnostics—Clearblue Pregnancy and Fertility Testing. in *The Immunoassay Handbook* 537–540 (Elsevier, 2013). doi:10.1016/B978-0-08-097037-0.00037-3.

97. Koshy, T. I. & Buechler, K. F. The Triage ® System. in *The Immunoassay Handbook* 541–544 (Elsevier, 2013). doi:10.1016/B978-0-08-097037-0.00038-5.

98. Fraiwan, A., Kwan, L. & Choi, S. A disposable power source in resource-limited environments: A paper-based biobattery generating electricity from wastewater. *Biosens Bioelectron* 85, 190–197 (2016).

99. Zhu, X., Shah, P., Stoff, S., Liu, H. & Li, C. Z. A paper electrode integrated lateral flow immunosensor for quantitative analysis of oxidative stress induced DNA damage. *Analyst* 139, 2850–2857 (2014).

100. Perju, A. & Wongkaew, N. Integrating high-performing electrochemical transducers in lateral flow assay. *Anal Bioanal Chem* 413, 5535–5549 (2021).

101. Lan, T., Xiang, Y. & Lu, Y. Detection of Protein Biomarker Using a Blood Glucose Meter. in 99–109 (2015). doi:10.1007/978-1-4939-2172-0_7.

102. Gao, F. *et al.* Overview of the Design and Application of Photothermal Immunoassays. *Sensors* 24, 6458 (2024).

103. Ojaghi, A., Pallapa, M., Tabatabaei, N. & Rezai, P. High-sensitivity interpretation of lateral flow immunoassays using thermophotonic lock-in imaging. *Sens Actuators A Phys* 273, 189–196 (2018).

104. Ma, X., Ge, Y. & Xia, N. Overview of the Design and Application of Dual-Signal Immunoassays. *Molecules* 29, 4551 (2024).

105. Wen, C.-Y. *et al.* Colorimetric and photothermal dual-mode lateral flow immunoassay based on Au-Fe3O4 multifunctional nanoparticles for detection of Salmonella typhimurium. *Microchimica Acta* 190, 57 (2023).

106. Zhang, W.-Y. *et al.* A Paper-Based Analytical Device Integrated with Smartphone: Fluorescent and Colorimetric Dual-Mode Detection of β-Glucosidase Activity. *Biosensors (Basel)* 12, 893 (2022).

107. Imhof, R. E., Zhang, B. & Birch, D. J. S. Photothermal Radiometry for NDE. in *Non-Destructive Evaluation: Progress in Photothermal and Photoacoustic Science and Technology* (ed. Mandelis, A.) vol. 7 185–236 (PTR Prentice Hall, Edgewood Cliffs, New Jersey, 1994).

108. Maris, H. & Balibar, S. Diffusion waves and their uses. *Phys Today* 53, 29–34 (2000).

109. Tabatabaei, N. Development of Frequency and Phase Modulated Thermal-wave Methodologies for Materials Non-destructive Evaluation and Thermophotonic Imaging of Turbid Media. (University of Toronto, 2012).

110. Ojaghi, A. Development of Frequency and Phase Modulated Thermal-wave Methodologies for Materials Non-destructive Evaluation and Thermophotonic Imaging of Turbid Media. (University of Toronto, 2012).

111. Fourier, J. *Théorie Analytique de La Chaleur*. (Chez Firmin Didot, père et fils, Paris, 1822).

112. Angström, A. XVII. New method of determining the thermal conductibility of bodies. *The London, Edinburgh, and Dublin Philosophical Magazine and Journal of Science* 25, 130–142 (1863).

113. Busse, G., Wu, D. & Karpen, W. Thermal wave imaging with phase sensitive modulated thermography. *J Appl Phys* 71, 3962–3965 (1992).

114. Kuo, P. & others. Parallel thermal wave imaging using a vector lock-in video technique. in *Photoacoustic and Photothermal Phenomena* 415–418 (Springer, 1988).

115. Beaudoin, J. L. & others. Numerical system for infrared scanners and application to the subsurface control of materials by photothermal radiometry. in *1985 International Technical Symposium/Europe* (International Society for Optics and Photonics, 1986).

116. Carlomagno, G. & Berardi, P. G. Unsteady thermotopography in non-destructive testing. in *Proc. 3rd Biannual Exchange* (St. Louis, USA, 1976).

117. An, Y.-K., Kim, J. M. & Sohn, H. Laser lock-in thermography for detection of surface-breaking fatigue cracks on uncoated steel structures. *NDT & E International* 65, 54–63 (2014).

118. Giorleo, G., Meola, C. & Squillace, A. The use of lock-in thermography in industrial applications. *Nondestructive Testing and Evaluation* 16, 15–29 (2000).

119. Meola, C. & others. Nondestructive evaluation of fiber reinforced polymers with lock-in thermography. in *Residual Stress, Thermomechanics & Infrared Imaging, Hybrid Techniques and Inverse Problems, Volume 8* 207–213 (Springer, 2014).

120. Meola, C. & Carlomagno, G. The Role of Infrared Thermography in NDT. in *Nondestructive Testing of Materials and Structures* 91–96 (Springer, 2013).

121. Shirshahi, V., Tabatabaei, S. N., Hatamie, S. & Saber, R. Photothermal enhancement in sensitivity of lateral flow assays for detection of E-coli O157:H7. *Colloids Surf B Biointerfaces* 186, (2020).

122. Thapa, D., Samadi, N. & Tabatabaei, N. Handheld Thermo-Photonic Device for Rapid, Low-Cost, and On-Site Detection and Quantification of Anti-SARS-CoV-2 Antibody. *IEEE Sens J* 21, 18504–18511 (2021).

123. Thapa, D. *et al.* Rapid and Low-Cost Detection and Quantification of SARS-CoV-2 Antibody Titers of ICU Patients with Respiratory Deterioration Using a Handheld Thermo-Photonic Device. *Biomedicines* 10, (2022).

124. Hayden, D. *et al.* Arduino-Based Sensing Platform for Rapid, Low-Cost, and High-Sensitivity Detection and Quantification of Analytes in Fluidic Samples. in *The 9th International Electronic Conference on Sensors and Applications* 69 (MDPI, Basel Switzerland, 2022). doi:10.3390/ecsa-9-13277.

125. Nikdoost, A. *Investigation of Secondary (Dean) Flows in Curved Microchannels and Application to Microparticle Manipulation in Various Fluids*. (2022).

126. Oakey, J. *et al.* Particle Focusing in Staged Inertial Microfluidic Devices for Flow-Through Separation of Particles by Size. *Anal Chem* 82, 3862–3867 (2010).

127. *Basic Practical Microbiology: A Manual*. (Microbiology Society, London, 2016).

128. Mach, A. J. & di Carlo, D. Continuous scalable blood filtration device using inertial microfluidics. *Biotechnol Bioeng* 107, (2010).

129. Gervais, T., El-Ali, J., Günther, A. & Jensen, K. F. Flow-induced deformation of shallow microfluidic channels. *Lab Chip* 6, 500–507 (2006).

130. Schindelin, J. *et al.* Fiji: an open-source platform for biological-image analysis. *Nat Methods* 9, 676–682 (2012).

131. Karpen, W., Wu, D., Steegmüller, R. & Busse, G. Depth profiling of orientation in laminates with local lockin thermography. in *Proceedings of the 1994 International Conference on Quantitative InfraRed Thermography* (QIRT Council, 1994). doi:10.21611/qirt.1994.042.

132. Lu, X. *et al.* Sheathless and high-throughput elasto-inertial bacterial sorting for enhancing molecular diagnosis of bloodstream infection. *Lab Chip* 21, 2163–2177 (2021).

133. Tanriverdi, S. *et al.* Elasto-inertial focusing and particle migration in high aspect ratio microchannels for high-throughput separation. *Microsyst Nanoeng* 10, 87 (2024).

134. Liu, C. *et al.* Size-Based Separation of Particles and Cells Utilizing Viscoelastic Effects in Straight Microchannels. *Anal Chem* 87, 6041–6048 (2015).

135. Yang, S., Kim, J. Y., Lee, S. J., Lee, S. S. & Kim, J. M. Sheathless elasto-inertial particle focusing and continuous separation in a straight rectangular microchannel. *Lab Chip* 11, 266–273 (2011).

136. Thapa, D., Samadi, N., Patel, N. & Tabatabaei, N. Thermographic detection and quantification of THC in oral fluid at unprecedented low concentrations. *Biomed Opt Express* 11, 2178 (2020).

Appendices

Appendix A.

W	H	Dh	Betha	PEO
25	25	25	0.04	1000

Q	Uax	Re	El	Wi	Rep
2	0.05	0.81	17.84	14.51	0.03
4	0.11	1.65	17.63	29.01	0.07
8	0.21	3.33	17.41	58.03	0.13

Avg	90.23734

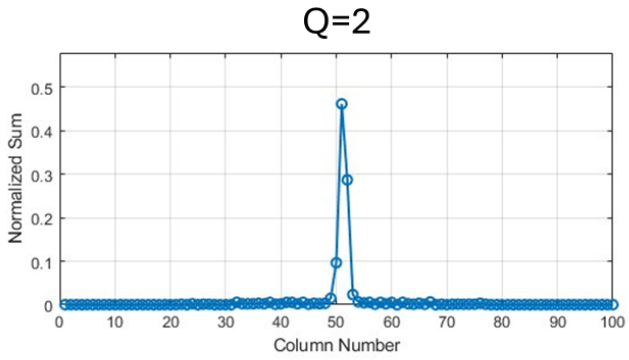

Avg	79.69112

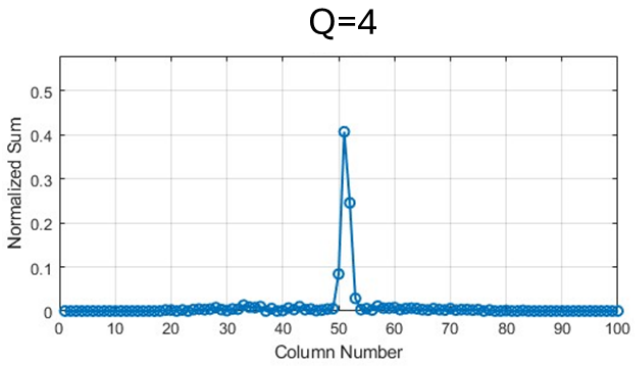

Avg	44.70747

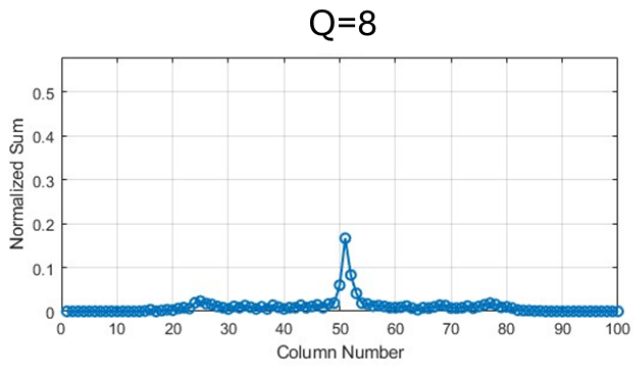

Appendix Figure A-0-1: Normalized average number of particles alongside their normalized lateral position for 1 µm particles inside a straight microchannel (25 × 25 µm^2) with 1000 ppm PEO at various flow rates.

W	H	Dh	Betha	PEO
25	25	25	0.04	1000

Q	Uax	Re	El	Wi	Rep
2	0.05	0.81	17.84	14.51	0.03
4	0.11	1.65	17.63	29.01	0.07
8	0.21	3.33	17.41	58.03	0.13

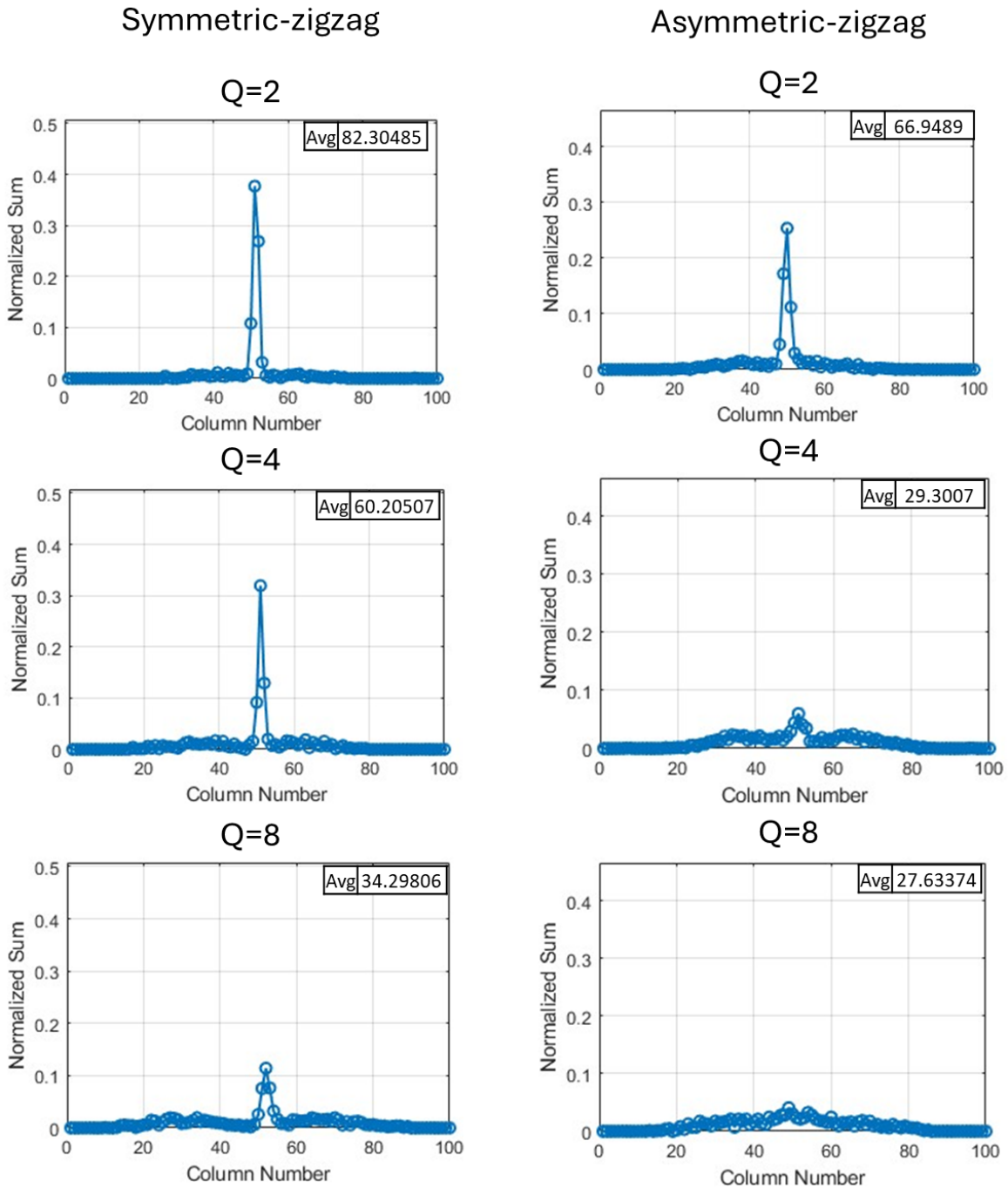

Appendix Figure A-0-2: Normalized average number of particles alongside their normalized lateral position for 1 µm particles inside a Asymmetric zigzag channel (right) and Symmetric zigzag channel (left) microchannel (25 × 25 µm^2) with 1000 ppm PEO at various flow rates.

W	H	Dh	Betha	PEO
25	45	32.14	0.031	1000

Q	Uax	Re	El	Wi	Rep
2	0.03	0.54	11.52	6.27	0.02
4	0.06	1.15	10.86	12.54	0.04
8	0.12	2.38	10.53	25.07	0.07

Avg	96.23

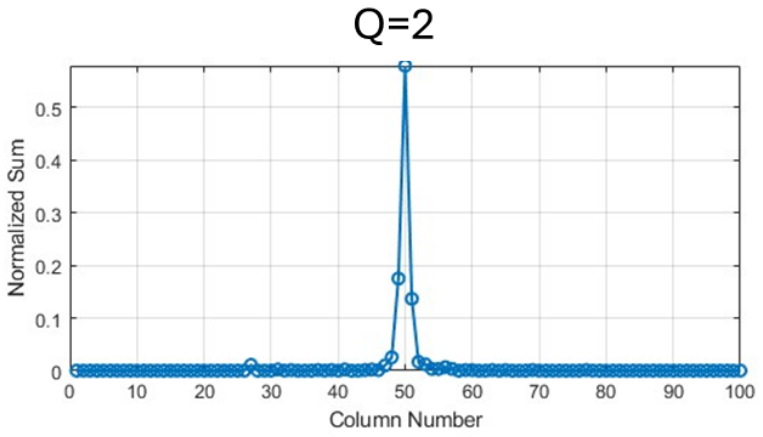

Avg	70.37

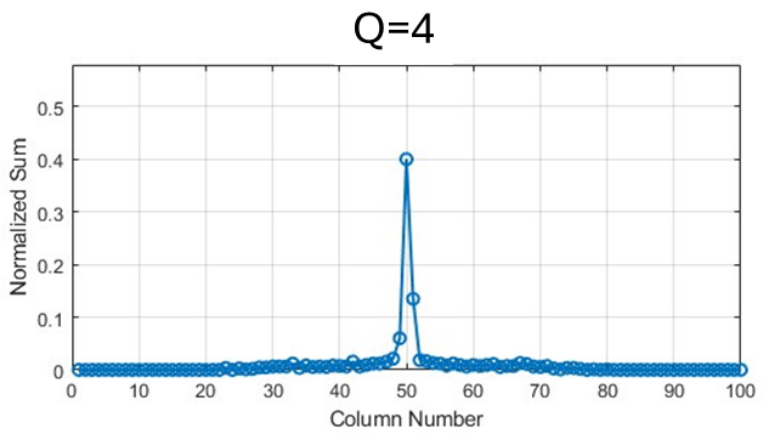

Avg	30.22

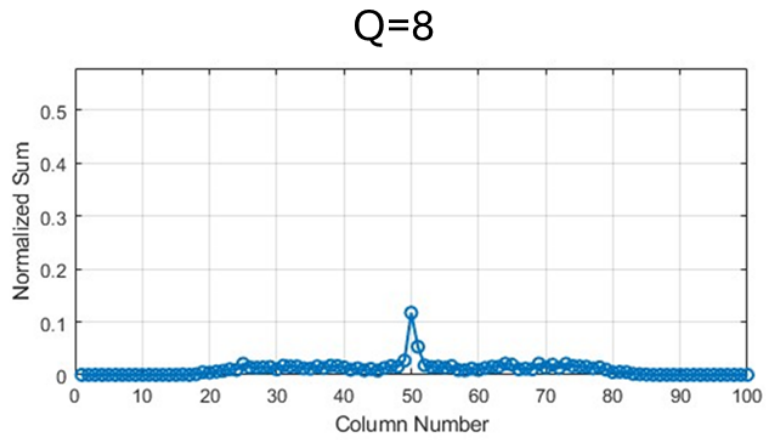

Appendix Figure A-0-3: Normalized average number of particles alongside their normalized lateral position for 1 µm particles inside a straight microchannel (25 × 45 µm^2) with 1000 ppm PEO at various flow rates.

W	H	Dh	Betha	PEO
25	45	32.14	0.04	1000

Q	Uax	Re	El	Wi	Rep	Dean
2	0.03	0.54	11.52	6.27	0.02	0.98
4	0.06	1.15	10.86	12.54	0.04	2.07
8	0.12	2.38	10.53	25.07	0.07	4.27

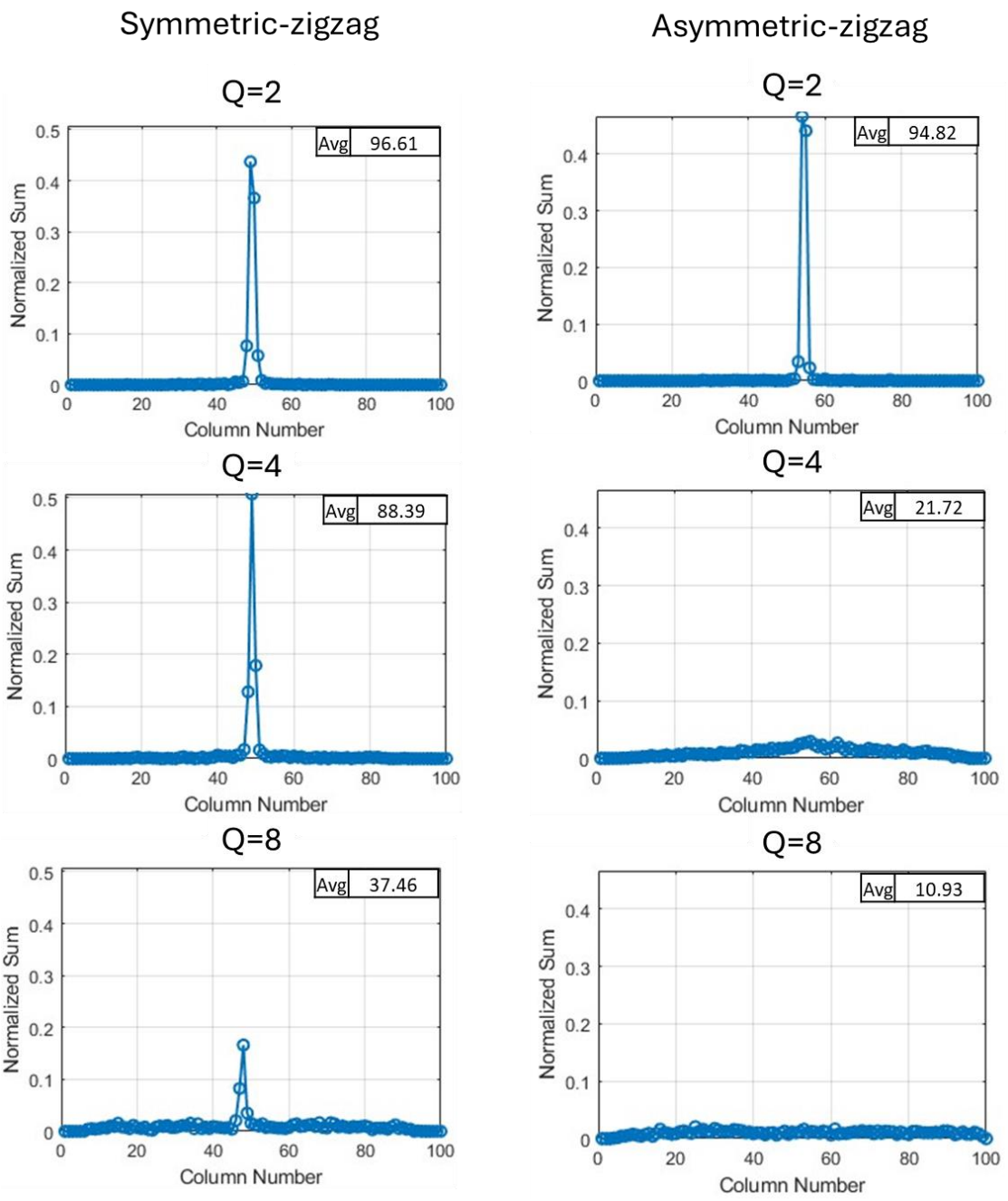

Appendix Figure A-0-4: Normalized average number of particles alongside their normalized lateral position for 1 µm particles inside a Asymmetric zigzag channel (right) and Symmetric zigzag channel (left) microchannel (25 × 45 µm^2) with 1000 ppm PEO at various flow rates.

W	H	Dh	Betha	PEO
45	25	32.14	0.031	1000

Q	Uax	Re	El	Wi	Rep
2	0.03	0.54	11.52	6.27	0.02
4	0.06	1.15	10.86	12.54	0.04
8	0.12	2.38	10.53	25.07	0.07

Avg	46.54

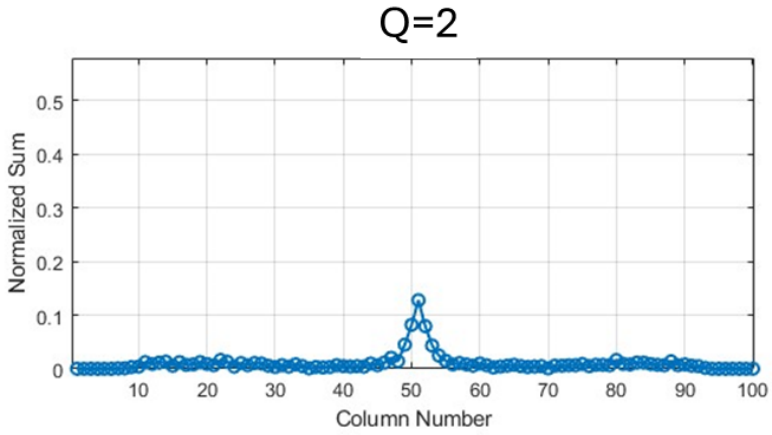

Avg	43.15

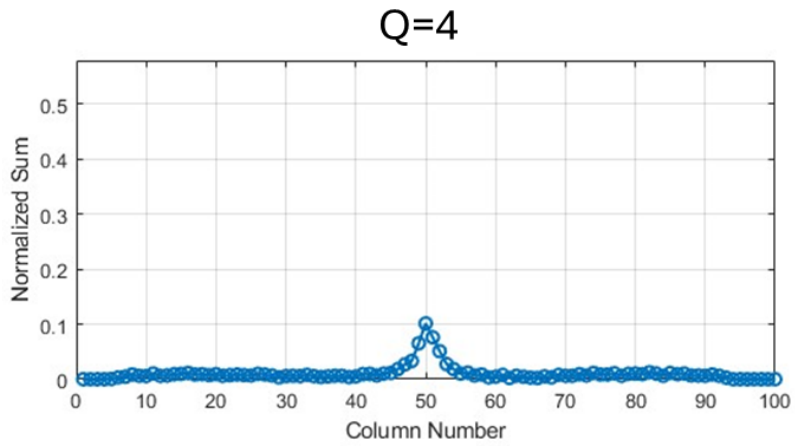

Avg	32.56

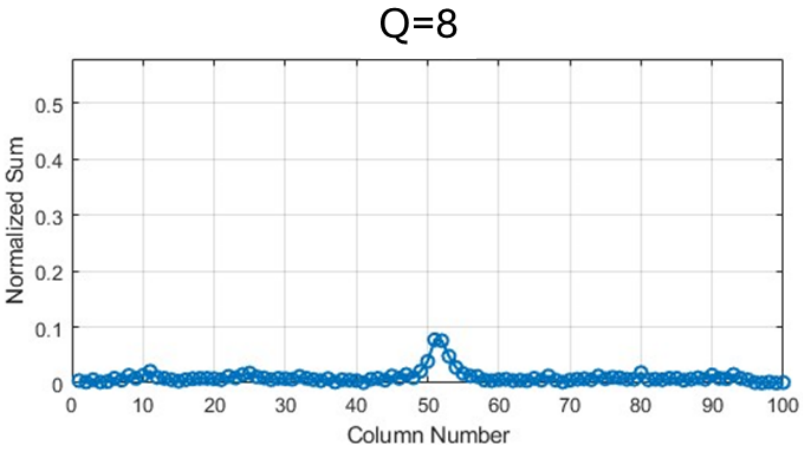

Appendix Figure A-0-5: Normalized average number of particles alongside their normalized lateral position for 1 µm particles inside a straight microchannel (45 × 25 µm^2) with 1000 ppm PEO at various flow rates.

W	H	Dh	Betha	PEO
45	25	32.14	0.04	1000

Q	Uax	Re	El	Wi	Rep	Dean
2	0.03	0.54	11.52	6.27	0.02	0.98
4	0.06	1.15	10.86	12.54	0.04	2.07
8	0.12	2.38	10.53	25.07	0.07	4.27

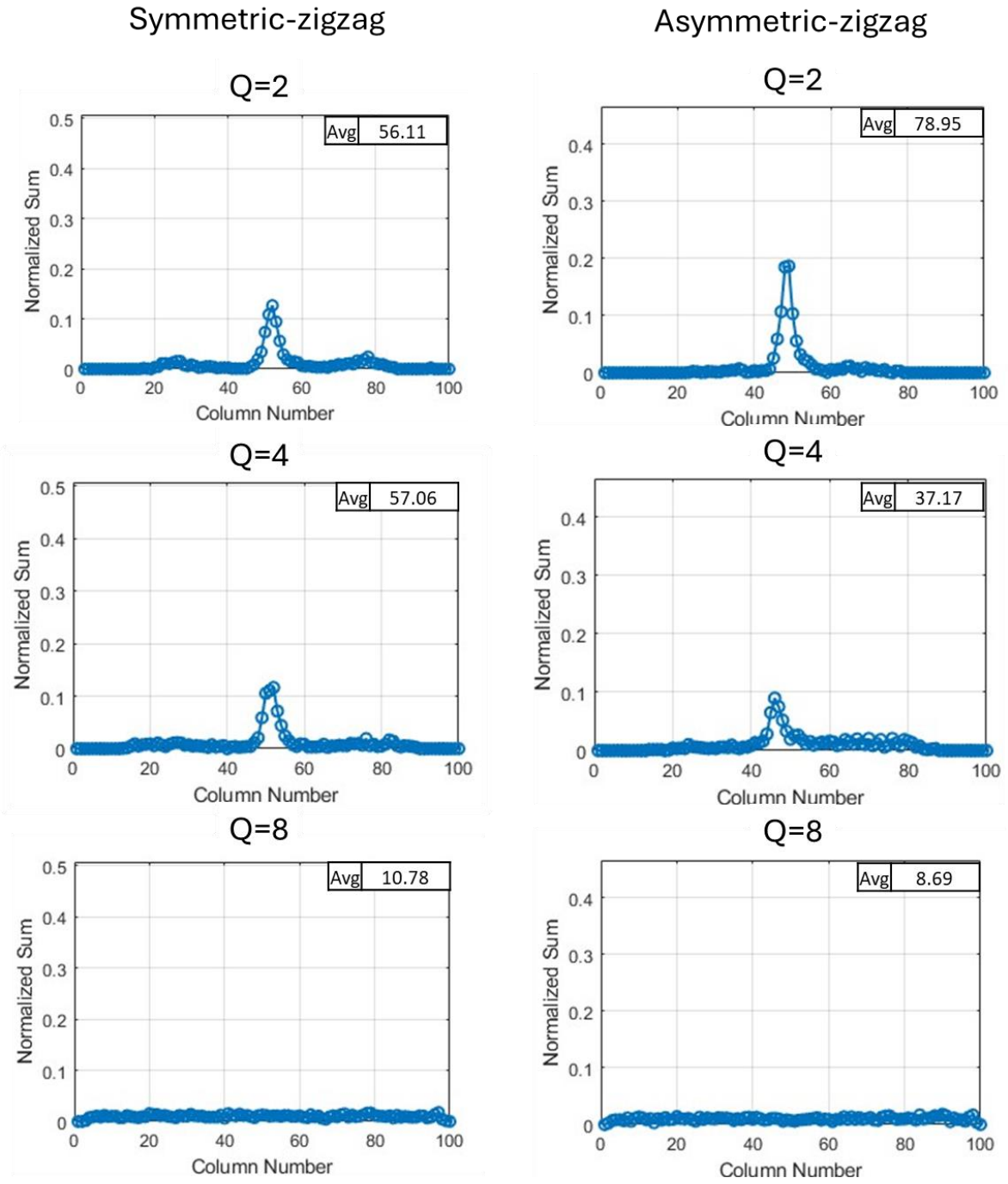

Appendix Figure A-0-6: Normalized average number of particles alongside their normalized lateral position for 1 µm particles inside a Asymmetric zigzag channel (right) and Symmetric zigzag channel (left) microchannel (45 × 25 µm^2) with 1000 ppm PEO at various flow rates.

W	H	Dh	Betha	PEO
75	75	75	0.053	1000

Q	Uax	Re	El	Wi	Rep
5	0.01	0.51	2.64	1.34	0.03
15	0.04	1.82	2.21	4.03	0.10
25	0.07	3.21	2.09	6.72	0.17

Avg	27.73

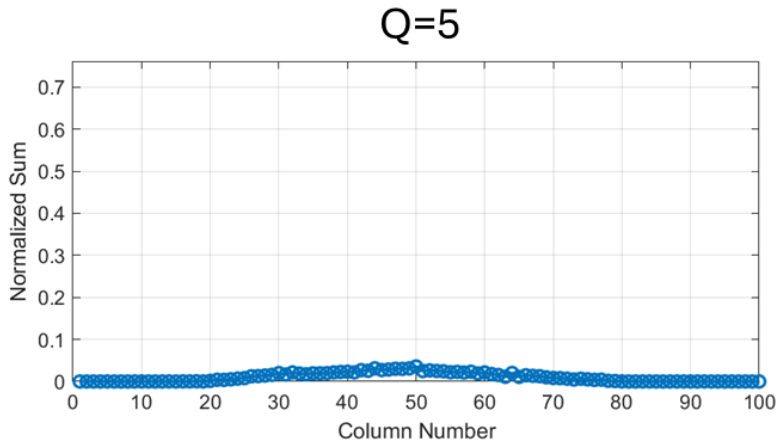

Avg	40.29

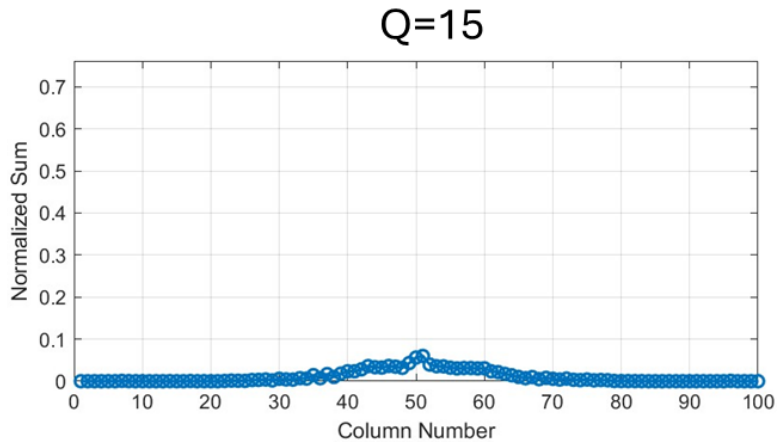

Avg	41.15

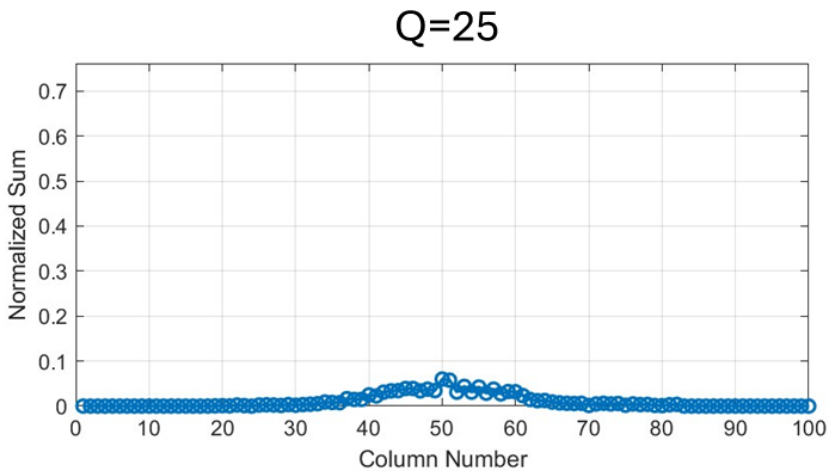

Appendix Figure A-0-7: Normalized average number of particles alongside their normalized lateral position for 4 µm particles inside a straight microchannel (75 × 75 µm^2) with 1000 ppm PEO at various flow rates.

W	H	Dh	Betha	PEO
75	75	75	0.053	1000

Q	Uax	Re	El	Wi	Rep	Dean
5	0.01	0.51	2.64	1.34	0.03	1.40
15	0.04	1.82	2.21	4.03	0.10	4.99
25	0.07	3.21	2.09	6.72	0.17	8.79

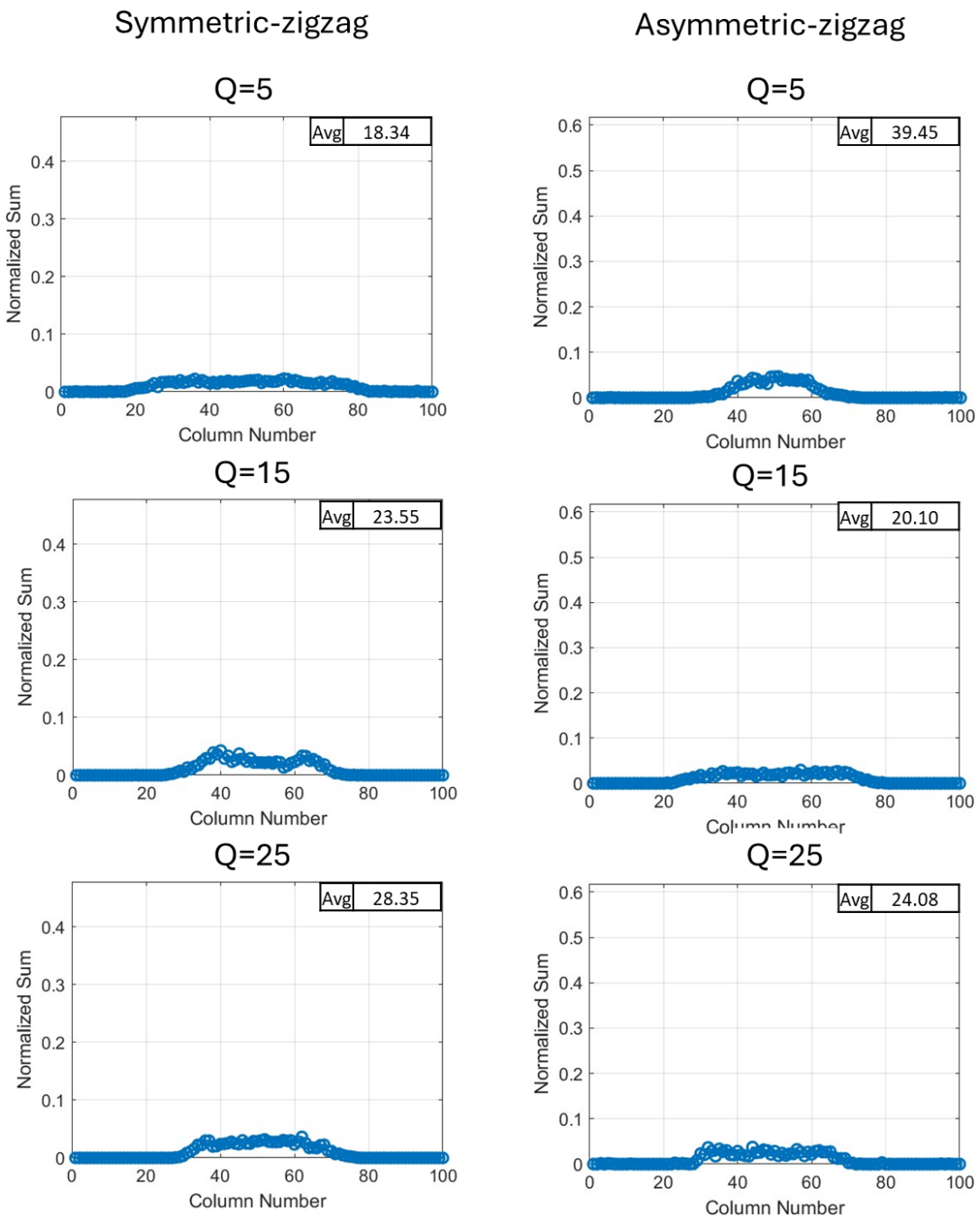

Appendix Figure A-0-8: Normalized average number of particles alongside their normalized lateral position for 4 µm particles inside a Asymmetric zigzag channel (right) and Symmetric zigzag channel (left) microchannel (75 × 75 µm^2) with 1000 ppm PEO at various flow rates.

W	H	Dh	Betha	PEO
75	45	75	0.071	1000

Q	Uax	Re	El	Wi	Rep
5	0.02	0.75	4.00	2.98	0.05
15	0.07	2.45	3.65	8.95	0.17
25	0.12	4.21	3.55	14.92	0.30

Avg	99.80

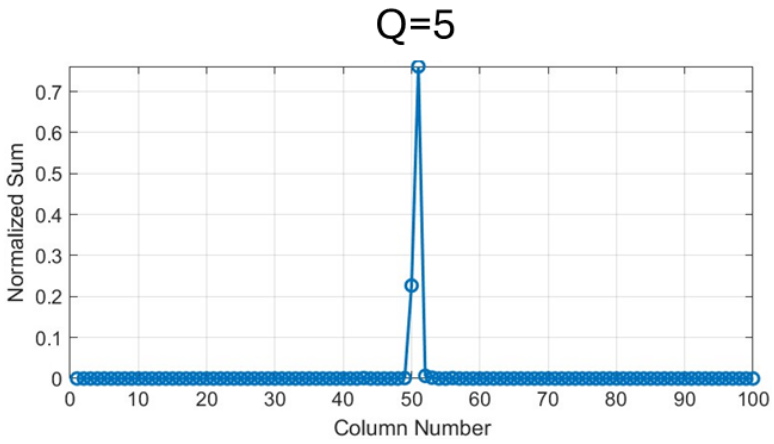

Avg	96.47

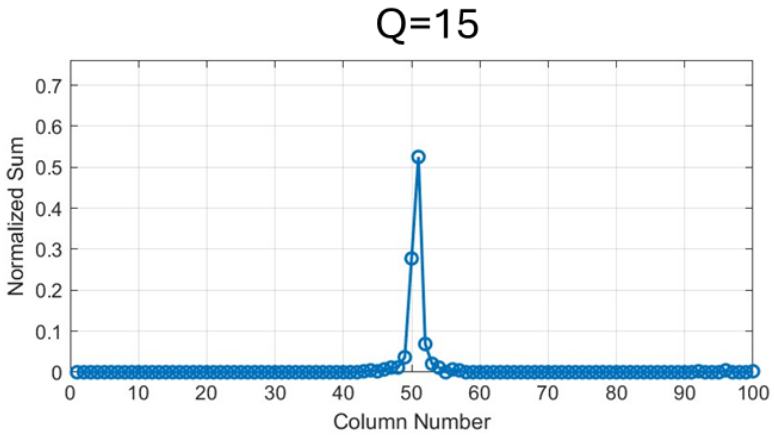

Avg	80.57

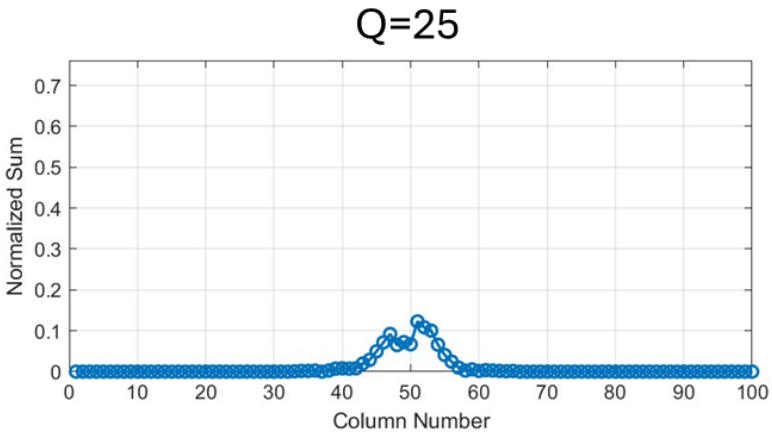

Appendix Figure A-0-9: Normalized average number of particles alongside their normalized lateral position for 4 µm particles inside a straight microchannel (75 × 45 µm^2) with 1000 ppm PEO at various flow rates.

W	H	Dh	Betha	PEO
75	45	75	0.071	1000

Q	Uax	Re	El	Wi	Rep	Dean
5	0.02	0.75	4.00	2.98	0.05	1.77
15	0.07	2.45	3.65	8.95	0.17	5.81
25	0.12	4.21	3.55	14.92	0.30	9.98

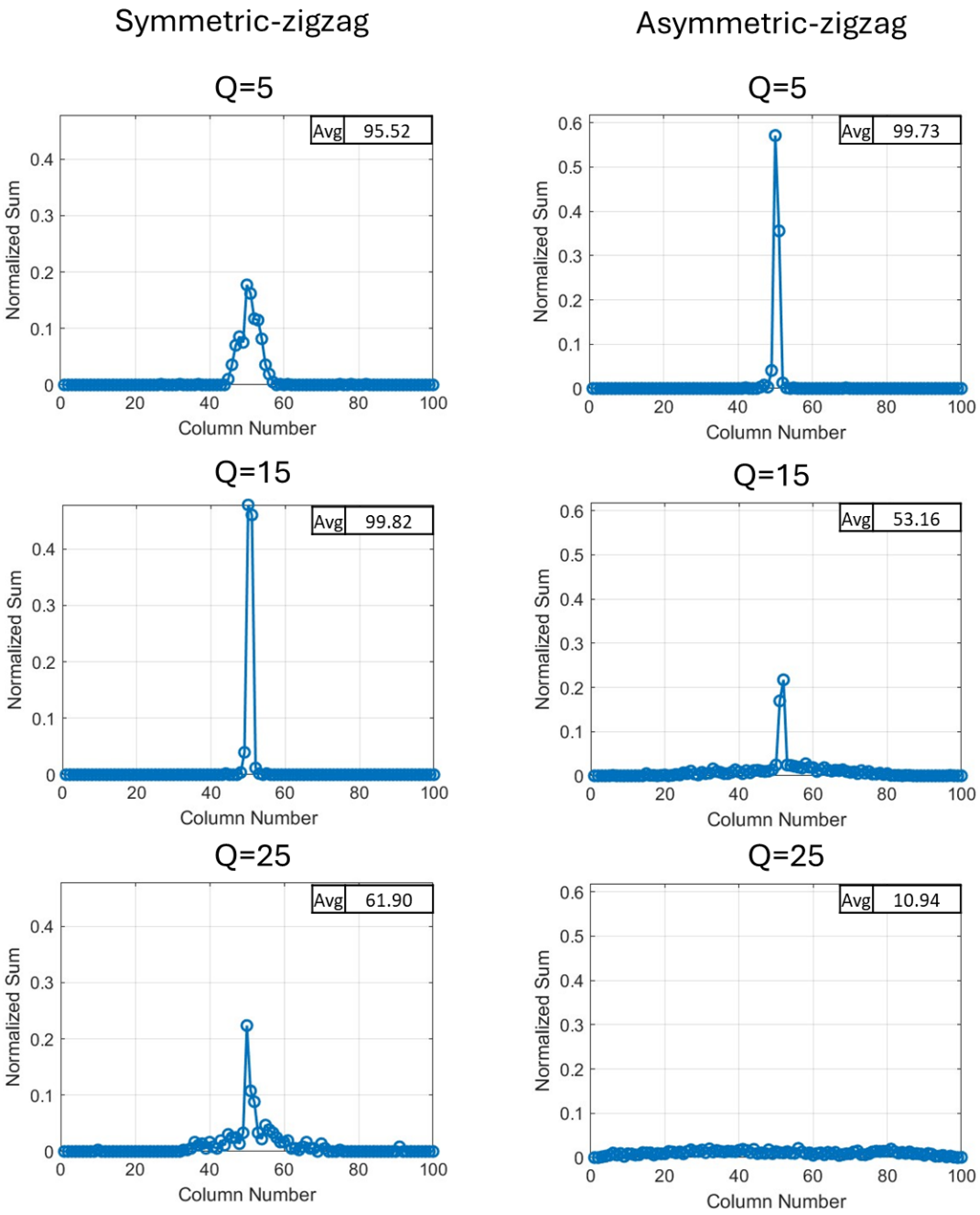

Appendix Figure A-0-10: Normalized average number of particles alongside their normalized lateral position for 4 µm particles inside a Asymmetric zigzag channel (right) and Symmetric zigzag channel (left) microchannel (75 × 45 µm^2) with 1000 ppm PEO at various flow rates.

W	H	Dh	Betha	PEO
45	75	75	0.071	1000

Q	Uax	Re	El	Wi	Rep
5	0.02	0.75	4.00	2.98	0.05
15	0.07	2.45	3.65	8.95	0.17
25	0.12	4.21	3.55	14.92	0.30

Avg	89.84

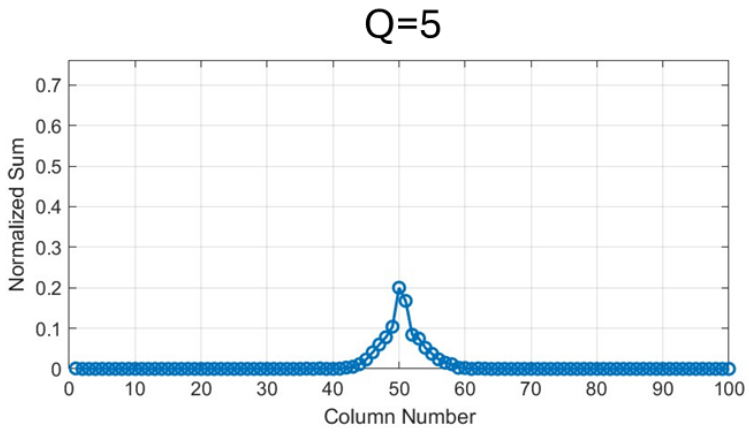

Avg	98.77

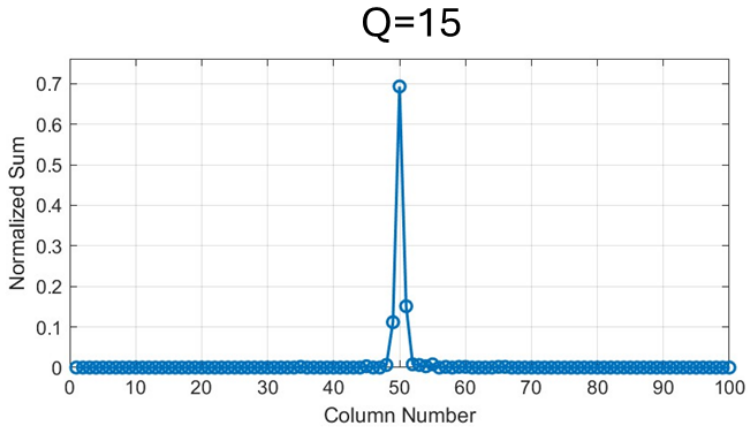

Avg	88.77

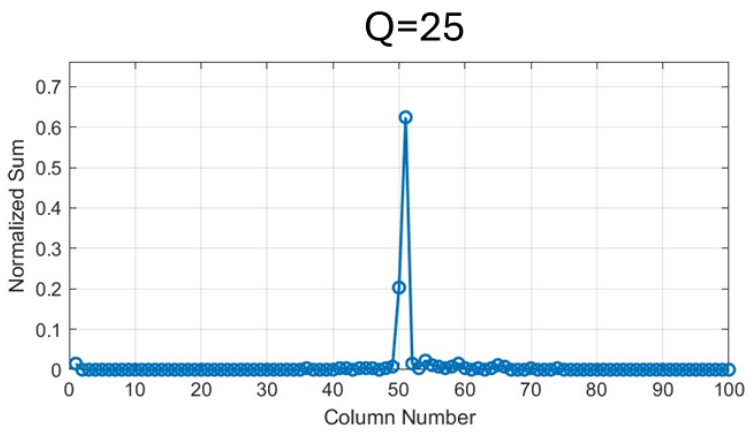

Appendix Figure A-0-11: Normalized average number of particles alongside their normalized lateral position for 4 µm particles inside a straight microchannel (45 × 75 µm^2) with 1000 ppm PEO at various flow rates.

W	H	Dh	Betha	PEO
45	75	75	0.071	1000

Q	Uax	Re	El	Wi	Rep	Dean
2	0.02	0.75	4.00	2.98	0.05	2.21
4	0.07	2.45	3.65	8.95	0.17	7.16
8	0.12	4.21	3.55	14.92	0.30	12.11

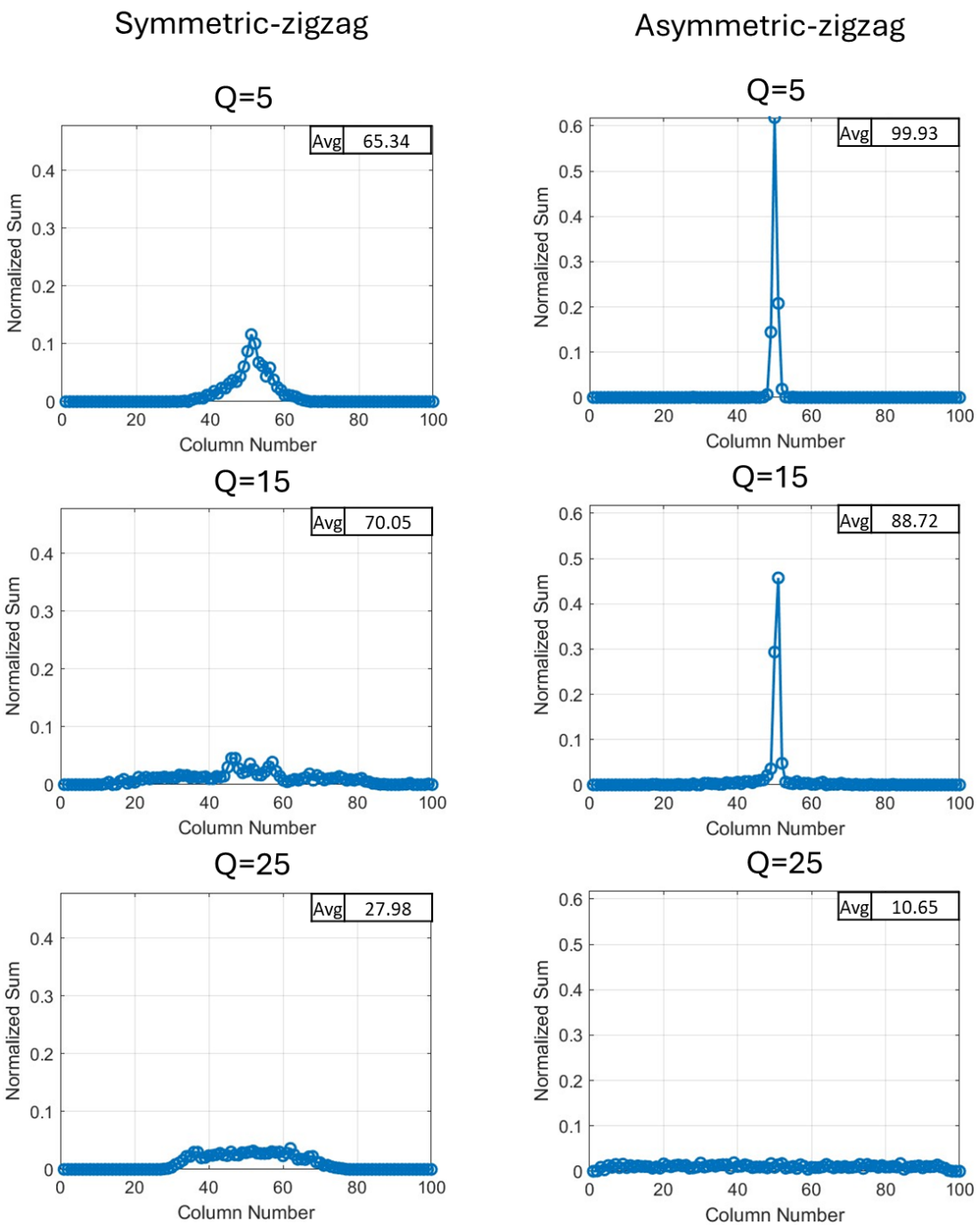

Appendix Figure A-0-12: Normalized average number of particles alongside their normalized lateral position for 4 µm particles inside a Asymmetric zigzag channel (right) and Symmetric zigzag channel (left) microchannel (45 × 75 µm^2) with 1000 ppm PEO at various flow rates.

Appendix B.

```
function combined_particle_tracking_gui()


    % Select the video file

    [fileName, filePath] = uigetfile({'*.avi;*.mp4', 'Video Files (*.avi, *.mp4)'},
'Select a Video File');

    if isequal(fileName, 0)

        disp('User selected Cancel');

        return;

    end

    videoFile = fullfile(filePath, fileName);


    % Load the video

    videoReader = VideoReader(videoFile);

    backgroundFrame = readFrame(videoReader);

    backgroundGray = rgb2gray(backgroundFrame);


    % Create a figure and UI controls

    hFig = figure('Name', 'Particle Tracking', 'NumberTitle', 'off', 'Position',
[100, 100, 1600, 800]);


    % Create axes for video display and plot

    hAxesOriginal = axes('Parent', hFig, 'Units', 'pixels', 'Position', [50, 350,
500, 400]);

    hAxesProcessed = axes('Parent', hFig, 'Units', 'pixels', 'Position', [650, 350,
500, 400]);

    hAxesPlot = axes('Parent', hFig, 'Units', 'pixels', 'Position', [1200, 50, 350,
700]);


    % Initialize variables
```

```
    selectedFrame = [];

    frameGray = [];

    frameBlurred = [];

    frameSubtracted = [];

    binaryFrame = [];

    threshold = 50;

    blurAmount = 2;

    areaOpen = 30;

    structElemSize = 2;

    frameNumber = 1;

    particleData = [];

    previousCentroids = [];

    particlePaths = {};

    kalmanFilters = {};

    numColumns = 10; % Default number of columns

    columnSpacing = 50; % Default column spacing

    normalizationFactor = 1; % Default normalization factor

    brightnessFactor = 1; % Default brightness factor

    contrastFactor = 1; % Default contrast factor

    finalCumulativeImage = []; % Initialize final cumulative image

    allParticleCounts = []; % Initialize allParticleCounts

    totalParticleCounts = []; % Initialize totalParticleCounts

    normalizedTotalParticleCounts = []; % Initialize normalizedTotalParticleCounts

    selectedRange = [1, numColumns]; % Default selected range


    % Create sliders and checkboxes for threshold adjustment, Gaussian blur,
background subtraction, brightness, and contrast
```

```
    createSlider(0, 255, threshold, [150, 80, 500, 20], @updateThreshold,
'Threshold');

    hSliderThreshold = findobj(hFig, 'Style', 'slider', 'Position', [150, 80, 500,
20]);

    hSliderLabelThreshold = findobj(hFig, 'Style', 'text', 'Position', [660, 80, 50,
20]);

    createSlider(0.1, 5, blurAmount, [150, 110, 500, 20], @updateBlur, 'Blur');

    hSliderBlur = findobj(hFig, 'Style', 'slider', 'Position', [150, 110, 500, 20]);

    hSliderLabelBlur = findobj(hFig, 'Style', 'text', 'Position', [660, 110, 50,
20]);

    createSlider(0, 200, areaOpen, [150, 140, 500, 20], @updateAreaOpen, 'Area
Open');

    hSliderAreaOpen = findobj(hFig, 'Style', 'slider', 'Position', [150, 140, 500,
20]);

    hSliderLabelAreaOpen = findobj(hFig, 'Style', 'text', 'Position', [660, 140, 50,
20]);

    createSlider(1, 10, structElemSize, [150, 170, 500, 20], @updateStructElem,
'Struct Elem');

    hSliderStructElem = findobj(hFig, 'Style', 'slider', 'Position', [150, 170, 500,
20]);

    hSliderLabelStructElem = findobj(hFig, 'Style', 'text', 'Position', [660, 170,
50, 20]);

    createSlider(1, 100, numColumns, [150, 200, 500, 20], @updateNumColumns, 'Number
of Columns');

    hSliderNumColumns = findobj(hFig, 'Style', 'slider', 'Position', [150, 200, 500,
20]);

    hSliderLabelNumColumns = findobj(hFig, 'Style', 'text', 'Position', [660, 200,
50, 20]);

    createSlider(0.1, 10, normalizationFactor, [150, 230, 500, 20],
@updateNormalization, 'Normalization');

    hSliderNormalization = findobj(hFig, 'Style', 'slider', 'Position', [150, 230,
500, 20]);

    hSliderLabelNormalization = findobj(hFig, 'Style', 'text', 'Position', [660, 230,
50, 20]);

    createSlider(0, 2, brightnessFactor, [150, 260, 500, 20], @updateBrightness,
'Brightness');
```

```
    hSliderBrightness = findobj(hFig, 'Style', 'slider', 'Position', [150, 260, 500,
20]);

    hSliderLabelBrightness = findobj(hFig, 'Style', 'text', 'Position', [660, 260,
50, 20]);

    createSlider(0.1, 2, contrastFactor, [150, 290, 500, 20], @updateContrast,
'Contrast');

    hSliderContrast = findobj(hFig, 'Style', 'slider', 'Position', [150, 290, 500,
20]);

    hSliderLabelContrast = findobj(hFig, 'Style', 'text', 'Position', [660, 290, 50,
20]);



    % Create checkboxes for optional steps

    hCheckboxGrayscale = uicontrol('Style', 'checkbox', 'String', 'Convert to
Grayscale', 'Position', [700, 80, 150, 20], 'Value', 1);

    hCheckboxBlur = uicontrol('Style', 'checkbox', 'String', 'Apply Gaussian Blur',
'Position', [700, 110, 150, 20], 'Value', 1);

    hCheckboxBackground = uicontrol('Style', 'checkbox', 'String', 'Subtract
Background', 'Position', [700, 140, 150, 20], 'Value', 1);



    % Create buttons for each step

    uicontrol('Style', 'pushbutton', 'String', 'Select First Frame', 'Position', [50,
20, 150, 30], 'Callback', @selectFirstFrame);

    uicontrol('Style', 'pushbutton', 'String', 'Convert to Grayscale', 'Position',
[210, 20, 150, 30], 'Callback', @convertToGrayscale);

    uicontrol('Style', 'pushbutton', 'String', 'Apply Gaussian Blur', 'Position',
[370, 20, 150, 30], 'Callback', @applyGaussianBlur);

    uicontrol('Style', 'pushbutton', 'String', 'Subtract Background', 'Position',
[530, 20, 150, 30], 'Callback', @subtractBackground);

    uicontrol('Style', 'pushbutton', 'String', 'Apply Threshold', 'Position', [690,
20, 150, 30], 'Callback', @applyThreshold);

    uicontrol('Style', 'pushbutton', 'String', 'Detect Particles', 'Position', [850,
20, 150, 30], 'Callback', @detectParticles);

    uicontrol('Style', 'pushbutton', 'String', 'Next Frame', 'Position', [1010, 20,
150, 30], 'Callback', @nextFrame);

    uicontrol('Style', 'pushbutton', 'String', 'Process Entire Video', 'Position',
[1010, 60, 150, 30], 'Callback', @processEntireVideo);
```

```
    % Create additional buttons for selecting a new video, resetting the preview,
saving results, and selecting range and sum

    uicontrol('Style', 'pushbutton', 'String', 'Select New Video', 'Position', [1010,
100, 150, 30], 'Callback', @selectNewVideo);

    uicontrol('Style', 'pushbutton', 'String', 'Save Results', 'Position', [1010,
140, 150, 30], 'Callback', @saveResults);

    uicontrol('Style', 'pushbutton', 'String', 'Reset Preview', 'Position', [1010,
180, 150, 30], 'Callback', @resetPreview);

    uicontrol('Style', 'pushbutton', 'String', 'Select Range and Sum', 'Position',
[1010, 220, 150, 30], 'Callback', @selectRangeAndSum);



    % Callback functions

    function createSlider(minVal, maxVal, initialValue, position, callback, label)

        uicontrol('Style', 'slider', 'Min', minVal, 'Max', maxVal, 'Value',
initialValue, 'Position', position, 'Callback', callback);

        uicontrol('Style', 'text', 'Position', [position(1) - 50, position(2), 50,
20], 'String', label);

        uicontrol('Style', 'text', 'Position', [position(1) + 510, position(2), 50,
20], 'String', num2str(initialValue));

    end



    function updateThreshold(~, ~)

        threshold = round(hSliderThreshold.Value);

        hSliderLabelThreshold.String = num2str(threshold);

    end



    function updateBlur(~, ~)

        blurAmount = hSliderBlur.Value;

        hSliderLabelBlur.String = num2str(blurAmount, '%.1f');

    end
```

```
function updateAreaOpen(~, ~)
    areaOpen = round(hSliderAreaOpen.Value);
    hSliderLabelAreaOpen.String = num2str(areaOpen);
end

function updateStructElem(~, ~)
    structElemSize = round(hSliderStructElem.Value);
    hSliderLabelStructElem.String = num2str(structElemSize);
end

function updateNumColumns(~, ~)
    numColumns = round(hSliderNumColumns.Value);
    hSliderLabelNumColumns.String = num2str(numColumns);
    plotParticleDistribution([]);
end

function updateNormalization(~, ~)
    normalizationFactor = hSliderNormalization.Value;
    hSliderLabelNormalization.String = num2str(normalizationFactor, '%.1f');
    adjustFinalImage();
end

function updateBrightness(~, ~)
    brightnessFactor = hSliderBrightness.Value;
    hSliderLabelBrightness.String = num2str(brightnessFactor, '%.1f');
    adjustFinalImage();
end
```

```
function updateContrast(~, ~)
    contrastFactor = hSliderContrast.Value;
    hSliderLabelContrast.String = num2str(contrastFactor, '%.1f');
    adjustFinalImage();
end

function selectFirstFrame(~, ~)
    frameNumber = 1;
    videoReader.CurrentTime = (frameNumber - 1) / videoReader.FrameRate;
    selectedFrame = readFrame(videoReader);
    imshow(selectedFrame, 'Parent', hAxesOriginal);
    title(hAxesOriginal, 'Original Frame');
    imshow(selectedFrame, 'Parent', hAxesProcessed);
    title(hAxesProcessed, 'Original Frame');
end

function convertToGrayscale(~, ~)
    if isempty(selectedFrame)
        errordlg('Please select the first frame first', 'Error');
        return;
    end
    frameGray = rgb2gray(selectedFrame);
    imshow(frameGray, 'Parent', hAxesProcessed);
    title(hAxesProcessed, 'Grayscale Image');
end
```

```
function applyGaussianBlur(~, ~)
    if isempty(frameGray)
        errordlg('Please convert to grayscale first', 'Error');
        return;
    end
    frameBlurred = imgaussfilt(frameGray, blurAmount);
    imshow(frameBlurred, 'Parent', hAxesProcessed);
    title(hAxesProcessed, 'Blurred Image');
end

function subtractBackground(~, ~)
    if isempty(frameBlurred)
        errordlg('Please apply Gaussian blur first', 'Error');
        return;
    end
    frameSubtracted = imsubtract(frameBlurred, backgroundGray);
    imshow(frameSubtracted, 'Parent', hAxesProcessed);
    title(hAxesProcessed, 'Background Subtracted');
end

function applyThreshold(~, ~)
    if isempty(frameSubtracted)
        errordlg('Please subtract the background first', 'Error');
        return;
    end
    binaryFrame = frameSubtracted > threshold;
    imshow(binaryFrame, 'Parent', hAxesProcessed);
    title(hAxesProcessed, 'Binary Image');
```

```
    end

    function detectParticles(~, ~)
        if isempty(binaryFrame)
            errordlg('Please apply threshold first', 'Error');
            return;
        end

        % Apply morphological operations to clean up the binary image
        binaryFrame = bwareaopen(binaryFrame, areaOpen); % Remove small objects
        se = strel('disk', structElemSize); % Structuring element for dilation
        binaryFrame = imdilate(binaryFrame, se); % Dilate to fill gaps

        % Detect particles
        cc = bwconncomp(binaryFrame);
        particleCentroids = regionprops(cc, 'Centroid', 'Area', 'MajorAxisLength',
'MinorAxisLength');

        % Filter out non-particle objects based on size and shape
        centroids = cat(1, particleCentroids.Centroid);
        areas = [particleCentroids.Area]';
        majorAxis = [particleCentroids.MajorAxisLength]';
        minorAxis = [particleCentroids.MinorAxisLength]';
        aspectRatio = majorAxis ./ minorAxis;
        validIdx = areas > 20 & aspectRatio < 5; % Filter by area and aspect ratio
        centroids = centroids(validIdx, :);

        % Plot particles if centroids are not empty and have the right dimensions
```

```
        if ~isempty(centroids) && size(centroids, 2) == 2
            imshow(binaryFrame, 'Parent', hAxesProcessed);
            hold(hAxesProcessed, 'on');
            plot(hAxesProcessed, centroids(:, 1), centroids(:, 2), 'r+');

            % Draw column separation lines
            xLimits = get(hAxesProcessed, 'XLim');
            yLimits = get(hAxesProcessed, 'YLim');
            columnSpacing = size(binaryFrame, 2) / numColumns;
            for col = 1:columnSpacing:size(binaryFrame, 2)
                line([col, col], yLimits, 'Color', 'b', 'Parent', hAxesProcessed);
            end
            hold(hAxesProcessed, 'off');
        else
            imshow(binaryFrame, 'Parent', hAxesProcessed);
        end

        % Count particles in each column based on the slider value
        particleCounts = zeros(1, numColumns);
        for i = 1:numColumns
            colStart = (i - 1) * columnSpacing + 1;
            colEnd = min(i * columnSpacing, size(binaryFrame, 2));
            if ~isempty(centroids) && size(centroids, 2) >= 1
                particleCounts(i) = sum(centroids(:, 1) >= colStart & centroids(:, 1)
<= colEnd);
            else
                particleCounts(i) = 0;
            end
```

```
    end

    % Update the particle data
    particleData = [particleData; frameNumber, size(centroids, 1)];

    % Plot particle distribution
    plotParticleDistribution(particleCounts);
    title(hAxesProcessed, 'Detected Particles');
end

function plotParticleDistribution(particleCounts)
    if ~isempty(particleCounts)
        bar(hAxesPlot, 1:length(particleCounts), particleCounts);
        xlabel(hAxesPlot, 'Column Number');
        ylabel(hAxesPlot, 'Particle Count');
        title(hAxesPlot, 'Particle Distribution Across Columns');
    else
        cla(hAxesPlot);
        title(hAxesPlot, 'Particle Distribution Across Columns');
    end
    drawnow;
end

function nextFrame(~, ~)
    if isempty(videoReader)
        errordlg('Please select a video first', 'Error');
        return;
```

```
        end
        if frameNumber < videoReader.NumFrames
            frameNumber = frameNumber + 1;
            videoReader.CurrentTime = (frameNumber - 1) / videoReader.FrameRate;
            selectedFrame = readFrame(videoReader);
            imshow(selectedFrame, 'Parent', hAxesOriginal);
            title(hAxesOriginal, 'Original Frame');
            processFrameSteps();
        else
            msgbox('End of video reached', 'Info');
            writetable(array2table(particleData, 'VariableNames', {'Frame',
'ParticleCount'}), 'particle_counts.csv');
        end
    end

    function processEntireVideo(~, ~)
        if isempty(videoReader)
            errordlg('Please select a video first', 'Error');
            return;
        end

        % Initialize variables for tracking
        numFrames = floor(videoReader.Duration * videoReader.FrameRate);
        allParticleCounts = zeros(numFrames, numColumns);
        columnSpacing = size(binaryFrame, 2) / numColumns;

        % Initialize the intensity frame
        intensityFrame = zeros(videoReader.Height, videoReader.Width);
```

```
        previousCentroids = [];
        particlePaths = {};
        kalmanFilters = {};

        % Process each frame
        frameCount = 1;
        while hasFrame(videoReader)
            try
                frame = readFrame(videoReader);
                fprintf('Processing frame %d\n', frameCount); % Debugging output
                [particleCount, centroids, binaryFrame] = processFrame(frame,
backgroundFrame);

                % Count particles in each column based on the slider value
                particleCounts = zeros(1, numColumns);
                for i = 1:numColumns
                    colStart = (i - 1) * columnSpacing + 1;
                    colEnd = min(i * columnSpacing, size(binaryFrame, 2));
                    if ~isempty(centroids) && size(centroids, 2) >= 1
                        particleCounts(i) = sum(centroids(:, 1) >= colStart &
centroids(:, 1) <= colEnd);
                    else
                        particleCounts(i) = 0;
                    end
                end
                allParticleCounts(frameCount, 1:numColumns) = particleCounts;

                % Update the intensity frame
                intensityFrame = intensityFrame + double(binaryFrame);
```

```
                % Initialize Kalman filters for new particles
                for i = 1:size(centroids, 1)
                    if isempty(previousCentroids) || i > numel(kalmanFilters)
                        kalmanFilters{end+1} =
configureKalmanFilter('ConstantVelocity', centroids(i, :), [1 1]*1e5, [25, 10], 25);
                    end
                end

                % Track particles using Kalman filter
                if isempty(previousCentroids)
                    for i = 1:size(centroids, 1)
                        particlePaths{end+1} = centroids(i, :); %#ok<AGROW>
                    end
                else
                    for i = 1:numel(kalmanFilters)
                        predictedCentroid = predict(kalmanFilters{i});
                        distances = pdist2(predictedCentroid, centroids);
                        [minDist, minIndex] = min(distances, [], 2);
                        if minDist < 20 % Adjust this threshold as needed
                            correct(kalmanFilters{i}, centroids(minIndex, :));
                            if i <= length(particlePaths)
                                particlePaths{i}(end+1, :) = centroids(minIndex, :);
                            else
                                particlePaths{i} = centroids(minIndex, :);
                            end
                        else
                            % Mark as lost
```

```
                kalmanFilters{i} = [];
            end
        end
        % Remove empty Kalman filters
        kalmanFilters = kalmanFilters(~cellfun('isempty',
kalmanFilters));
    end
    previousCentroids = centroids;

    % Display the original and processed frames
    imshow(frame, 'Parent', hAxesOriginal);
    title(hAxesOriginal, sprintf('Frame %d', frameCount));
    if ~isempty(centroids) && size(centroids, 2) == 2
        imshow(binaryFrame, 'Parent', hAxesProcessed);
        hold(hAxesProcessed, 'on');
        plot(hAxesProcessed, centroids(:, 1), centroids(:, 2), 'r+');

        % Draw column separation lines
        xLimits = get(hAxesProcessed, 'XLim');
        yLimits = get(hAxesProcessed, 'YLim');
        for col = 1:columnSpacing:size(binaryFrame, 2)
            line([col, col], yLimits, 'Color', 'b', 'Parent',
hAxesProcessed);
        end
        hold(hAxesProcessed, 'off');
    else
        imshow(binaryFrame, 'Parent', hAxesProcessed);
    end
```

```
                title(hAxesProcessed, 'Detected Particles');
                plotParticleDistribution(particleCounts);
                drawnow;
                frameCount = frameCount + 1;
            catch ME
                warning('Error processing frame %d: %s', frameCount, ME.message);
                frameCount = frameCount + 1; % Ensure we continue processing the next
frame
                continue;
            end
        end

        % Sum the particle counts for each column across all frames
        totalParticleCounts = sum(allParticleCounts, 1);

        % Normalize the intensity frame
        finalCumulativeImage = intensityFrame;
        adjustFinalImage();

        % Normalize total particle counts per column
        normalizedTotalParticleCounts = totalParticleCounts /
max(totalParticleCounts);

        msgbox('Processing complete. You can now save the results.', 'Info');
    end

    function selectNewVideo(~, ~)
        [fileName, filePath] = uigetfile({'*.avi;*.mp4', 'Video Files (*.avi,
*.mp4)'}, 'Select a Video File');
```

```
if isequal(fileName, 0)
    disp('User selected Cancel');
    return;
end
videoFile = fullfile(filePath, fileName);

% Load the new video
videoReader = VideoReader(videoFile);
backgroundFrame = readFrame(videoReader);
backgroundGray = rgb2gray(backgroundFrame);

% Reset variables and UI
selectedFrame = [];
frameGray = [];
frameBlurred = [];
frameSubtracted = [];
binaryFrame = [];
threshold = 50;
blurAmount = 2;
areaOpen = 30;
structElemSize = 2;
frameNumber = 1;
particleData = [];
previousCentroids = [];
particlePaths = {};
kalmanFilters = {};
imshow(backgroundFrame, 'Parent', hAxesOriginal);
title(hAxesOriginal, 'Background Frame');
```

```
        imshow([], 'Parent', hAxesProcessed);
        title(hAxesProcessed, 'Processed Frame');
    end

    function resetPreview(~, ~)
        imshow([], 'Parent', hAxesProcessed);
        title(hAxesProcessed, 'Processed Frame');
        particlePaths = [];
        previousCentroids = [];
        kalmanFilters = [];
    end

    % Function to process a frame
    function [particleCount, centroids, binaryFrame] = processFrame(frame,
backgroundFrame)
        % Convert to grayscale if needed
        if get(hCheckboxGrayscale, 'Value')
            frameGray = rgb2gray(frame);
        else
            frameGray = frame;
        end

        % Apply Gaussian blur if needed
        if get(hCheckboxBlur, 'Value')
            frameBlurred = imgaussfilt(frameGray, blurAmount);
        else
            frameBlurred = frameGray;
        end
```

```
        % Subtract background if needed
        if get(hCheckboxBackground, 'Value')
            frameSubtracted = imsubtract(frameBlurred, backgroundGray);
        else
            frameSubtracted = frameBlurred;
        end

        % Apply threshold to create a binary image
        binaryFrame = frameSubtracted > threshold;

        % Apply morphological operations to clean up the binary image
        binaryFrame = bwareaopen(binaryFrame, areaOpen); % Remove small objects
        se = strel('disk', structElemSize); % Structuring element for dilation
        binaryFrame = imdilate(binaryFrame, se); % Dilate to fill gaps

        % Detect particles
        cc = bwconncomp(binaryFrame);
        particleCentroids = regionprops(cc, 'Centroid', 'Area', 'MajorAxisLength',
'MinorAxisLength');

        % Filter out non-particle objects based on size and shape
        centroids = cat(1, particleCentroids.Centroid);
        areas = [particleCentroids.Area]';
        majorAxis = [particleCentroids.MajorAxisLength]';
        minorAxis = [particleCentroids.MinorAxisLength]';
        aspectRatio = majorAxis ./ minorAxis;
        validIdx = areas > 20 & aspectRatio < 5; % Filter by area and aspect ratio
```

```
        centroids = centroids(validIdx, :);

        % Count particles
        particleCount = size(centroids, 1);
    end

    % Function to process frame steps
    function processFrameSteps()
        convertToGrayscale();
        applyGaussianBlur();
        subtractBackground();
        applyThreshold();
        detectParticles();
        adjustFinalImage();
    end

    % Function to adjust brightness, contrast, and normalization of the final
cumulative image
    function adjustFinalImage()
        if ~isempty(finalCumulativeImage)
            % Normalize the intensity frame
            normalizedIntensityFrame = mat2gray(finalCumulativeImage) *
normalizationFactor;

            % Adjust brightness
            adjustedImage = normalizedIntensityFrame * brightnessFactor;

            % Adjust contrast
```

```
            adjustedImage = imadjust(adjustedImage, [], [], contrastFactor);


            % Ensure values are within valid range
            adjustedImage(adjustedImage > 1) = 1;
            adjustedImage(adjustedImage < 0) = 0;


            % Display the adjusted image
            imshow(adjustedImage, 'Parent', hAxesProcessed);
            title(hAxesProcessed, 'Adjusted Brightness, Contrast, and
Normalization');
        end
    end


    % Function to save the results
    function saveResults(~, ~)
        % Save the graph of the total particle count per column
        figure;
        plot(1:length(totalParticleCounts), totalParticleCounts, '-.'); % Line graph
with markers
        xlabel('Column Number');
        ylabel('Total Particle Count');
        title('Total Particle Count per Column');
        grid on;
        saveas(gcf, 'total_particle_count_per_column.png');


        % Save the graph of the normalized total particle count per column
        figure;
        plot(1:length(normalizedTotalParticleCounts), normalizedTotalParticleCounts,
'-.'); % Line graph with markers
```

```
        xlabel('Column Number');
        ylabel('Normalized Particle Count');
        title('Normalized Particle Count per Column');
        grid on;
        saveas(gcf, 'normalized_particle_count_per_column.png');

        % Capture and save the adjusted final image as displayed
        frame = getframe(hAxesProcessed);
        imwrite(frame.cdata, 'final_cumulative_image.png');

        % Save particle counts to CSV
        particleCountTable = array2table(allParticleCounts, 'VariableNames',
arrayfun(@(x) sprintf('Col_%d', x), 1:size(allParticleCounts, 2), 'UniformOutput',
false));
        writetable(particleCountTable, 'particle_counts_per_column.csv');

        msgbox('Results saved successfully.', 'Info');
    end

    % Function to select range and sum particles
    function selectRangeAndSum(~, ~)
        % Replace particle distribution plot with total particle count plot
        plotTotalParticleCount();

        % Create range selection sliders
        uicontrol('Style', 'slider', 'Min', 1, 'Max', numColumns, 'Value',
selectedRange(1), 'Position', [1200, 780, 150, 20], 'Callback', @updateRangeStart);
        uicontrol('Style', 'slider', 'Min', 1, 'Max', numColumns, 'Value',
selectedRange(2), 'Position', [1400, 780, 150, 20], 'Callback', @updateRangeEnd);
```

```
        uicontrol('Style', 'text', 'Position', [1200, 800, 150, 20], 'String', 'Start
Column');

        uicontrol('Style', 'text', 'Position', [1400, 800, 150, 20], 'String', 'End
Column');



        updateRangeDisplay();

    end



    function updateRangeStart(src, ~)

        selectedRange(1) = round(src.Value);

        updateRangeDisplay();

    end



    function updateRangeEnd(src, ~)

        selectedRange(2) = round(src.Value);

        updateRangeDisplay();

    end



    function updateRangeDisplay()

    cla(hAxesPlot);

    plot(hAxesPlot, 1:length(totalParticleCounts), totalParticleCounts, '-');

    xlabel(hAxesPlot, 'Column Number');

    ylabel(hAxesPlot, 'Total Particle Count');

    title(hAxesPlot, 'Total Particle Count per Column');

    hold on;

    area(hAxesPlot, selectedRange(1):selectedRange(2),
totalParticleCounts(selectedRange(1):selectedRange(2)), 'FaceColor', 'r',
'FaceAlpha', 0.5);

    hold off;
```

```
    rangeSum = sum(totalParticleCounts(selectedRange(1):selectedRange(2)));

    uicontrol('Style', 'text', 'Position', [1300, 850, 150, 20], 'String',
sprintf('Sum: %d', rangeSum));



    drawnow;

end


function plotTotalParticleCount()

    cla(hAxesPlot);

    plot(hAxesPlot, 1:length(totalParticleCounts), totalParticleCounts, '-');

    xlabel(hAxesPlot, 'Column Number');

    ylabel(hAxesPlot, 'Total Particle Count');

    title(hAxesPlot, 'Total Particle Count per Column');

    drawnow;

end



    % Display the first frame initially

    imshow(backgroundFrame, 'Parent', hAxesOriginal);

    title(hAxesOriginal, 'Background Frame');


end
```